

Generation of Long-time Complex Signals for Testing the Instruments for Detection of Voltage Quality Disturbances

Dragan Živanović¹, Milan Simić¹, Zivko Kokolanski², Dragan Denić¹, Vladimir Dimcev²

¹University of Niš, Faculty of Electronic Engineering, A. Medvedeva 14, 18000 Niš, Serbia, dragan.zivanovic@elfak.ni.ac.rs

²Ss. Cyril and Methodius University, Faculty of Electrical Engineering and Information Technologies, R. Boshkovik bb, 1000 Skopje, Macedonia

Software supported procedure for generation of long-time complex test sentences, suitable for testing the instruments for detection of standard voltage quality (VQ) disturbances is presented in this paper. This solution for test signal generation includes significant improvements of computer-based signal generator presented and described in the previously published paper [1]. The generator is based on virtual instrumentation software for defining the basic signal parameters, data acquisition card NI 6343, and power amplifier for amplification of output voltage level to the nominal RMS voltage value of 230 V. Definition of basic signal parameters in LabVIEW application software is supported using Script files, which allows simple repetition of specific test signals and combination of more different test sequences in the complex composite test waveform. The basic advantage of this generator compared to the similar solutions for signal generation is the possibility for long-time test sequence generation according to predefined complex test scenarios, including various combinations of VQ disturbances defined in accordance with the European standard EN50160. Experimental verification of the presented signal generator capability is performed by testing the commercial power quality analyzer Fluke 435 Series II. In this paper are shown some characteristic complex test signals with various disturbances and logged data obtained from the tested power quality analyzer.

Keywords: Signal generation, instrument testing, voltage quality disturbances, LabVIEW software.

1. INTRODUCTION

In recent years, electrical power quality has become a very important and significant topic, foremost due to limitations of natural resources necessary for electrical power production and widespread usage of renewable energy resources. Powerful electronic components and switching devices can directly cause quality level degradation, which affects the production process costs and reduces reliability of customer electrical devices and equipment. In order to provide the required level of energy efficiency in electrical power production, distribution and consumption, including providing final customer protection, the optimal voltage supply level is determined according to relevant international standards and regulations [2], [3]. For example, the European power quality standard EN50160 defines voltage characteristics of the public electrical power distribution systems under normal operating conditions. The required quality level is determined by reference nominal values and acceptable tolerances of basic quality parameters and typical network disturbances. Continuous measurements of voltage quality parameters at carefully selected locations inside the power distribution network, including software processing of the obtained measurement results, are necessary to provide the relevant information for proper

assessment of electrical power quality level. Instruments and equipment designed for measurement and software supported processing of standard quality parameters are available on the market in various constructive and functional solutions. Such measurement instruments are designed to perform continuous monitoring of voltage supply quality at selected locations inside electrical power distribution networks. Using continuous measurement of standard quality parameters, including software supported statistical and diagnostic activities in the single and three-phase power distribution systems, these instruments are capable to verify compliance of measured parameters with quality standards requirements. The European standard EN50160 defines reference values, acceptable limits, measurement intervals and monitoring periods for following quality parameters and network disturbances: frequency variations, slow RMS voltage value variations, voltage dips and voltage swells, temporary and transient overvoltages, short and long time voltage interruptions, three-phase signal unbalance and maximum levels of individual high-order signal harmonic components [4].

Having in mind the significant importance of VQ issues and problems, there have been developed various sophisticated and reliable microprocessor-based instruments and complex measurement systems for continuous electrical

power quality monitoring in recent years. Generally speaking, software based virtual instruments can be very useful and successful in realization of flexible computer-based measurement systems. A number of research and scientific papers related to the use of virtual instrumentation for electrical power quality measurement and reference signal generation have been published so far [5]-[10]. Naturally, in order to satisfy the required measurement accuracy level, instruments and equipment for measurement of quality parameters must be supported by appropriate metrological traceability. Reference instruments, voltage and current calibrators, are sources of reference waveforms with high accuracy parameters, which correspond to the secondary standards, laboratory and industrial standards. Also, there are some commercial calibration instruments developed for testing of specific types of quality meters and analyzers. Closed and not flexible functional architecture, predesigned according to some relevant quality standards, for example EN50160, presents certain limitation of these instruments. Virtual instrument, presented in the paper, is capable of reproducing long-time predefined complex test scenarios, including various combinations of standard VQ disturbances. This solution, easily adaptable to various practical requirements, random test sequence generation and upgrading, includes significant improvements of computer supported signal generator presented and described in the previously published paper [1]. It is suitable for testing the commercial instruments for detection of standard voltage quality disturbances. For the purpose of practical experimental verification, developed complex signal generator is applied for testing three-phase quality analyzer Fluke 435 Series II [11]. Complete test procedure, generated characteristic test waveforms and important results obtained from test procedure are presented and analyzed in the paper.

2. BASIC CONFIGURATION AND DESCRIPTION OF VIRTUAL VQ SIGNAL GENERATOR

Software supported generator of sinusoidal voltage waveforms with standard quality disturbances is based on the virtual instrument programmed in LabVIEW graphical environment, data acquisition card NI PCIe 6343 for output signal generation and external power amplifier.

Signal generation virtual instrument (VI) is divided into two basic functional segments: a graphical user interface (virtual instrument front panel) and executive program code (virtual instrument block diagram), interlinked between each other. At the left sides of the control front panel of LabVIEW virtual instrument (shown in Fig.1.), one can see default values of signal parameters per each of the three signal phases: nominal signal amplitude and frequency, phase angle, signal DC offset, noise level, flicker amplitude, flicker frequency, and overall control of presence of high-order harmonics. Percentage level of the specific high-order harmonics can be precisely determined by an array of the control knobs for harmonic regulation. Using these defined parameters, virtual instrument successively calculates samples for signal generation and sends specific samples to the buffer of data acquisition card for output signal generation. Sample rate, as well as duration of test sequence is also present at the front panel. Shown front panel

generates test voltage waveform with nominal frequency value of 50 Hz and normalized RMS voltage value of 5.6 V. This selected RMS voltage value corresponds to the nominal power line voltage level of 230 V, after amplification of generated waveform using the external power amplifier.

In addition to such generation of test signal, similar to the one shown in [1], presented generator includes an array of commands to change any of the enumerated parameters, in defined time, with defined rising time, and goal value of parameter. That array of changes, present at the right side of the front panel in Fig.1., enables a more complex predefined test scenario during the generation process. Each type of signal disturbances, for example voltage swell, voltage dip, interruption, flicker, noise and high-order signal harmonic components, can be combined in serial combination, and unified in the form of final complex sequence, according to the requirements of the European quality standard EN50160 [4]. As an example, graphical presentation of voltage test signal with various quality disturbances, generated using the described LabVIEW based virtual instrument, is given in Fig.2.

Another feature in the presented generator is the possibility to load default parameter values and the list of commands from a textual script file, before starting generation. Such approach with a script file definition of generator working enables easy repetition of several different test scenarios, automatic generation of test files and manual editing or combining test scenarios by using a standard text editor.

Example of the script file including changing of default parameter at the beginning, and then an array of commands to change particular parameters are presented in Fig.3. One command is based on one line of text. Comments can be anywhere after `'''` characters. Line which changes one of the default values contains three parameters separated with comma `,` character. Line starts with the name of the voltage phase, then comes the name of parameter, and goal values of that parameter are at the end.

Line with command for dynamic change of parameter in any moment during signal generation contains five parameters, separated with coma character. After the name of the phase, before the parameter name, comes the start time for this change, and the rising time while a particular parameter will linearly change value from previous value to goal value. Short increasing of signal amplitude (defined over parameter U_{eff} as $\sqrt{2} * U_{eff}$) can be set by two commands: first which will increase U_{eff} , and second which will change U_{eff} to previous value. It is also possible to put several short transients of voltage in any moment during generation of signal, by command for Transient parameter, where the third parameter "rising time" will present duration of transient.

In the example of script file, presented in Fig.3., one can see definition of start U_{eff} value of 5.6 V, definition of present flicker with amplitude 5 % of signal amplitude, frequency of flicker as 1 Hz, and amounts of noise in generated signal 1 % of amplitude. Based on such defined signal, level of noise will change after 2.2 s, short swell of voltage will be from 10.7 s to 12 s, and at the end of the file, one transient of voltage is defined to be in 15.2 s from beginning of the signal generation.

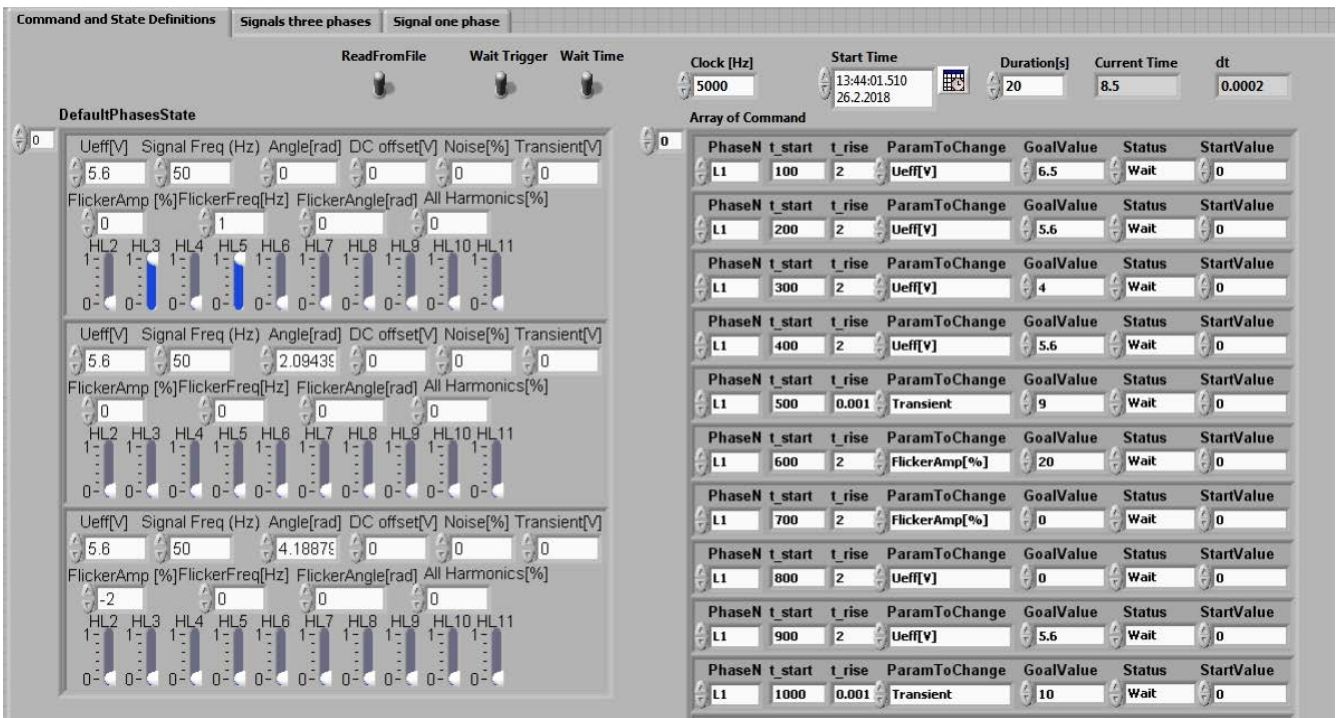


Fig.1. Control front panel of LabVIEW virtual instrument for generation of standard VQ signal disturbances.

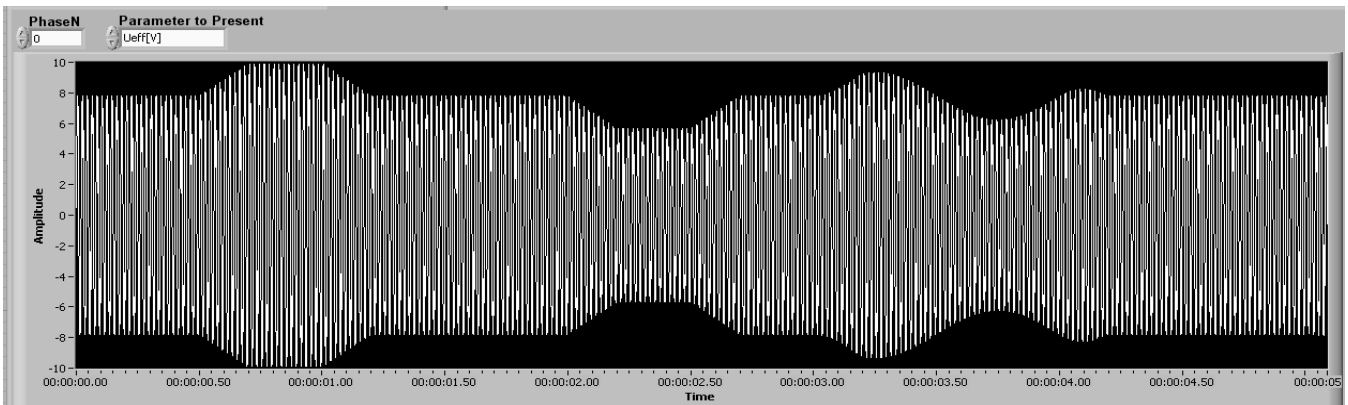


Fig.2. Graphical presentation of voltage test signal with various disturbances generated using LabVIEW based virtual instrument.

```

SagSweTest1.txt - Notepad
File Edit Format View Help
// Start values for first phase - can be defined for three phases together
// All parameter names should be without unit!

L1, Ueff, 5.6 // phase L1, Default voltage
L1, FlickerAmp, 5.0 // phase L1, Flicker 5% of amplitude
L1, FlickerFreq, 1.0 // Flicker frequency 1Hz
L1, Noise, 1.1 // in [%] of amplitude

// Definition of changes as:
// phase, start_time, rise_time, parameter, goal_value

L1, 2.2, 0, Noise, 3.5 // Phase L1, Change Noise level, after 2.2s immediately to 3.5% of voltage amplitude
L1, 10.7, 0.3, Ueff, 7 // Change Ueff, after 10.7s in 0.3s from current value to 7V
L1, 12, 1.1, Ueff, 5.6 // Return back Urms to 5.6v
L1, 15.2, 0.001, Transient, 9 // Transient in L1, duration of 1ms
    
```

Fig.3. Example of test voltage waveform with various signal disturbances defined in .txt script file.

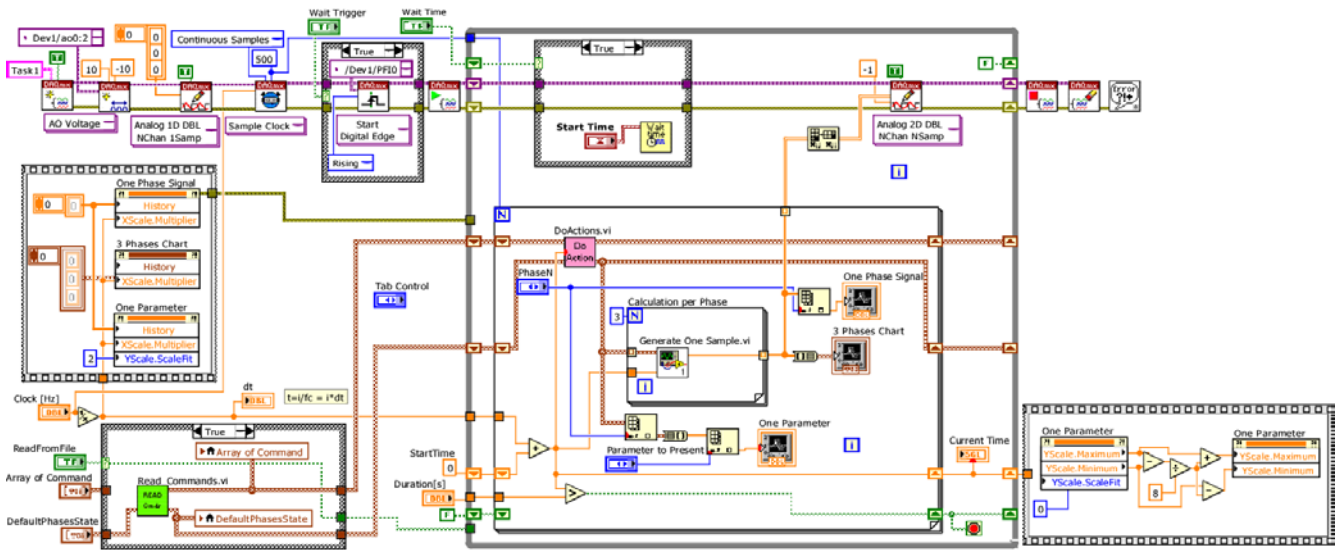


Fig.4. Block diagram (software code) of LabVIEW virtual instrument for generation of VQ signal disturbances.

Block diagram (executive software code) of LabVIEW based virtual instrument for signal generation is shown in Fig.4. In the sub VI called "Read_ Commands.vi", reading of Script file and changes of predefined default parameter values is performed. In the main software loop, during calculation of each individual signal sample, using sub VI "DoActions.vi", program checks through an array of commands if current time is larger than the defined start time. If it is true, this specific parameter needs to be changed linearly in the period of rise time. Then, using changed parameter values (amplitude, frequency, high-order harmonics, noise, etc.), individual signal samples are calculated in the sub VI "Generate_One_Sample.vi". In order to improve the overall virtual instrument performances, 500 samples at once per each phase are calculated and sent to data acquisition card NI PCIe 6343.

Reproduction of time axis during generation is based on a defined sample rate and counting of samples from the beginning of generation. Time reference for start of generation can be chosen at the front panel by two switches: waiting for exact start time (entered by user), and/or waiting for external trigger signal. If both switches are in off position, generation will start instantly when program is started. If exact time for starting generation is chosen, then accuracy of that time reference largely depends on the version of the computer operating system, and its automatic synchronization to the Universal Coordinated Time (UTC). External trigger input enables synchronization in the accuracy of one sample time. Not dependent on selected start of generation, accuracy of time interval between two disturbances will be caused only by accuracy of data acquisition card NI 6343 sample rate generator, specified as 50 ppm. This will produce maximal error of 18 ms after one hour of generation.

Using high performance universal counter HP5316B, time between the appearances of two transients is measured, and the result of 1.0000137 s is obtained. As this time is defined in script file to be one second, it can be calculated that

sample rate generator in the used acquisition card has an error of 13.7 ppm.

Generation process will be interrupted when total time of generated signal samples ($\text{Current_Time} = N \cdot 1/f$ sample) becomes equal to or greater than previously defined "Duration", at the front panel of virtual instrument.

Working with three phases together is possible in realized generator and script file, in order to simulate a three-phase power distribution system. However, in the experiments described in this paper, signal generator is used for generating L1 - one phase voltage waveforms.

Signal calculated using the LabVIEW software can be reproduced by standard data acquisition card with analog output channels. However, this acquisition card must have good-enough resolution (which is defined by the required output signal uncertainty) and must support high-enough sampling frequency. Theoretically, the sampling frequency has to be at least two times higher than the frequency of highest signal harmonic. According to the standard EN50160 (up to 50th harmonic), the minimum sampling frequency is 5 kHz. In practice, the sampling frequency should be higher in order to maintain the accuracy of the higher signal harmonics. For this application, real-time generation of previously defined test voltage waveforms with standard VQ disturbances is performed using analog outputs of the D/A data acquisition card NI PCIe 6343 [12]. This is a 32-channel PCIe acquisition card, with digital to analog signal conversion, output signal range of ± 10 V and 16-bit resolution. In order to provide the output signal level required for testing the instruments for VQ measurement, reference signals generated on the data acquisition board analog outputs must be amplified to the nominal power line voltage level of 230 V. For realization of signal amplifier several analog signal processing blocks were used: low pass antialiasing filter (to restrict the input signal bandwidth and eliminate noise), preamplifier (to amplify the input signal to the required given reference level), and power amplifier (to amplify the input signal to the nominal power line voltage

level of 230 V). Design and implementation of this specific power quality (PQ) amplifier used for signal amplification are already described in recently published scientific papers [1], [13].

For low-pass antialiasing filter a fourth order Butterworth low-pass filter in Sallen-key configuration realized as the cascade of two two-pole filters was designed. Considering that 50th voltage harmonic ($f_{50} = 2.5$ kHz) has to be generated, the cut-off filter frequency is 5.45 kHz. Preamplifier has a double function: to amplify the input signal from acquisition card to the standardized reference level and to limit the input voltage level. Power amplifier is designed to amplify input signal to the power line voltage levels. However, in order to be able to generate voltage swells, the power line voltage level should be placed near the middle of the data acquisition card analog output range. The power amplifier was designed by using high voltage operation amplifier APEX PA97 [14]. The amplifier is capable of delivering 10 mA at 500 V (or power of 5 W), which is sufficient to test the commercial quality meters. The amplifier was designed in an inverting configuration with amplification of 40 times. Special attention has to be paid to the power amplifier supply. In this realization, a classical Zener-diode based power supply of ± 430 V was designed.

Table 1. Summary of measurement uncertainty components for signal generator voltage uncertainty budget at 50 Hz.

Voltage uncertainty source	Uncertainty value [V]
Standard deviation of measurement results from amplifier	0.0020162
Calibrator uncertainty	0.0267748
Calibrator resolution	0.0000058
Multimeter uncertainty in amplifier range	0.1407124
Multimeter resolution in amplifier range	0.0002887
Combined uncertainty amplifier - u_{CAMP}	0.1432500
Expanded uncertainty amplifier - u_{EAMP}	0.2807700
Standard deviation of measurement results from data acquisition card - DAQ	0.0000235
Multimeter uncertainty in DAQ range	0.0023240
Multimeter resolution in DAQ range	0.0000029
DAQ card uncertainty	0.0000013
DAQ card resolution	0.0000881
Combined uncertainty for DAQ - u_{CDAQ}	0.0023300
Expanded uncertainty for DAQ - u_{EDAQ}	0.0045600
Combined uncertainty - signal generator	0.1432690
Expanded voltage uncertainty of signal generator - u_{EGEN}	0.28 V

Metrological performances of applied signal generator are evaluated using the professional instrumentation. Reference input signal was obtained from high quality signal source - calibrator Fluke 5500A and output signal parameters are measured with 6½ digit precision digital multimeter Fluke 8846A, which is described in [1]. For complete assessment extensive measurement uncertainty calculation is performed,

according to the recommendations of the document “Guide to the Expression of Uncertainty in Measurement”, as defined by the International Organization for Standardization - ISO. Final summary of measurement uncertainty components for signal generator voltage uncertainty budget is shown in Table 1.

This procedure includes calculation of standard, combined and expanded measurement uncertainties and presentation of overall uncertainty budget. Uncertainty calculation is based on three main segments: calculation of amplifier uncertainty, data acquisition card - DAQ uncertainty, and calculation of entire signal generator uncertainty.

Calculation of standard uncertainty involves Type A uncertainty (standard deviation of the measurement results) and Type B uncertainty (calibrator uncertainty, calibrator resolution, multimeter uncertainty, multimeter resolution, DAQ uncertainty, and DAQ resolution). Calculation of the combined voltage uncertainties for amplifier and DAQ card is based on the previously calculated Type A and Type B uncertainties. Considering the values of amplifier combined uncertainty (u_{CAMP}) and DAQ combined uncertainty (u_{CDAQ}), combined voltage uncertainty of signal generator is:

$$u_{CGEN}(V) = \sqrt{u_{CAMP}^2 + u_{CDAQ}^2} \quad (1)$$

Finally, expanded measurement uncertainty is calculated for desired confidence probability level of 95 % (value of coverage factor k is 1.96). Using the previously calculated value of combined voltage uncertainty, expanded voltage uncertainty of computer-based signal generator is:

$$u_{EGEN}(V) = 1.96u_{CGEN} = 1.96\sqrt{u_{CAMP}^2 + u_{CDAQ}^2} \quad (2)$$

Experimental results show that signal generator expanded voltage uncertainty of ± 0.28 V and frequency uncertainty of ± 8 MHz can be achieved [1].

3. EXPERIMENTAL PROCEDURE FOR TESTING INSTRUMENTS FOR DETECTION OF VQ DISTURBANCES

Capability of developed signal generator to generate proper signal for testing commercial quality analyzers is experimentally verified in this chapter by testing quality analyzer Fluke 435 Series II. Block configuration of experimental system is presented in Fig.5. Amplified voltage waveforms, generated by VQ signal generator with various standard disturbances, are sent directly to the voltage inputs of device under test (DUT) - measurement instrument Fluke 435.

The photo of experimental system including computer-based signal generator, acquisition card connector block SCB 68 A, PQ signal amplifier and tested instrument Fluke 435 is shown in Fig.6.

Setup of experimental test procedure includes various tests with generation of reference voltage waveforms with some characteristic variations of standard VQ disturbances. Computer supported testing of instrument Fluke 435 is focused on detection of standard VQ disturbances: voltage

swells, voltage dips, transients and voltage interruptions, in accordance with the recommendations of the European standard EN50160. Test scenarios also include certain presence of high-order harmonics, flicker, and noise in defined intervals.

Communication principle between instrument Fluke 435 and computer supported by Power Log application software for processing of previously recorded data is shown in Fig.7.

Instrument Fluke 435 is set to operate in the Data logging mode. Time interval for each measurement cycle in instrument data logger is adjusted to 0.25 s. Duration of data logging is equal to length of reference test signals from generator. Logged signals and data recorded in instrument database are transferred to computer according to the USB communication principle previously presented in Fig.7. Power Log software provides various possibilities for processing and analysis of recorded data and logged signals. In this paper there will be presented the following results of data analysis: time diagrams and histograms of RMS voltage values measured using instrument Fluke 435, diagrams of

detected and measured high-order harmonics of reference test signals, diagrams of disturbance events detected using Fluke 435 (swells, dips, rapid voltage changes, transients, interruptions, etc.), including some reports about detected disturbances recorded directly from graphical display of tested instrument. Time diagram of measured RMS voltage values for 1800 s (30 minutes) long voltage test signal, including a large number of various disturbances, recorded using the Power Log application software, is presented in Fig.8. In this diagram are chronologically and clearly indicated detected events (voltage disturbances) with specific measured RMS voltage values related to individual events. Script files with such large number of signal disturbances are produced with the help of additional LabVIEW application software for random generation of various signal disturbances. As the produced script file is written to .txt text file, it is possible to inspect it, and also manually modify with any text editor before using it, and store in database of test scenarios, for repetition of test, or later possible applications.

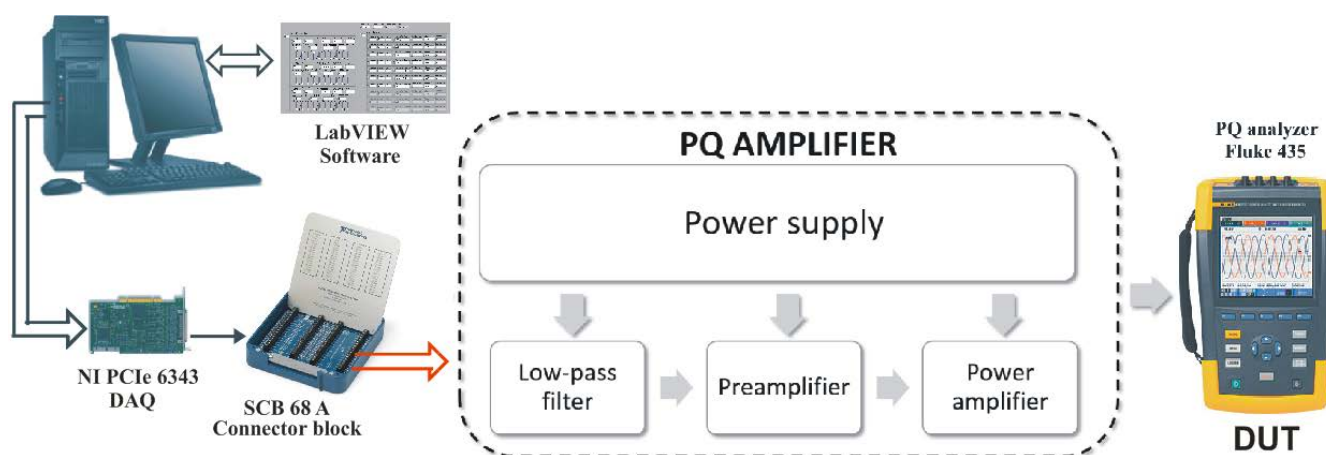


Fig.5. Block diagram of experimental procedure for testing quality analyzer Fluke 435 using LabVIEW based signal generator.

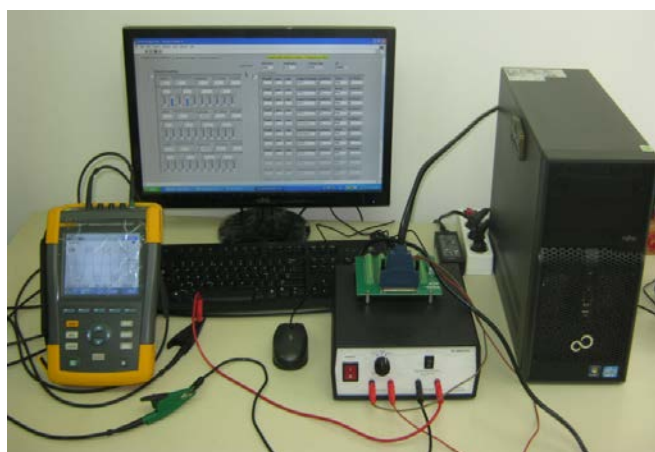


Fig.6. Photo of experimental system for testing instrument Fluke 435 using LabVIEW based signal generator.

Analyzer Fluke 435 detects voltage disturbances according to the standard EN50160. This standard prescribes acceptable limits of nominal RMS voltage value $230\text{ V} \pm 10\%$ (207 V to 253 V). Practically, the RMS voltage values larger than 253 V are detected by the instrument as the swell (SWL), while the RMS voltage values smaller than 207 V are detected by the instrument as the dip (DIP). On the other hand, instrument detects voltage interruption (INT) in the cases when measured voltage values are smaller than 1 % of nominal RMS voltage value (1 % of 230 V). This practically means that interruptions will be detected for voltage values smaller than 2.3 V. For voltage levels smaller than 10 % of nominal RMS voltage value (10 % of 230 V) the instrument indicates the rapid voltage change (CHG). Finally, for short-time and very fast rapid voltage rise, in amount greater than 100 V in relation to nominal RMS voltage value, instrument will detect the voltage transient (TRA).



Fig.7. USB communication between instrument Fluke 435 and computer for recording and processing of measurement data.

As an example, for instrument events detection, in Fig.9. is presented a detailed summary of chronologically detected voltage disturbances in test signal, recorded directly from graphical display of tested analyzer. This summary gives just a small part of all detected signal disturbances, due to the space limitations in instrument display. In this report summary are included the following data: types of detected voltage events, exact dates and times for individual detections, voltage amount and time duration for detected individual disturbances and events.

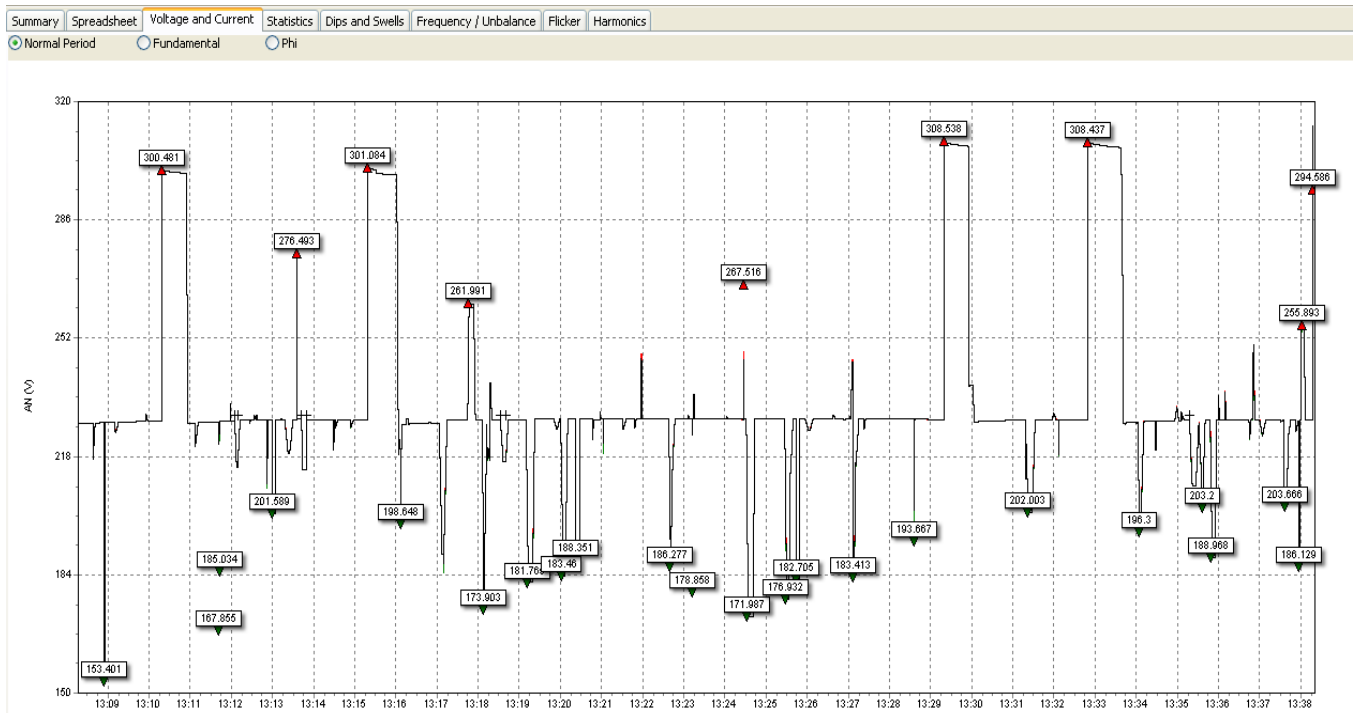


Fig.8. Time diagram of measured RMS voltage values - 30 minutes long test signal with large number of voltage disturbances.

More detailed analysis of detected disturbances is provided using the Power Log application software. Software analysis of detected signal disturbances for previous case according to the standard EN50160 is presented in diagrams in Fig.10. Two curves in this figure, blue and red, indicate general standard power acceptability limits. Blue curve is CBEMA Curve - Power Acceptability Curve for Computer Business Equipment. The CBEMA curve was adapted from IEEE Standard 446 (Recommended Practice for Emergency and Standby Power Systems for Industrial and Commercial Applications), which is typically used in the analysis of power quality monitoring results [15]. The CBEMA curve is a susceptibility profile with the abscissa representing the duration of the event, while the ordinate indicates the percent of nominal voltage value. In the center of plot is the so-called acceptable area. Voltage values above the envelope are supposed to cause malfunctions such as insulation failure and over voltages. Voltages below the envelope are assumed to cause the load to drop out due to lack of energy. In other words, the

concept is that if the supply voltage stays within the acceptable power area then the sensitive equipment will operate normally.

LOGGER				
START 09/08/17 13:08:18		EVENT 1 / 41		
		0:30:01	U P ←	
DATE	TIME	TYPE	LEVEL	DURATION
09/08/17	13:08:54:751	A DIP	153.4 U	0:00:00:640
09/08/17	13:10:19:501	A SWL	300.5 U	0:00:36:541
09/08/17	13:11:42:033	A DIP	167.9 U	0:00:00:020
09/08/17	13:11:42:552	A DIP	185.0 U	0:00:00:030
09/08/17	13:11:42:562	A TRA	> 100U	
09/08/17	13:12:05:023	A CHG	13.4 U	0:00:03:010
09/08/17	13:12:09:653	A CHG	13.3 U	0:00:02:940
09/08/17	13:12:59:513	A DIP	201.6 U	0:00:05:511
09/08/17	13:13:35:793	A SWL	276.5 U	0:00:00:251
09/08/17	13:13:42:632	A CHG	14.4 U	0:00:01:241
09/08/17	13:13:49:334	A CHG	14.2 U	0:00:01:240
...	
09/08/17 13:38:19		230V 50Hz 1Ø		EN50160
WAVE EVENT	RMS EVENT	NORMAL	BACK	

Fig.9. Summary of detected disturbances recorded from graphical display of instrument Fluke 435 - 30 minutes test signal.

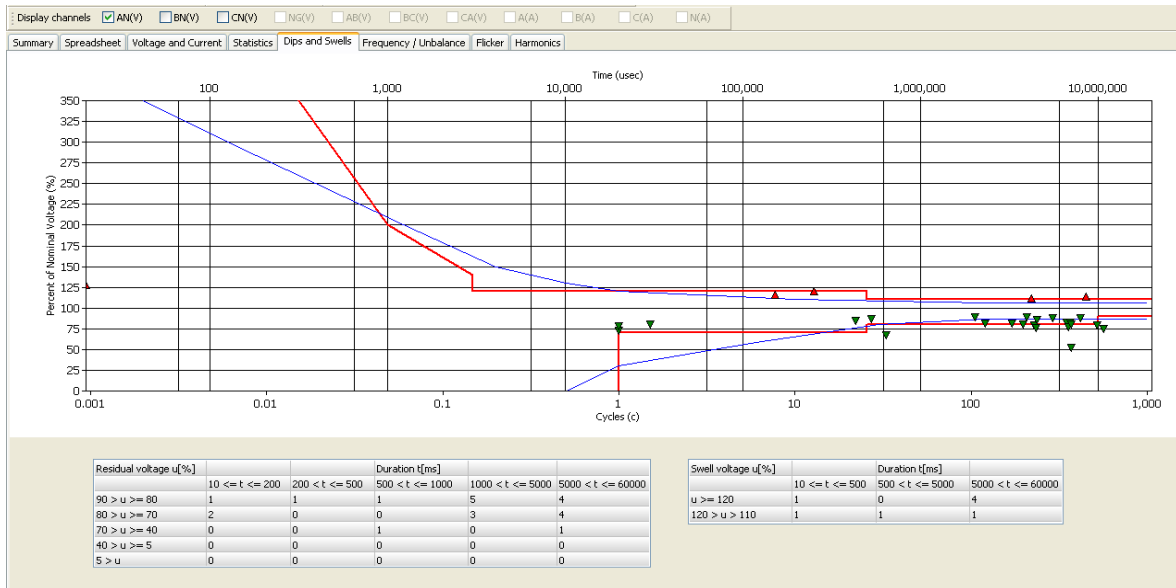
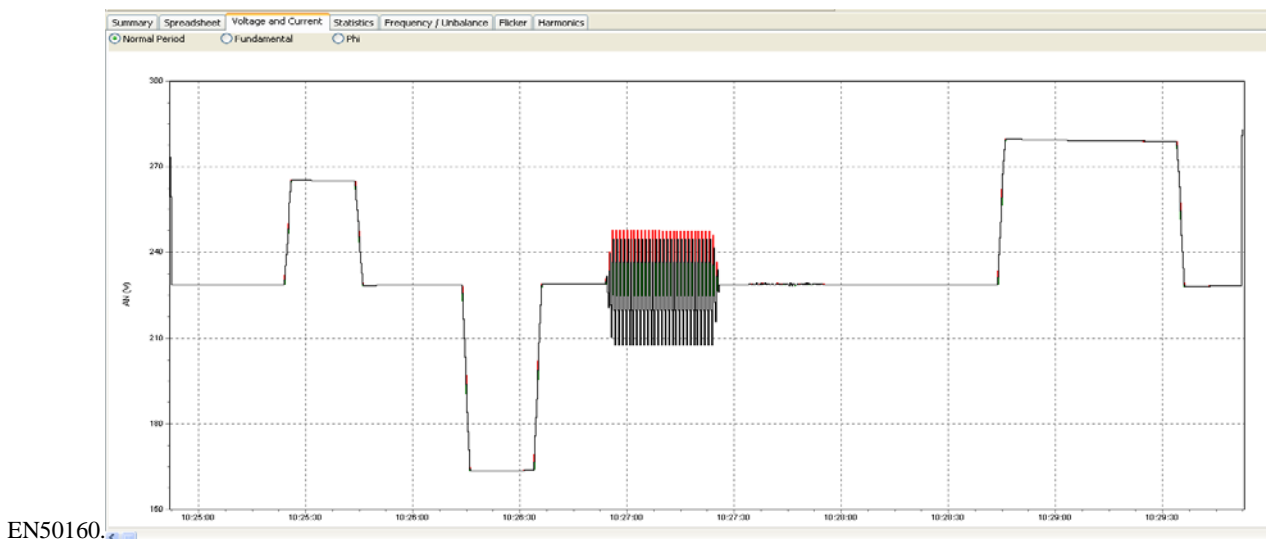


Fig.10. Power Log software analysis of detected signal disturbances according to the quality standard



EN50160.

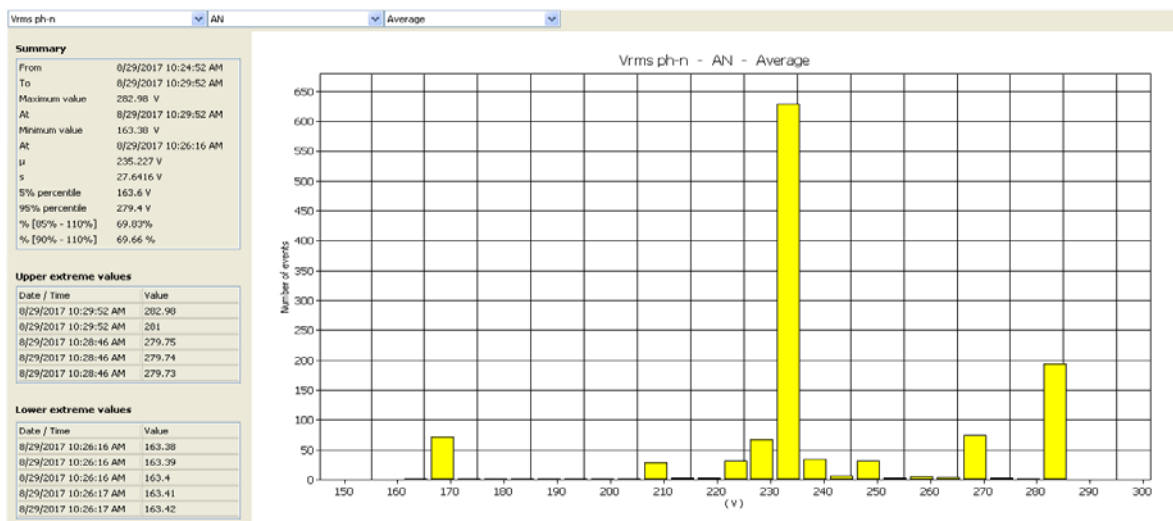


Fig.11. Time diagram (above) and histogram (below) - measured RMS voltage values (300 s long test signal, no harmonics, flicker 10 %).

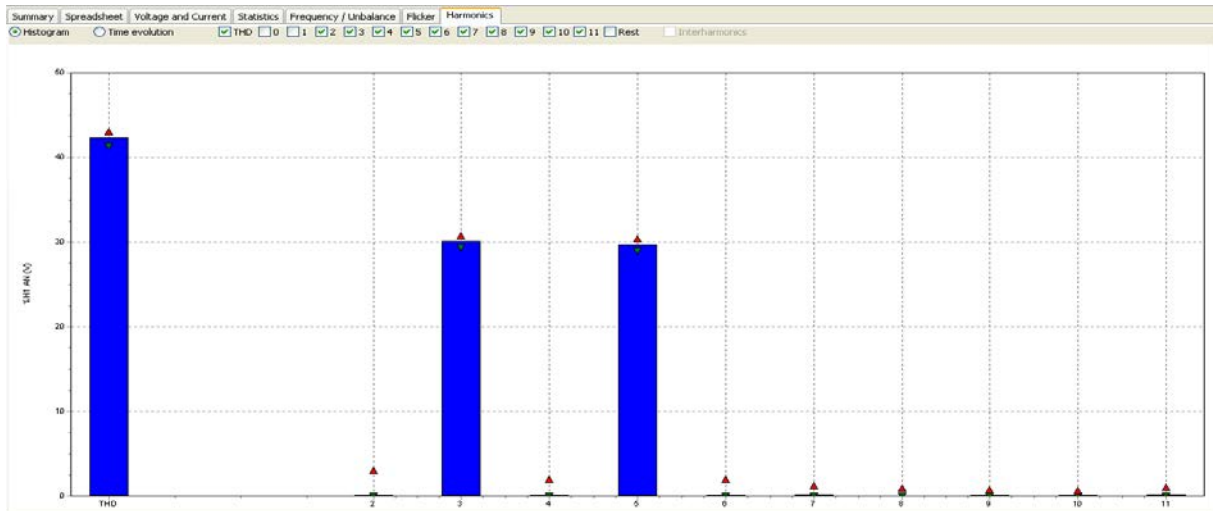


Fig.12. Histogram of measured high-order signal harmonics (total THD value, 30 % of H3 and H5 voltage harmonics).

LOGGER				
START 08/30/17 14:17:55		EVENT 1 / 31		
DATE	TIME	TYPE	LEVEL	DURATION
08/30/17	14:18:07:673	A SWL	266.7 U	0:00:19:711
08/30/17	14:18:37:104	A DIP	163.9 U	0:00:20:761
08/30/17	14:19:09:144	A DIP	206.6 U	0:00:00:130
08/30/17	14:19:10:135	A DIP	206.6 U	0:00:00:140
08/30/17	14:19:11:135	A DIP	206.6 U	0:00:00:140
08/30/17	14:19:12:134	A DIP	206.6 U	0:00:00:140
08/30/17	14:19:13:134	A DIP	206.6 U	0:00:00:140
08/30/17	14:19:14:134	A DIP	206.6 U	0:00:00:140
08/30/17	14:19:15:134	A DIP	206.6 U	0:00:00:140
08/30/17	14:19:16:135	A DIP	206.5 U	0:00:00:140
08/30/17	14:19:17:134	A DIP	206.5 U	0:00:00:140
...
08/30/17 14:19:55		230V 50Hz 1Ø		EN50160
WAVE	RMS	NORMAL	BACK	
EVENT	EVENT	DETAIL		

a) 10 % flicker amplitude, no harmonics

LOGGER				
START 08/29/17 09:52:24		EVENT 2 / 64		
DATE	TIME	TYPE	LEVEL	DURATION
08/29/17	09:52:56:950	A SWL	266.1 U	0:00:21:440
08/29/17	09:53:47:580	A DIP	177.3 U	0:00:19:800
08/29/17	09:54:26:651	A SWL	254.4 U	0:00:00:270
08/29/17	09:54:27:460	A SWL	275.0 U	0:00:00:461
08/29/17	09:54:28:440	A SWL	290.2 U	0:00:00:481
08/29/17	09:54:29:171	A DIP	206.9 U	0:00:00:080
08/29/17	09:54:29:441	A SWL	290.2 U	0:00:00:480
08/29/17	09:54:30:171	A DIP	206.9 U	0:00:00:080
08/29/17	09:54:30:440	A SWL	290.2 U	0:00:00:481
08/29/17	09:54:31:171	A DIP	206.9 U	0:00:00:080
08/29/17	09:54:31:440	A SWL	290.2 U	0:00:00:481
...
08/29/17 09:57:25		230V 50Hz 1Ø		EN50160
WAVE	RMS	NORMAL	BACK	
EVENT	EVENT	DETAIL		

b) 20 % flicker amplitude, 30% H3 and H5 harmonics

Fig.13. Summary of detected VQ disturbances for two different levels of flicker and high-order harmonics in test signals.

Red curve is ITIC Curve - Power Acceptability Curve for Information Technology Equipment. ITIC curve is the modified version of CBEMA power acceptability curve, but the concept remains the same. The intent was to derive a

curve that can better reflect the performances of typical single-phase computers and their peripheral units. Besides the described power curves, in Fig.10. there are shown dips, swells and transient classification table according to the standard EN50160. In this figure, detected voltage dips are presented using green arrows, while detected voltage swells are indicated using red arrows in relation to the percentage nominal voltage values shown on the diagram vertical axis.

Second experiment includes 300 s long test signals generated with combination of voltage swell, dip, flicker, noise and certain level of odd high-order harmonics (specifically 3rd and 5th signal harmonics as most dominant odd harmonics). For test purposes are analyzed cases with the various percentage levels of flicker and noise, without high-order harmonics or with the presence of signal harmonics. For each generated disturbance there are defined various start times and the same disturbance rise time of 2 s. Time diagram and histogram of measured RMS voltage values, regarding the disturbed test signal with presence of short-time flicker, are shown in Fig.11. In this case, reference test signal is generated with voltage swell, voltage dip, 10 % amplitude level flicker, short-time noise, without high-order harmonics and with time duration of 300 s. In time diagram are clearly visible specific disturbances in test signal, first swell and dip, then influence of flicker, small noise level and finally again voltage swell.

For test signal with certain level of high-order harmonics, test scenario is performed similar to the previously presented case, with 300 s time duration, voltage swell, voltage dip and small level of noise, but in this test, in the signal are included 3rd and 5th high-order harmonics with amplitude levels of 30 % and flicker with amplitude level of 20 %. In Fig.12. is shown a histogram of measured high-order signal harmonics, recorded using the Power Log software support, including percentage value of total harmonic distortion - THD factor and measured individual high-order harmonic components – 30 % of H3 and H5 signal harmonics.

Table 2. Summary of events detection using instrument Fluke 435 for various amounts of typical disturbances in test signals.

Default voltage parameters of test signal	Instrument Fluke 435
Percentage levels	Detected VQ events
> 110% of nominal RMS value	voltage swells (SWL)
< 90% of nominal RMS value	voltage dips (DIP)
< 10% of nominal RMS value	rapid changes (CHG)
< 1% of nominal RMS value	interruptions (INT)
> 100 V + nominal RMS value	transients (TRA)
Nominal RMS value + 30% of H3 and H5 signal harmonics	no events, only signal harmonics
20% of flicker amplitude, no signal harmonics	voltage swells (SWL) and dips (DIP)
10% of flicker amplitude, no signal harmonics	voltage dips (DIP)
9% of flicker amplitude, no signal harmonics	no detected events
20% of flicker amplitude + 30% of H3 and H5 harmonics	voltage swells (SWL) and dips (DIP)
3% of flicker amplitude + 30% of H3 and H5 harmonics	voltage swells (SWL)
2% of flicker amplitude + 30% of H3 and H5 harmonics	no detected events
3% of flicker amplitude + 25% of H3 and H5 harmonics	no detected events
100% of noise amplitude	no detected events

An interesting case for analysis is influence of percentage value of flicker amplitude in test signals on disturbance detection. Actually, when flicker occurs in the measured signal, depending on flicker amplitude level, three different cases for events detection are possible: instrument could detect swells, dips, or none of the disturbances. For example, in case of 10 % flicker amplitude the instrument detects combinations of swells and dips. This is clearly confirmed in Fig.13., where are shown detailed summaries of detected disturbances for two examples of voltage test signals, with the different levels of flicker, 10 % flicker amplitude (above) and 20 % flicker amplitude (below). For 10 % flicker amplitude value the instrument detects only dips, while for 20 % flicker amplitude the instrument alternatively detects voltage swells and dips. Generally, detailed software supported analysis of flicker amplitude influence shows that without harmonics for flicker amplitude values greater than 10 % the instrument detects combination of swells and dips, for flicker amplitude value equal to 10 % the instrument will detect only voltage dips, and for flicker percentage amplitude values smaller than 10 % the instrument will not detect presence of voltage disturbances in the test signals. Instrument under test defines Dip and Swell events based on calculated true RMS values within window of a half of each signal period, thus flicker will change detected voltage periodically and generated dip and/or swell each time when limit according to the standard EN50160 is reached. Presence of harmonic in the signal slightly changes the calculated RMS value of measured voltage. Contrary, even high amplitude of noise in test

signal is very good suppressed based on this 10 ms period of integration.

Finally, tabular presentation of signal parameter influence on event detection in tested instrument Fluke 435 can be seen in Table 2.

4. CONCLUSION

An improved generator of long-time complex signals with various combinations of standard VQ disturbances is described in this paper. Developed signal generator is based on virtual instrumentation concept and interpretation of script files. Definition of test sequence in text file enables easy and flexible repeatable testing of VQ instruments, especially during the development phase of detection algorithms, when minutely repetition of long and specific test is required. This system enables generation of long-time test sequences according to predefined complex scenarios, including typical VQ disturbances predefined in accordance with the European quality standard EN50160, in combination with presence of noise, harmonic and flicker in the specified time intervals. As the practical experimental verification of developed signal generator, in this paper is shown a procedure for testing the instrument for detection of standard VQ disturbances Fluke 435. In the first test scenario is analyzed a large number of various disturbances. Second test scenario was focused on an influence of various percentage levels of flicker and high-order harmonics in test signals on the VQ disturbance detection using the instrument Fluke 435. Some characteristic time diagrams of measured parameters, detailed reports and most important, conclusions about detected signal disturbances obtained from the experimental procedure are presented and analyzed in the paper.

REFERENCES

- [1] Simić, M., Kokolanski, Z., Denić, D., Dimcev, V., Živanović, D., Taskovski, D. (2017). Design and evaluation of computer-based electrical power quality signal generator. *Measurement*, 107, 77-88.
- [2] Bollen, M.H.J. (2003). What is power quality? *Electric Power Systems Research*, 66 (1), 5-14.
- [3] Ferrero, A. (2008). Measuring electric power quality: Problems and perspectives. *Measurement*, 41 (2), 121-129.
- [4] Copper Development Association. (2004). *Power quality application guide. Voltage disturbances*. Standard EN 50160.
- [5] Montenegro, D., Hernandez, M.E., Ramos, G.A. (2014). A realistic generator of power quality disturbances for practicing in courses of electrical engineering. *Computer Applications in Engineering Education*, 23 (3), 391-402.
- [6] De la Rosaa, J.G., Pérez, A.A., Salas, J.C., Fernández, J.M., Muñoz, A.M. (2012). A novel virtual instrument for power quality surveillance based in higher-order statistics and case-based reasoning. *Measurement*, 45 (7), 1824-1835.

- [7] Chunling, C., Huihui, Q., Wei, Z., Pengfei, W. (2012). Transient power quality signal generator and detector platform. *Energy Procedia*, 16B, 1380-1385.
- [8] Kumar, V., Kaur, M. (2015). Power quality event generation in MATLAB/Simulink environment. *International Journal of Advanced Research in Electrical, Electronics and Instrumentation Engineering*, 4 (7), 6055-6059.
- [9] Saxena, R., Swami, A.K., Mathur, S. (2012). A power quality signal generator in LabVIEW Environment. In *International Conference on Advances in Electronics, Electrical and Computer Science Engineering - EEC 2012*, 36-39.
- [10] Zhu, W., Ma, W.Y., Gui, Y., Zhang, H.F. (2013). Modelling and simulation of PQ disturbance based on Matlab. *International Journal of Smart Grid and Clean Energy*, 2 (1), 18-24.
- [11] Fluke Corporation. (2012). *Fluke 435 Series II, Three-phase energy and power quality analyzer*. Manual.
- [12] National Instruments Corporation. (2014). *PCIe NI 6343 multifunction data acquisition card - specifications*.
- [13] Kokolanski, Z., Gavrovski, C., Mircevska, I., Dimcev, V., Simić, M. (2016). On the design of power quality signal amplifier. In *International Scientific Conference Electronics (ET 2016)*. IEEE.
- [14] Apex Microtechnology, Inc. (2012). *Power operational amplifiers*. PA97DR - datasheet.
- [15] IEEE. (2000). *Recommended practice for emergency and standby power systems for industrial and commercial applications*. IEEE Standard 446-1995.

Received September 30, 2017.

Accepted March 20, 2018.

Metrological Software Test for Simulating the Method of Determining the Thermocouple Error in Situ During Operation

Jingliang Chen¹, Jun Su¹, Orest Kochan^{1,2}, Mariana Levkiv³

¹Country School of Computer Science, Hubei University of Technology, Wuhan, China

²Department of Measuring Information Technologies, Lviv Polytechnic National University, Bandera Str. 28A, 79013, Lviv, Ukraine

³I. Horbachevsky Ternopil State Medical University, Maidan Voli 1, 46001, Ternopil, Ukraine, levkiv.mo@gmail.com

The simplified metrological software test (MST) for modeling the method of determining the thermocouple (TC) error in situ during operation is considered in the paper. The interaction between the proposed MST and a temperature measuring system is also reflected in order to study the error of determining the TC error in situ during operation. The modelling studies of the random error influence of the temperature measuring system, as well as interference magnitude (both the common and normal mode noises) on the error of determining the TC error in situ during operation using the proposed MST, have been carried out. The noise and interference of the order of 5-6 μV cause the error of about 0.2-0.3°C. It is shown that high noise immunity is essential for accurate temperature measurements using TCs.

Keywords: Thermocouple, determination of TC error in situ, determination of TC error during operation, metrological software test, simulation of measuring channel.

1. INTRODUCTION

Measurement plays an important role in science, industry, and commerce. The influence of metrology can be felt in technics [1], [2], technology [3], [4], economy [5], [6] and science [7]-[9], as well as in the fields of public health and safety [10], law and legal system and forensic studies [11], and in many others. Thus, it is no wonder that a considerable share of GDP in the developed countries belongs to the field of metrology and adjacent fields [12].

There are many measurement techniques and sensors [13] but the temperature is one of the most frequently measured physical quantities. Therefore, thermometry is a very important branch of metrology, and it also has numerous sensors [13]-[16] and techniques [17]-[19]. The importance of thermometry is reflected in the fact that the unit of temperature is one of the basic units of the International System of Units. Therefore, a lot of attention is dedicated to studying trends of thermometry [20] and improvement of the existing temperature scale [21].

Thermocouples (TCs) dominate in temperature measurements within the interval from 600°C to 1500°C [22]. However, they have a lot of sources of error: (i) electromagnetic interference [23]; (ii) data acquisition modules [24]; (iii) the reference junction [25]; (iv) nonlinearity of the conversion characteristic (CC) [22], [26]; (v) transient processes [22]; (vi) the initial deviation of CC

from the nominal one (also called tolerance) at 800°C reaches 6°C [22], [26]; (vii) degradation of TC legs with operating time which leads to their longitudinal inhomogeneity [26]-[28], which is considered the biggest source of error. The latter source causes two interrelated errors: (i) the error due to drift of TC CC, which manifests itself in a stable condition of operation as a gradual change of a CC with time [28], which can reach 8°C for 1000 hours at 800°C; (ii) the error due to acquired under high temperatures during long term operation thermoelectric inhomogeneity (henceforth the error due to acquired thermoelectric inhomogeneity), which manifest itself as the dependence of the developed emf on temperature distribution along the TC legs [29]. The latter error is considered to be the most dangerous when measuring temperature using thermocouples: according to [29] it can even reach 30°C at the measured temperature of 1000°C. Recently, there was proposed the TC based sensor to cope with the error due to inhomogeneity [15], [16]. It decreases the error due to inhomogeneity approximately 10 times [15]. However, this sensor does not decrease the error due to drift of TC CC. It just allows using the known methods [27] to decrease this error in a changeable temperature field of a measured object. The error due to drift is quite well studied and even reliable techniques of its prediction exist [27], but the method [27] works only in stable temperature fields and

does not work in changeable temperature fields. However, the sensor [15], [16] requires methods for temperature control, for instance [30].

Data acquisition systems for TC are being complicated by correction of various errors [24], [25] and implementation of auxiliary procedures [31]-[33]. This makes it difficult to determine their metrological properties. To solve this problem the simulation modeling is widely used [32], [34]. A special software tool, called the metrological software test (MST), was proposed [34]. The MST contains templates of simulation models of typical components of a measuring channel that take into account various components of the error. It allows simulating different values of components of the error, the relations between them, the effect of influence quantities, drifts due to time and temperature, etc. The MST allows determining the reaction of the studied measuring channel to various errors and the efficacy of the error

suppression measures. However, the MST presented in [34] is very complex. The goal of this paper is to create the special simplified MST to study the method of determining the TC error in situ during operation [33] (henceforth the method of determining the TC error). The method [33] is possible only for the sensor proposed in [15], [16].

2. THE METHOD OF DETERMINING THE THERMOCOUPLE ERROR IN SITU DURING OPERATION

The method of determining the TC error [33] using the purposeful change of a temperature field along the TC legs was proposed. A regular TC (i.e., a TC available on the market and described in [13], [22]), labeled as 1, is shown in Fig.1. It is located in the bore of tubular multi-zone furnace 2. Furnace 2 is attached to the wall of object 3 whose temperature is to be measured. The axis of symmetry is 4.

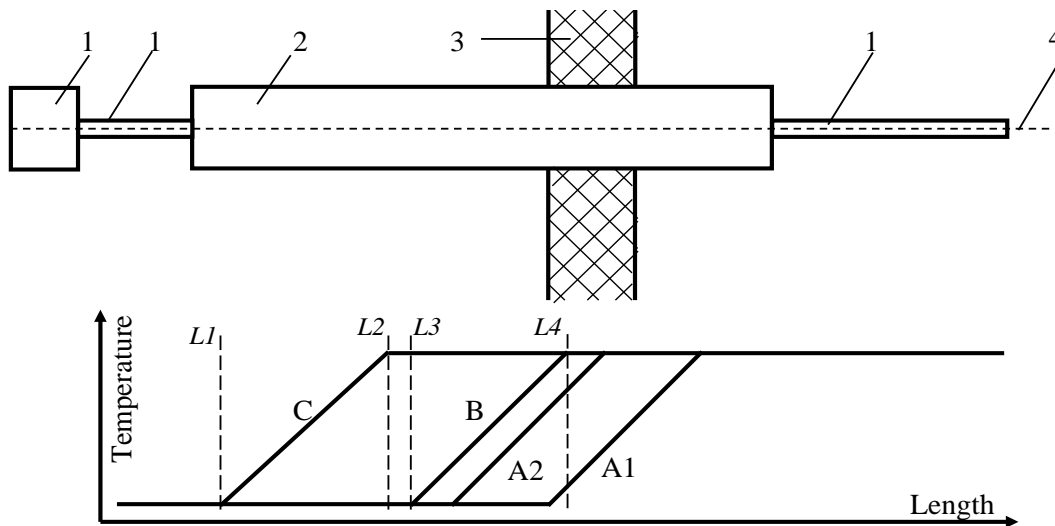


Fig.1. The method of determining the TC error.

The temperature field of object 3 (the temperature field labeled A at the bottom of Fig.1.) changes during operation (for example, within A1 and A2 due to diurnal or weather changes or both simultaneously). In this case, the error due to acquired thermoelectric inhomogeneity appears. Therefore, the first goal of furnace 2 is to stabilize the temperature field profile along the legs of TC 1. Furnace 2 stabilizes temperature field maintaining the temperature field profile labeled B (see Fig.1., lines L3 and L4). Such stabilization does not make it possible for the error due to acquired thermoelectric inhomogeneity of TC 1 to appear.

Thus, the correction of the TC 1 error is reduced to the correction of the individual deviation of TC 1 CC from the nominal one (based on the calibration before operation) and the correction of the error due to drift of the TC 1 CC with operation time. The methods to correct the error due to drift of a TC CC are known [27]. The method for forecasting the error due to drift of a TC CC using neural networks was proposed [27]. This method allows correcting the individual drift of a TC CC based on the results of determining the TC

error. However, the high potential of the method [27] can be only used when a periodic determination of the individual TC error during operation is performed.

Therefore, the second goal of furnace 2 is to carry out a purposeful change in the profile of the temperature field to determine the current error of a TC (the error at a certain instant according to the method described in [33]) in situ during its operation. When determining the TC error, the zone of temperature gradient of the temperature field along TC 1 legs is shifted to the position labeled C (see Fig.1., lines L1 and L2). In the profile of temperature field labeled C, emf is developed by the sections of TC 1 that are usually operated at low temperatures (which means that $L3-L2 > 0$). Therefore, the CC of these sections L1-L2 does not undergo degradation and thus does not drift during operation. If the temperature of the TC 1 measuring junction during this procedure remains constant, then the difference between the emfs developed in the profiles B and C equals the error due to drift of the CC of TC 1 [33]. Before the operation of TC 1, its calibration in the profile of the temperature field C is

necessary. The emf of TC 1 during this calibration is developed only by the section limited by lines L1-L2. Based on the results of this calibration, one will determine the initial error of the TC. The sum of the initial error and the error due to drift equals the current TC error [33]. The TC 1 error will decrease 8-12 times. Thus, the combination of the methods [27] and [33] ensures the high accuracy of temperature measurements.

3. THE STRUCTURE OF THE MST FOR STUDYING THE METHOD OF DETERMINING THE THERMOCOUPLE ERROR

The general structure of the simplified MST, which allows testing the measuring channel in the mode of TC error determination [35], is given in Fig.2. It consists of the following software blocks: (i) the specification of the parameters of profiles of the operation temperature field of the TC and the deviations of the Seebeck coefficient from the nominal one during operation; (ii) the calculation of the temperatures of the endpoints of the virtual sections, into which the TC is split, during operation T_{Li}^{OPER} and during the determination of TC error T_{Li}^{ER} according to the method [33]; (iii) the calculation of the nominal thermo-emf E_i^{NOM} for the virtual sections; (iv) the calculation of the error of the endpoint temperatures of the virtual sections into which the TC is split caused by the errors of the temperature control systems of multi-zone furnace 2; (v) the calculation of the absolute errors of these virtual sections; (vi) the calculation of the actual thermo-emfs of these virtual sections; (viii) three accumulative adders. The accumulative adders calculate both the net nominal and actual thermo-emfs of the TC and its error based on the calculations of the corresponding parameters of the virtual sections.

To study the influence of separate components on the residual error of TC 1 (the error of the correction of the error

due to drift of the CC of TC 1), the coefficients K_{CONT} and K_{DEG} are applied. The coefficient K_{CONT} determines the level of the random error in the systems for setting the profile of temperature field of each zone in furnace 2 during operation and calibration. The error ΔT_{CONT} can be randomly simulated by the formula

$$\Delta T_{CONT} = K_{CONT} \cdot (rnd - 0.5) \quad (1)$$

where rnd – uniformly distributed random variable with limits of change from 0 to 1.

The coefficient K_{DEG} determines the random deviation of the rate of degradation processes in the virtual sections into which TC 1 is split. The error of each virtual section is randomly simulated by the formula

$$\Delta T_{DEG} = K_{DEG} \cdot \Delta e_i \cdot (rnd - 0.5) , \quad (2)$$

where Δe_i - the deviation of the Seebeck coefficient of the i -th section due to degradation of the legs.

The connection block diagram of a temperature measuring system to the MST is given in Fig.3. It includes the MST, whose output generates the nominal value of TC thermo-emf E_{TP}^{NOM} , the actual TC thermo-emf (including the error) E_{TP} and the value of the absolute error of the TC CC ΔE_{TP} . The values of thermo-emf E_{TP}^{NOM} and E_{TP} simulate the thermo-emf developed by the TC in the temperature field of determining the error due to drift of the TC CC and in that of operation. These values are submitted to the temperature measuring system that is currently under test. The random errors of the measuring channel of emf $\Delta \varepsilon^{RND}$ are superimposed with E_{TP}^{NOM} and E_{TP} in this system.

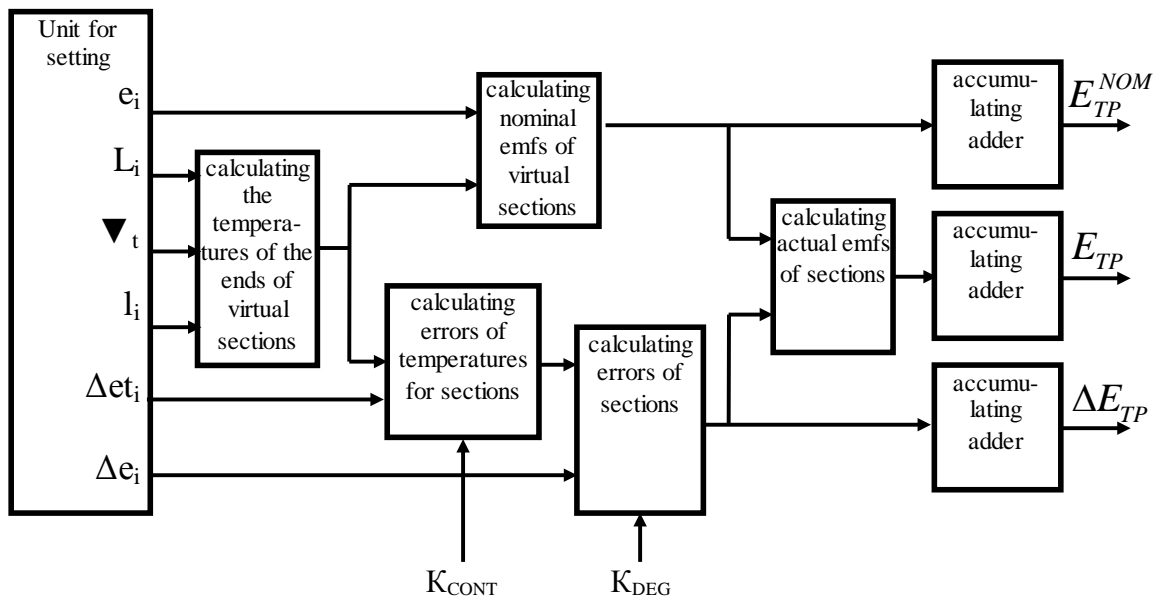


Fig.2. The structure of the simplified MST to test the measuring channel in the mode of determining the TC error during operation.

The values of the error due to noise Δ_{Σ}^{NOISE} are randomly simulated similarly to (1). To study the effect of Δ_{Σ}^{NOISE} on the error determination, the coefficient K_{NOISE} similar to the coefficient K_{CONT} is applied.

Based on the values of thermo-emfs E_{TP}^{NOM} and E_{TP} the temperature measuring system has to determine the error ΔE_{TP}^{SYS} of the main TC, which will be used by the system in the future to correct its error by constructing the individual model of the error due to drift of the TC CC, using, for instance, neural networks as in [27]. The unit analysis of correction error determines the deviation of the error value ΔE_{TP}^{SYS} obtained by the temperature measuring system from the error value ΔE_{TP} determined by the MST. The unit analysis of correction error interprets these deviations as the error of determining the error for the main TC.

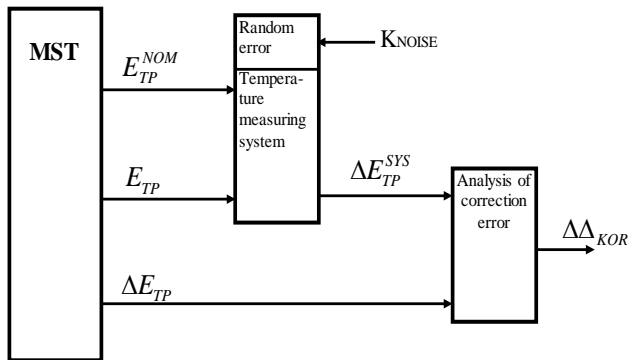


Fig.3. The connection of the temperature measuring system to the MST in the mode of determining the error of the main TC.

4. THE RESULTS OF THE STUDY

A. Influence of the error of temperature control

Firstly, the influence of the error of temperature control of zones in multi-zone furnace 2 (see Fig.1.) on the error of determining the TC error during operation was studied. For this purpose the following values of the coefficient $K_{CONT}=0.1; 1; 10; 100$ were considered. These values correspond to the change in the random error of the systems for setting the profile of temperature field for furnace 2 within the interval $\Delta T_{CONT} \leq 0.00125 \dots 1.25^{\circ}\text{C}$ because type K TCs were studied.

At the same time, the coefficient, which characterizes the rate of degradation in virtual sections, into which TC 1 was split, was given the minimum, that is $K_{DEG}=0.1$. This means that the rate of degradation in all TC 1 virtual sections was very small, that is, $\Delta T_{DEG}=0.00125^{\circ}\text{C}$. The coefficient K_{NOISE} , determining the level of the random error in the measuring channel, was also set as minimum $K_{NOISE}=2$. This means that the voltage of the random error of the measuring channel does not exceed $U_{NOISE} \leq 1 \mu\text{V}$. This corresponds to the temperature error of $\Delta T_{NOISE}=0.025^{\circ}\text{C}$.

The results of the study are presented in Fig.4. In this figure, there are four random realizations with the maximum error of determining the TC error for the abovementioned values of $K_{CONT}=0.1; 1; 10; 100$ (x-axis), $K_{DEG}=0.1$ and $K_{NOISE}=2$ among 50 realizations.

As can be seen from Fig.4., the errors of the systems for setting the profile of temperature field of furnace 2 virtually do not affect the method of determining the TC error. This statement is in accordance with the theoretical study of the influence of the errors of the systems for setting the profile of temperature field. The errors of these systems affect the error of determining the TC error indirectly. These errors determine only the level of the error due to acquired thermoelectric inhomogeneity. Thus, they are the infinitesimals of higher order with respect to the emf developed by the TC.

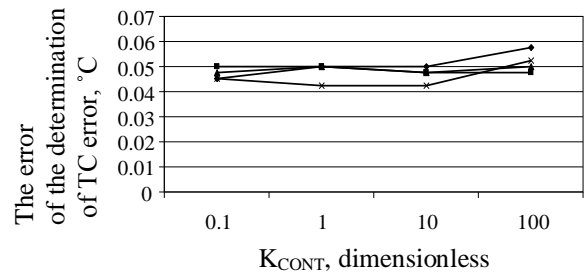


Fig.4. The error of determining the TC error versus the temperature control error of the system of zones in multi-zone furnace 2.

B. Influence of the rate of degradation

Then the influence of the rate of degradation in the virtual sections into which TC 1 is split, on the proposed method of determining the TC error was studied. To carry out this study, the coefficient K_{DEG} was set equal to the following values $K_{DEG}=0.1; 1; 10$. This corresponds to the change of the Seebeck coefficient of type K TC within the interval $\Delta T_{DEG} \leq 0.00125 \dots 0.225^{\circ}\text{C}$, or on 12.5 %. The values of the coefficients $K_{CONT}=0.1$ and $K_{NOISE}=2$ were set as minimum; therefore, the errors caused by them do not exceed $\Delta T_{CONT} \leq 0.00125^{\circ}\text{C}$ and $\Delta T_{NOISE} \leq 0.025^{\circ}\text{C}$, respectively.

The results of the study are given in Fig.5. In this figure, there are four realizations with the maximum error of determining the TC error $\Delta \Delta E_{TC}$ for the values of the coefficients $K_{DEG}=0.1; 1; 10$ (x-axis), $K_{CONT}=0.1$ and $K_{NOISE}=2$ among 50 realizations.

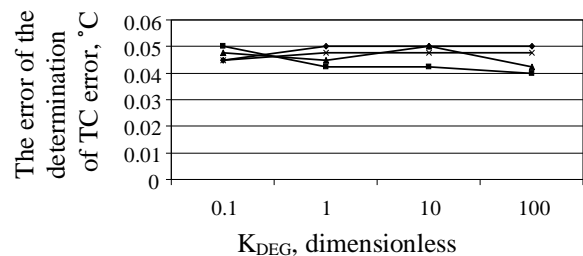


Fig.5. The error of determining the TC error versus the rate of degradation of virtual sections of TC1.

As can be seen from Fig.5., the rate of degradation in the virtual sections, into which TC 1 is split, virtually does not affect the error of determining the TC error during

operation. This statement is in accordance with the theoretical study. This is because the proposed method of determining the TC error is intended to eliminate the influence of the deviation of the individual rate of degradation in TC legs from the typical one.

C. Influence of the random error

The influence of the random error of the measuring channel on the proposed method of determining the TC error was also studied. To carry out this study, the values of the coefficient determining the level of random error were set as follows $K_{NOISE}=2; 10; 50$. This corresponds to the change of the random error within the limits $U_{NOISE}=\pm(1...25)\mu V$, which corresponds to $\Delta T_{NOISE}=\pm(0.025...0.625)^{\circ}C$. The values of the coefficients $K_{CONT}=0.1$ and $K_{DEG}=0.1$ were set as minimum; therefore, the errors caused by them do not exceed $\Delta T_{CONT}\leq 0.00125^{\circ}C$ and $\Delta T_{DEG}\leq 0.00125^{\circ}C$, respectively.

The results of the study are given in Fig.6. In this figure there are realizations with the maximum and minimum errors of the error of determining the TC error $\Delta\Delta E_{TC}$ for the values of the coefficients $K_{NOISE}=2; 10; 50$ (x-axis), $K_{CONT}=0.1$ and $K_{DEG}=0.1$ among 50 realizations. As can be seen from Fig.6., the error of determining the TC error during operation rises strongly with the rise of the random error of a measuring channel. This rise is virtually proportional to the rise of the random error. Thus, the main

source of the error of measurements of the TC CC during the procedure of determining the TC error during operation is the random error of the measuring channel of emf.

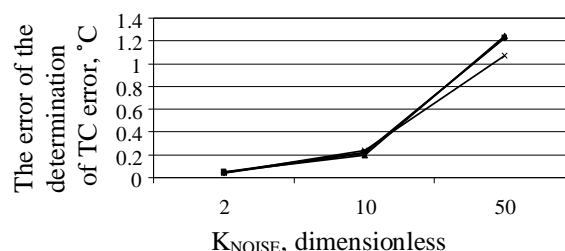


Fig.6. The error of determining the TC error versus the random error of the measuring channel.

D. Decreasing the influence of common and normal mode noises

It should be noted that the random error of a measuring channel of emf usually consists of two components: (i) the noise of the input amplifier of TC emf; (ii) the residual error due to the normal and common mode noises. The effect of the input amplifier's noise can be reduced by an integrated analog-to-digital converter (in particular, dual slope integration or sigma-delta analog to digital converters) and a high-quality operational amplifier.

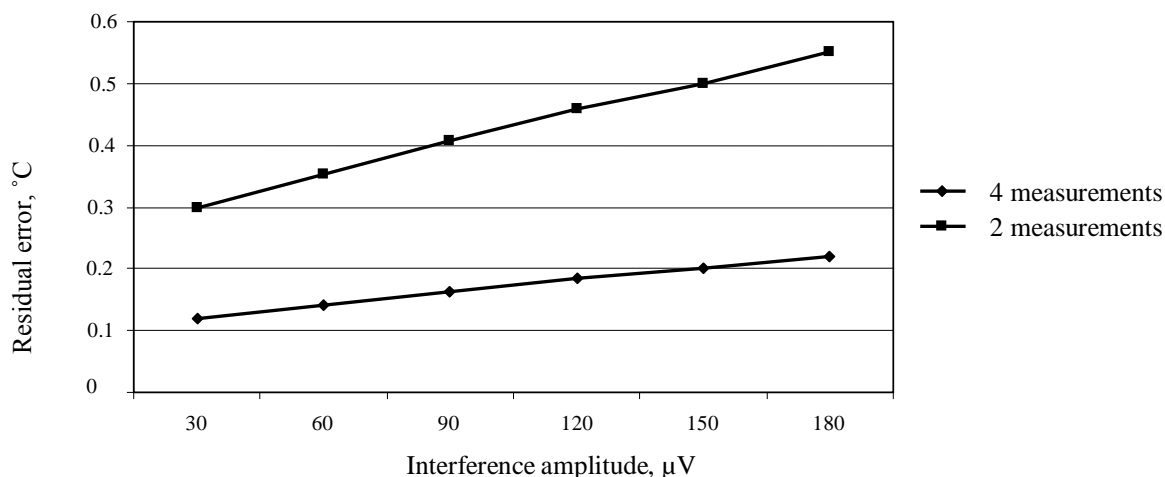


Fig.7. The error of determining the TC error for the discrete averaging of two and four measurement results versus interference amplitude.

Further reduction of the random error can be performed by averaging the results of several replicate measurements. Due to the fact that the input amplifier's noise is close to the white noise, the coefficient of reduction of its effect is proportional to $n^{0.5}$, where n is the number of averaged replicate measurements [36]. The residual error due to the normal and common mode noises is caused by the power grid delivering power supply to a measuring channel. Therefore, within a series of sequential measurements they

have virtually deterministic nature. This fact makes it possible to improve the efficiency of averaging the results of several replicate measurements by increasing the time of measurements. A simpler method for improving the accuracy is averaging of an even number of replicate measurements [37]. In this case, the beginning of each measurement has to be synchronized with the corresponding phase of the power grid voltage. For instance, it is reasonable to average the results of two measurements

whose beginnings are shifted in time on an odd number of halves of the power grid period. Thus, the residual interference during each measurement is shifted by 180° . The error of determining the TC error in this case is given in Fig.7. (the upper straight line) among 50 realizations. The error in this case, in comparison with the errors given in Fig.6., is approximately two times lower, whereas the amplitude of the interference is about four times greater. Even greater accuracy can be achieved by averaging four measurement results, whose beginnings are shifted on an odd number of quarters of the power grid period. Then, the residual interference during each measurement is shifted by 90° . The error of determining the TC error in this case is also given in Fig.7. (the bottom line). As can be seen from Fig.7., the error of determining the TC error decreases even more than twice.

5. CONCLUSIONS

As it is shown in the paper, the random error as well as the normal and common mode noise has considerable effect on the proposed method of determining the TC error [33]. They can significantly increase the error of determining the TC error using the proposed method. The noise and interference of the order of $5\text{-}6\ \mu\text{V}$ is still acceptable. They cause the error of about $0.2\text{-}0.3^\circ\text{C}$. Therefore, high noise immunity is a necessary condition for high accuracy of TC error correction and, consequentially, for accurate temperature measurements.

It should be noted that this paper considers random components of the error of determining the TC error in situ during operation proposed in [33]. The influence of systematic components is considered in [33]. Based on this study as well as on the study [33] the uncertainty budget can be composed for the method of determining the TC error.

As shown in this paper, the effect of the rate of degradation processes and the error of control of temperature field is of the order of few hundredths of a Celsius degree. This effect can be neglected.

It is known that the errors of sensors, in particular TCs, dominate in a measuring channel. A system that uses the investigated method can considerably (ten times or even more) reduce the intercalibration interval. In this case, calibrations occur during the operation. Thus, the accuracy of the temperature measurement and the metrological reliability of the system can be considerably improved. Due to the fact that the investigated method does not require the use of additional equipment (in particular, standards), it significantly increases the metrological autonomy of such systems.

ACKNOWLEDGMENT

This work was supported by Green Industry Technology Leading Project of Hubei University of Technology (No. ZZTS2016004); Foundation of Wuhan Science and technology Bureau (2015030809020370); Doctoral Scientific Research Fund from Hubei University of Technology (No. BSQD14037).

REFERENCES

- [1] Józwick, J., Mika, D. (2015). Diagnostics of workpiece surface condition based on cutting tool vibrations during machining. *Advances in Science and Technology Research Journal*, 9 (26), 57-65.
- [2] Glowacz, A., Glowacz, Z. (2016). Diagnostics of stator faults of the single-phase induction motor using thermal images, MoASoS and selected classifiers. *Measurement*, 93, 86-93.
- [3] Fraczyk, A., Kucharski, J. (2017). Surface temperature control of a rotating cylinder heated by moving inductors. *Applied Thermal Engineering*, 125, 767-779.
- [4] Krolczyk, G.M., Maruda, R.W., Nieslony, P., Wieczorowski, M. (2016). Surface morphology analysis of Duplex Stainless Steel (DSS) in Clean Production using the Power Spectral Density. *Measurement*, 94, 464-470.
- [5] Kočí, V., Maděra, J., Jerman, M., Trník, A., Černý, R. (2014). Determination of the equivalent thermal conductivity of complex material systems with large-scale heterogeneities. *International Journal of Thermal Sciences*, 86, 365-373.
- [6] Novák, M., Náprstková, N., Józwick, J. (2015). Analysis of the surface profile and its material share during the grinding inconel 718 alloy. *Advances in Science and Technology Research Journal*, 9 (26), 41-48.
- [7] Wang, W.L., Zhang, H., Du, X.J., Sun, Y.Y. (2016). PCB-integrated thin film thermocouples for transient temperature measurement. *Electronics Letters*, 52 (13), 1140-1141.
- [8] Mikhaliyeva, M., Hots, N., Mykyychuk, M., Dzikovska, Y. (2017). Use electric and acoustic technologies for automated control of water. In *Advances in Intelligent Systems and Computing: Selected Papers from the International Conference on Computer Science and Information Technologies*. Springer, Vol. 512, 293-303.
- [9] Feldshtein, E., Józwick, J., Legutko, J. (2016). The influence of the conditions of emulsion mist formation on the surface roughness of AISI 1045 steel after finish turning. *Advances in Science and Technology Research Journal*, 10 (30), 144-149.
- [10] Mellal, I., Laghrouche, M., Tien Bui, H. (2017). Field programmable gate array (FPGA) respiratory monitoring system using a flow microsensor and an accelerometer. *Measurement Science Review*, 17 (2), 61-67.
- [11] Ferrero, A., Scotti, V. (2013). Forensic metrology: A new application field for measurement experts across techniques and ethics. *IEEE Instrumentation & Measurement Magazine*, 16 (1), 14-17.
- [12] Birch, J. (2003). *Benefit of legal metrology for the economy and society*. A study for the International Committee of Legal Metrology. https://www.oiml.org/en/files/pdf_e/e002-e03.pdf.
- [13] Webster, J. (1999). *Measurement, Instrumentation, and Sensors Handbook*. CRC Press.

- [14] Childs, P.R.N., Greenwood, J.R., Long, C.A. (2000). Review of temperature measurement. *Review of Scientific Instruments*, 71, 2959-2978.
- [15] Kochan, O., Kochan, R., Bojko, O., Chyrka, M. (2007). Temperature measurement system based on thermocouple with controlled temperature field. In *4th IEEE Workshop on Intelligent Data Acquisition and Advanced Computing Systems: Technology and Applications (IDAACS 2007)*, 6-8 September 2007. IEEE, 47-51.
- [16] Jun, S., Kochan, O., Kochan, V., Wang, C. (2016). Development and investigation of the method for compensating thermoelectric inhomogeneity error. *International Journal of Thermophysics*, 37 (1).
- [17] Maruda, R.W., Krolczyk, G.M., Nieslony, P., Wojciechowski, S., Michalski, M., Legutko, S. (2016). The influence of the cooling conditions on the cutting tool wear and the chip formation mechanism. *Journal of Manufacturing Processes*, 24 (1), 107-115.
- [18] Glowacz, A., Glowacz, A., Glowacz, Z. (2015). Recognition of thermal images of direct current motor with application of area perimeter vector and bayes classifier. *Measurement Science Review*, 15 (3), 119-126.
- [19] Stadnyk, B., Yatsyshyn, S., Skoropad, P. (2012). Research in nanothermometry. Part 4. Amorphous alloys of thermo-resistive thermometry. *Sensors and Transducers*, 141 (6), 1-7.
- [20] Machin, G., Bojkovski, J., del Campo, D. et al. (2014). A European roadmap for thermometry. *International Journal of Thermophysics*, 35 (3-4), 385-394.
- [21] Palenčár, R., Sopkuliak, P., Palenčár, J., Ďuriš, S., Suroviak, E., Halaj, M. (2017). Application of Monte Carlo Method for evaluation of uncertainties of ITS-90 by Standard Platinum Resistance Thermometer. *Measurement Science Review*, 17 (3), 108-116.
- [22] Park, R.M. (1993). *Manual on the Use of Thermocouples in Temperature Measurement*. ASTM International.
- [23] Smalcerz, A., Przulucki, R. (2013). Impact of electromagnetic field upon temperature measurement of induction heated charges. *International Journal of Thermophysics*, 34 (4), 667-679.
- [24] Kochan, R., Kochan, O., Chyrka, M., Vasylykiv, N. Precision data acquisition (DAQ) module with remote reprogramming. In *IEEE Intelligent Data Acquisition and Advanced Computing Systems: Technology and Applications (IDAACS 2005)*, 5-7 September, 2005. IEEE, 279-282.
- [25] Duan, Q. (2009). Research of a cold end temperature compensation for thermal couple. In *IEEE International Conference on Automation and Logistics (ICAL '09)*, 5-7 August, 2009. IEEE, 921-924.
- [26] Körtvélyessy, L. (1998). *Thermoelement Praxis*. Essen, Germany: Vulkan-Verlag. (in German).
- [27] Sachenko, A., Kochan, V., Turchenko, V. (2000). Sensor drift prediction using neural networks. In *International Workshop on Virtual and Intelligent Measurement Systems (VIMS 2000)*, 29-30 April, 2000, 88-92.
- [28] Rogelberg, N., Nuzhnov, A., Pokrovskaya, G. et al. (1969). The stability of the chromel-alumel thermocouples' thermoelectric power at temperatures up to 1200°C. Investigation of alloys for thermocouples. In *Proceedings of the Giprotsvetmetobrabotka*.
- [29] Sloneker, K.C. (2009). Thermocouple inhomogeneity. *Ceramic Industry*, 159 (4), 13-18.
- [30] Vasylykiv, N., Kochan, O., Kochan, R., Chyrka, M. (2009). The control system of the profile of temperature field. In *IEEE International Workshop on Intelligent Data Acquisition and Advanced Computing Systems (IDAACS 2009)*, 21-23 September, 2009. IEEE, 201-206.
- [31] Jun, S., Kochan, O., Kochan, R. (2016). Thermocouples with built-in self-testing. *International Journal of Thermophysics*, 37 (4).
- [32] Woolley, J.W., Woodbury, K.A. (2009). Using computational models to account for thermocouple conduction error in cast metal/mold interfacial heat transfer experiments. In *113th Metalcasting Congress*, 7-10 April 2009, Vol. 117, 31-40.
- [33] Shu, C., Kochan, O. (2013). Method of thermocouples self verification on operation place. *Sensors & Transducers*, 160 (12), 55-61.
- [34] Vasylykiv, N. (2010). Improvement of metrology software test in computer systems of temperature measurement. *International Journal of Computing*, 9 (2), 175-182.
- [35] Jun, S., Kochan, O., Levkiv, M. (2017). Metrological software test for studying the method of thermocouple error determination during operation. In *11th International Conference on Measurement (Measurement 2017)*, 29-31 May, 2017. Bratislava, Slovakia: Institute of Measurement Science SAS, 171-174.
- [36] International Organization for Standardization. (2010). *Guide to the Expression of Uncertainty in Measurement (GUM)*.
- [37] Informa USA, Inc. *Electronic Design*. <http://www.electronicdesign.com/analog/when-1-1-3-db-averaging-adc-channels-improve-nsd>.

Received September 22, 2017.

Accepted March 20, 2018.

Analysis and Calculation of the Fluid Flow and the Temperature Field by Finite Element Modeling

M. Dhamodaran, S. Jegadeesan, R. Praveen Kumar

Department of Electronics and Communication Engineering, M.Kumarasamy College of Engineering, Karur, Tamil Nadu, 639113, India, dhamodaranm@yahoo.com

This paper presents a fundamental and accurate approach to study numerical analysis of fluid flow and heat transfer inside a channel. In this study, the Finite Element Method is used to analyze the channel, which is divided into small subsections. The small subsections are discretized using higher number of domain elements and the corresponding number of nodes. MATLAB codes are developed to be used in the analysis. Simulation results showed that the analyses of fluid flow and temperature are influenced significantly by the changing entrance velocity. Also, there is an apparent effect on the temperature fields due to the presence of an energy source in the middle of the domain. In this paper, the characteristics of flow analysis and heat analysis in a channel have been investigated.

Keywords: Finite Element Method, flow analysis, temperature analysis, entrance velocity, simulation.

1. INTRODUCTION

The finite element method (FEM) is a numerical technique to obtain an approximate solution to a class of problems governed by elliptic partial differential equations. [1]. A simple and effective FEM can be used for fluid flow and temperature flow analysis by developing a MATLAB code. The FEM is nowadays used in industrial applications, including aeronautical, aerospace, automobile, naval, and nuclear construction. A number of general-purpose computer codes are obtainable for industrial users of FEM.

The effect of FEM in the presence of a Poisson's equation for different combinations of velocity boundary conditions with prescribed fluid flow and heat flow at the boundaries has been analyzed. Such a study is beneficial in the appropriate design of many devices and methods, such as mass flow meter, ultrasonic flow meter, thermal mass flow meter, and variable area meters [2]-[4]. The resultant problem is solved using the governing equation. To complete the above goals, the paper is structured as follows. Section 2 is devoted to the numerical technique for mathematical formulation. The finite element analysis is discussed in Section 3. In Section 4 and Section 5, the numerical results presented are discussed, and some important conclusions follow in Section 6.

2. NUMERICAL TECHNIQUE

The goal of the numerical simulations is to determine the relationship between the transmitted energy and the changes in the flow rate of the pipe. For this numerical analysis, a pipe measuring 20 × 50 cm, as shown in Fig.1., is used. The fluid flows around a small pipe located in the middle of the domain

with a uniform velocity V and having a diameter $d = 10$ cm as shown in Fig.1. This small pipe contains an energy source that produces q units of energy per surface area of the pipe per unit time.

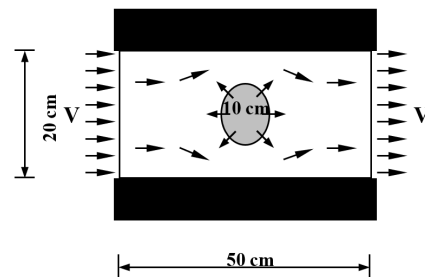


Fig.1. Pipe flow system.

The fluid flow is solved using the stream function for a specific value of entrance velocities [5]. Once the flow is determined, the temperature field can be established by solving the temperature governing equation [6].

The governing equation that governs the two-dimensional problem, in general can be obtained from the below relation:

$$\frac{\partial}{\partial x} \left(R_x \frac{\partial \Phi}{\partial x} \right) + \frac{\partial}{\partial y} \left(R_y \frac{\partial \Phi}{\partial y} \right) + B_x \frac{\partial \Phi}{\partial x} + B_y \frac{\partial \Phi}{\partial y} + G\Phi + H = 0 \text{ in } \Omega$$

$$\Phi = \Phi^* \text{ on } S_1$$

$$R_x \frac{\partial \Phi}{\partial x} n_x + R_y \frac{\partial \Phi}{\partial y} n_y = q^* \text{ on } S_2 \quad (1)$$

The coefficients R_x , R_y , B_x , B_y , G , and H are given as functions of x and y . The two-dimensional domain is denoted by Ω . S is the boundary of the domain, and S_1 and S_2 are parts of that boundary. n_x and n_y represent the outward normal unit vectors on the boundary [7]-[11].

Poisson's equation originates from the general governing partial differential equation, and it is adequate to describe a large number of applied problems including the flow of ideal fluids problems. The two governing equations for the flow of ideal fluids are shown below:

$$\frac{\partial u_x}{\partial y} - \frac{\partial u_y}{\partial x} = 0 \quad (2)$$

$$\frac{\partial u_x}{\partial x} + \frac{\partial u_y}{\partial y} = 0 \quad (3)$$

If we define Ψ such that it identically satisfies the condition for incompressible flow, then we have

$$u_x = +\frac{\partial}{\partial y} \Psi \quad (4)$$

$$u_y = -\frac{\partial}{\partial x} \Psi \quad (5)$$

By substituting equations (4) and (5) into the equation (2), the stream function of the fluid flow can be written as follows:

$$\frac{\partial^2 \Psi}{\partial x^2} + \frac{\partial^2 \Psi}{\partial y^2} = 0 \quad (6)$$

For steady state two-dimensional convection through a constant-property homogenous fluid, the energy equation is given by [7]

$$\frac{\partial}{\partial x} \left(\rho C_p u_x \varphi - k \frac{\partial \varphi}{\partial x} \right) + \frac{\partial}{\partial y} \left(\rho C_p u_y \varphi - k \frac{\partial \varphi}{\partial y} \right) = 0 \quad (7)$$

The above equation can also be rewritten as follows:

$$\frac{\partial}{\partial x} \left(k \frac{\partial \varphi}{\partial x} \right) + \frac{\partial}{\partial y} \left(k \frac{\partial \varphi}{\partial y} \right) - \rho C_p u_x \frac{\partial \varphi}{\partial x} - \rho C_p u_y \frac{\partial \varphi}{\partial y} = 0 \quad (8)$$

Here, φ is the temperature, k is the thermal conductivity of the fluid, and ρC_p is the heat capacity of the fluid. u_x and u_y denote the velocity components in x and y directions, respectively. Since the time-dependency is beyond the scope of this paper, the thermal conductivity of the fluid will be assumed to be time-independent and take a constant value $k = 1.0$. Also, the heat capacity ρC_p is assumed to be equal to 1.0.

In this paper, a two-dimensional steady flow problem is solved using the finite element technique. The flow field of that fluid then resolves the partial differential equations of temperature flow. For both fluid flow and temperature field, boundary conditions are applied. The domain of the problem is discretized to a large number of elements to promise the exactness of the solution. Both the fluid flow and temperature field have been reviewed for various values of entrance velocity.

3. FINITE ELEMENT ANALYSIS

The finite element analysis obtains the temperatures, stresses, flows, or other desired unknown parameters in the FEM by minimizing the energy functional. The energy functional consists of all the energies associated with the particular FEM. Based on the law of conservation of energy, the finite element energy functional must equal to zero. For the numerical simulation of a pipe, MATLAB code using a mesh generator is developed [12]-[14].

A scheme of a main, typical module with discretization is shown in Fig.2. The finite element technique involves dividing the analysis region into several sub-regions. These small regions are the elements, which are linked with adjacent elements at their nodes. Mesh generation is a process of generating the geometric data of the elements and their nodes, and involves computing the coordinate nodes, defining their connectivity, and thus, constructing the elements. Here, mesh designates aggregates of elements, nodes and lines representing their connectivity. Capability and convenience of modeling the analysis domain are dominated by the mesh generation procedure. The geometric characteristics of generated elements affect the overall performance and accuracy of the finite element analysis. Therefore, mesh generation is one of the most important procedures in FEM.

The input data for the mesh generator include the number of generation loops and some geometric coordinates of specific points on each side of each loop. Thus, the total used number of elements is discretized into domain element to maintain the continuity of the degrees of freedom along the edges of the elements. It should be noted, as shown in Fig.3., that the sizes of the elements decrease on getting closer to the small pipe in the middle so as to ensure the accuracy of the solution in this area of concentrated stresses. The mesh discretization is provided in both the flow and temperature analyses.

A problem encountered with the two-dimensional problem analyses is how to number the nodes such that it minimizes the storage needed in the stiffness matrix. The bandwidth of the stiffness matrix depends on the way the nodes have been numbered. Also, the difference between a good numbering scheme and a poor numbering scheme can result in a very large difference in bandwidth requirements. Since finite element equations are related to each other only through common elements, the reduction of the bandwidth needs nodes that are connected by common elements that are as close in numerical value as possible.

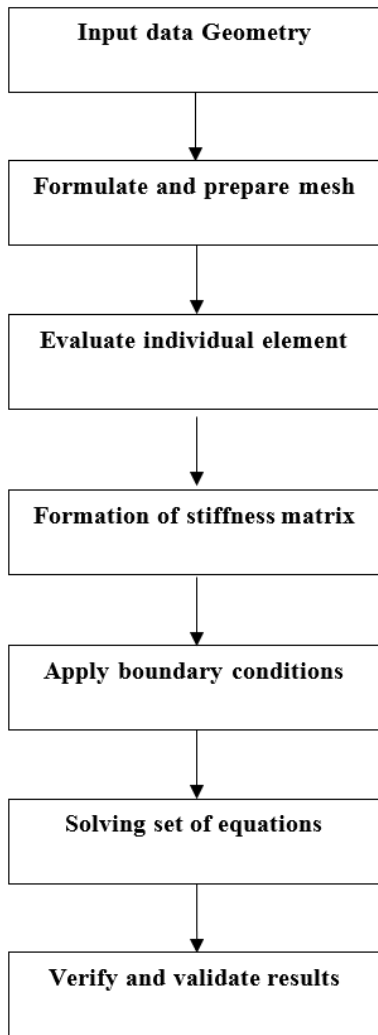


Fig.2. FEM flowchart.

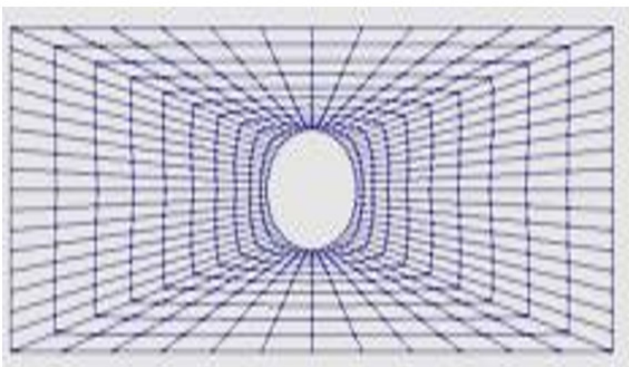


Fig.3. Mesh discretization.

The line connecting these nodes is referred to as the first wave of nodes, as shown in Fig.4. The second wave consists of all nodes that link to nodes in the first wave through common elements. The nodes in the second wave are then given the next consecutive numbers in the new order. This process continues until all nodes have been given new

numbers. Finally, all elements should have node numbers that differ by no more than the number of nodes in the lengthy two consecutive waves, and even less. The output contains the new numbering scheme that will be used in the finite element analysis.

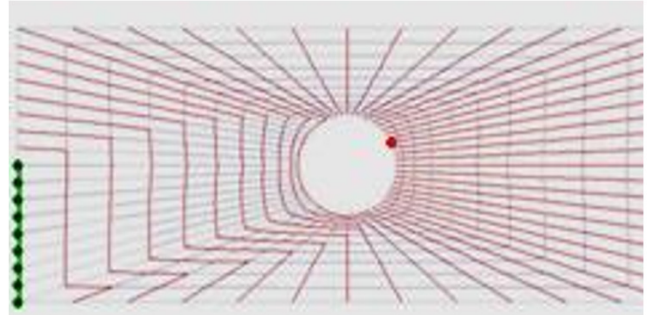


Fig.4. Wave of nodes.

4. FLOW ANALYSIS

Both fluid flow and temperature field can be described by the general equation that governs the two-dimensional problems. However, the coefficients of the governing equation (1) differ from the fluid flow to the temperature field such that they satisfy the governing equations given in equations (6) and (8) for fluid flow and temperature flow, respectively.

Since the flow analysis is characterized by the Poisson's expression; it is recalled here for convenience.

$$\frac{\partial^2 \Psi}{\partial x^2} + \frac{\partial^2 \Psi}{\partial y^2} = 0 \quad (9)$$

The boundary conditions for the fluid flow analysis are illustrated in Fig.5. The x-component of the velocity at the entrance and the exit is constant. u_x is constant specific value for the velocity and y is the y-coordinate of the nodes in that boundary. Since the flow is non-viscous and incompressible, the x-component of the velocity remains constant at the upper and lower boundaries. Thus, the boundary conditions of fluid flow at upper and lower boundaries can be given by the following relations:

$$\Psi = u_x(10) \quad (10)$$

$$\Psi = u_x(-10) \quad (11)$$

The values 10 and -10 are the y-coordinates of the nodes on upper and lower boundaries, respectively. The y-component of the velocity, i.e., u_y is constant and equal to zero. Also, it is maintained the non-viscosity and incompressibility of the fluid. Once the boundary conditions and the coefficients are defined, the analysis of the fluid flow is determined. Results are attained for altered values of the velocity $u_x = 0.0, 0.40, 0.80, \text{ and } 1.0$.

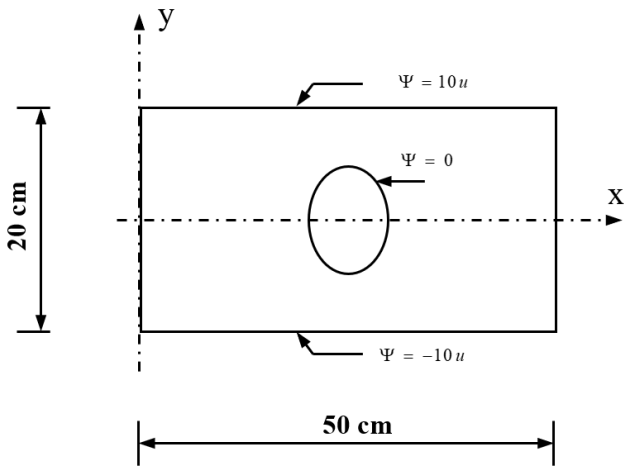


Fig.5. Boundary conditions of the fluid flow.

Fig.6. shows the fluid flow of the different specified values of the entrance velocity. As illustrated in the results, the flow field is the same for all values of the velocities; however, the absolute value of the flow increases with increasing entrance velocity. Also, it is noticed that when the velocity $u_x = 0.0$, the flow field is static and the stream function is constant all over the domain.

The temperature flow is characterized by the energy equation given by equation (8). Here, the coefficients of the general governing equation (1), R_x, R_y, B_x, B_y, G , and H , take the following values; $R_x = k, R_y = k, B_x = -\rho C_p u_x, B_y = -\rho C_p u_y, G = 0.0$, and $H = 0.0$. The thermal conductivity k and the heat capacity of the fluid ρC_p are assumed to have unit values. The coefficients B_x and B_y are functions of velocity components u_x and u_y , respectively. The velocity components u_x and u_y are given by using equations (4) and (5) as derivatives of the fluid flow with respect to x and y , respectively.

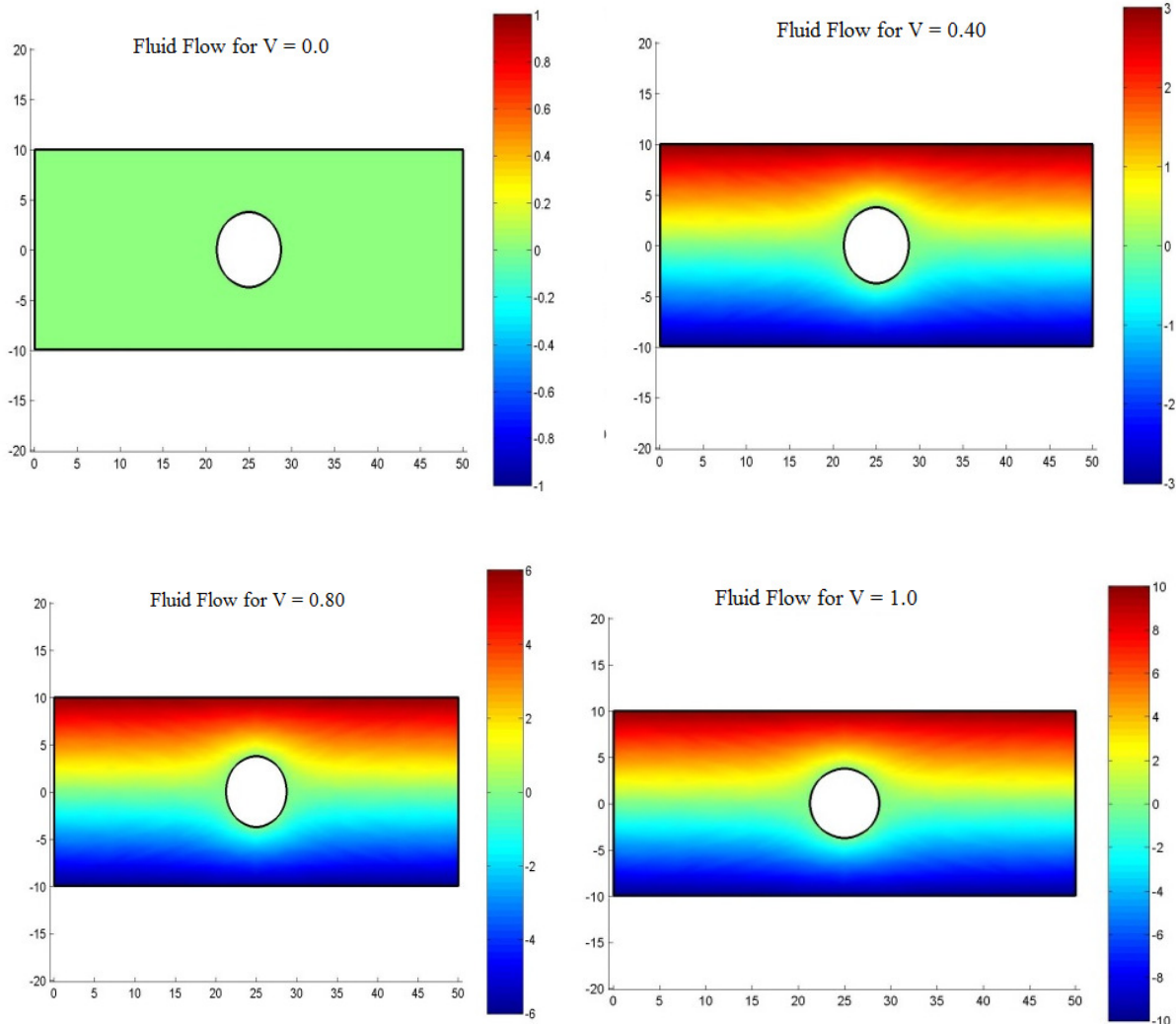


Fig.6. Fluid flow for different values of entrance velocity.

5. TEMPERATURE ANALYSIS

The boundary conditions for the temperature field analysis are illustrated in Fig.7. The small pipe in the middle is assumed to produce q units of energy per surface area of the pipe per unit time. The energy q is considered equal to unity at the small pipe and equal to zero at exit, lower boundary and upper boundary. The temperature flow ϕ is considered equal to zero at the entrance. Once the boundary conditions and the coefficients are defined, the analysis of the temperature field is ascertained.

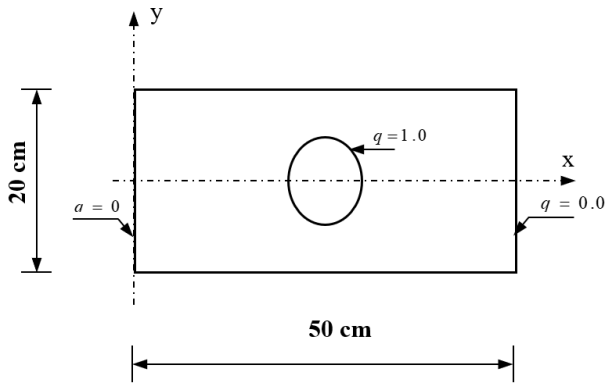


Fig.7. Boundary conditions of the temperature field.

Results are attained for altered values of the velocity, $u_x = 0.0, 0.40, 0.80,$ and 1.0 . Fig.8. shows the flow field of the temperature at different specified values of the entrance velocity. It is noticed from the results that there is a steep decrease in the temperature field with increasing entrance velocity. This coincides with the fact that the heat transferred by convection is greater than heat transferred by conduction. Also, Fig.8. illustrates that the rate of heat transferred through the domain is increasing with increasing velocity, which results in a decrease in temperature near the heat source in the middle of the domain.

In the present study, the flow is considered to be two-dimensional with no difference in the span-wise direction. A partial differential equation is used to represent the flow domain. A series of numerical calculations have been conducted, and the results are presented in order to show the effects of fluid flow and temperature field on temperature distribution in the pipe channel. It should be noted that since the pipe size in the flow direction is relatively coarse, the local heat transfer is not as accurate or detailed as is the case of the x and y directions. However, the resolution is sufficient to aid in the design of pipe for industrial applications and also to provide information and insight into the fluid flow characteristics in the flow direction. In reality, since it is difficult to achieve an adiabatic boundary at the inlet and outlet of the pipe as assumed in the numerical model, a significant portion of the heat loss is transferred to the ambient environment, especially for low fluid flow conditions. Thus, when evaluating the heat transfer in pipe with low fluid flow rates, particular attention should be paid to the effects of this heat loss.

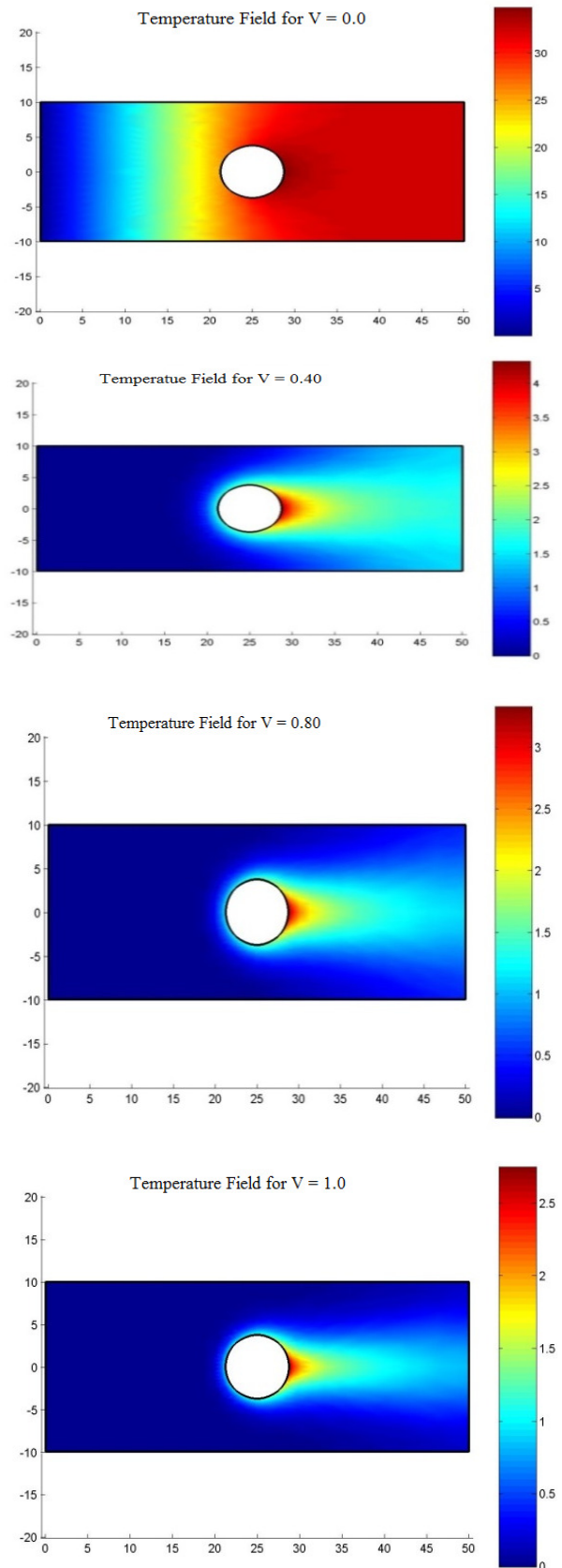


Fig.8. Temperature field for different values of entrance velocity.

6. CONCLUSIONS

In this paper, the numerical simulation of fluid flow and temperature field in a pipe channel for different entrance velocity is analyzed using the FEM through solving partial differential equations of the fluid flow. The fluid flow is expressed by the partial differential equation. The heat transfer is analyzed using the energy equation. The flow field of that fluid is then used to solve the partial differential equations of temperature flow. The flow structure and heat transfer characteristics are studied in detail.

A fundamental and accurate technique is used to compute the steady flow problem using the FEM. The formulation is based on the differential equation and the energy equation. The obtained results show that the fluid flow is characterized by a circulation upwards and that the presence of a mode of heat transfer is purely conductive. The effect of the presence of heat source inside the field of the temperature flow is also inspected. According to these results of this work, we can conclude that our calculation seems to be in concordance with some other works found in the literature for simple geometries. However, the simplicity of the measurement techniques makes FEM a suitable method for steady flow analysis.

NOMENCLATURE

x, y - Cartesian coordinates
Ψ - temperature
k - thermal conductivity
S - the boundary of the domain
S_1, S_2 - part of the boundary
ρC_p - heat capacity
q - energy source
V - velocity
d - diameter
R_x, R_y, B_x, B_y, G, H - coefficients
u_x - velocity of the x component
u_y - velocity of the y component

REFERENCES

- [1] Dhamodaran, M., Dhanasekaran, R. (2014). Comparison of computational electromagnetics for electrostatic analysis. *International Journal of Energy Optimization and Engineering*, 3 (3), 86-100.
- [2] Raine, A.B., Aslam, N., Underwood, C.P., Danaher, S. (2015). Development of an ultrasonic airflow measurement device for ducted air. *Sensors*, 15 (5), 10705-10722.
- [3] Daev, Z.A. (2015). A comparative analysis of the discharge coefficients of variable pressure-drop flowmeters. *Measurement Techniques*, 58 (3), 323-326.
- [4] Jiang, W., Zhang, T., Xu, Y. et al. (2016). The effects of fluid viscosity on the orifice rotameter. *Measurement Science Review*, 16 (2), 87-95.
- [5] Finlayson, B.A. (1970). Convective instability of ferromagnetic fluids. *Journal of Fluid Mechanics*, 40, 753-767.
- [6] Baker, R.C. (2004). The impact of component variation in the manufacturing process on variable area (VA) flowmeter performance. *Flow Measurement and Instrumentation*, 15 (4), 207-213.
- [7] Guiggiani, M. (1999). The evaluation of Cauchy principal value integrals in the boundary element method--a review. *Mathematical and Computer Modelling*, 15 (3), 175-184.
- [8] Schena, E., Massaroni, C., Saccomandi, P., Cecchini, S. (2015). Flow measurement in mechanical ventilation: A review. *Medical Engineering & Physics*, 37 (3), 257-264.
- [9] Ning, J., Peng, J. (2009). A temperature compensation method based on neural net for metal tube rotameter. In *International Conference on Transportation Engineering 2009*. ASCE, 2334-2339.
- [10] Turkowski, M. (2004). Influence of fluid properties on the characteristics of a mechanical oscillator flowmeter. *Measurement*, 35 (1), 11-18.
- [11] Turkowski, M. (2003). Progress towards the optimization of a mechanical oscillator flowmeter. *Flow Measurement and Instrumentation*, 14 (1-2), 13-21.
- [12] Gong, Y., Liu, Q.F., Zhang, C.L., Wu, Y., Rao, Y.R., Peng, G.D. (2015). Microfluidic flow rate detection with a large dynamic range by optical manipulation. *IEEE Photonics Technology Letters*, 27 (23), 2508-2511.
- [13] Sadiku, M.N.O. (2007) *Elements of Electromagnetics*, 4th Edition. Oxford University Press, 740-748.
- [14] Thompson, E.G. (2004) *Introduction to the Finite Element Method: Theory Programming and Applications*. John Wiley & Sons.
- [15] Jin, J. (2002) *Finite Element Method in Electromagnetics*. Wiley.

Received September 12, 2017.

Accepted March 20, 2018.

High Precision Edge Detection Algorithm for Mechanical Parts

Zhenyun Duan¹, Ning Wang¹, Jingshun Fu¹, Wenhui Zhao¹, Boqiang Duan², Jungui Zhao³

¹ School of Mechanical Engineering, Shenyang University of Technology, Shenyang, 110870, People's Republic of China

² College of Aerospace Engineering, Nanjing University of Aeronautics and Astronautics, Nanjing, 210016, People's Republic of China

³ Development Planning Department, China Academy of Launch Vehicle Technology, Beijing, 100076, People's Republic of China, fjs_sut@126.com

High precision and high efficiency measurement is becoming an imperative requirement for a lot of mechanical parts. So in this study, a subpixel-level edge detection algorithm based on the Gaussian integral model is proposed. For this purpose, the step edge normal section line Gaussian integral model of the backlight image is constructed, combined with the point spread function and the single step model. Then gray value of discrete points on the normal section line of pixel edge is calculated by surface interpolation, and the coordinate as well as gray information affected by noise is fitted in accordance with the Gaussian integral model. Therefore, a precise location of a subpixel edge was determined by searching the mean point. Finally, a gear tooth was measured by M&M3525 gear measurement center to verify the proposed algorithm. The theoretical analysis and experimental results show that the local edge fluctuation is reduced effectively by the proposed method in comparison with the existing subpixel edge detection algorithms. The subpixel edge location accuracy and computation speed are improved. And the maximum error of gear tooth profile total deviation is 1.9 μm compared with measurement result with gear measurement center. It indicates that the method has high reliability to meet the requirement of high precision measurement.

Keywords: Vision measurement, edge detection, subpixel-level, Gaussian integral model, normal section line.

1. INTRODUCTION

Mechanical parts are widely used in most major equipment. The high precision and high efficiency measurement for these components is becoming more and more urgent. With the rapid development of non-contact, high precision and automation computer vision technology, the computer vision and its applications become a research hotspot. Vision measurement can quickly and efficiently detect the contours and plane shapes, angles and positions of various complex parts, especially the microscopic detection and quality control of precision components, which achieves the rapid measurement of object size or relative position [1]-[4].

Recently, vision measurement has gradually attracted attention and applications [5]-[6]. How to realize the edge detection is one of key technologies in vision measurement because it decides the measuring accuracy. In order to shift the measuring accuracy, one method is improving the accuracy of measuring equipment, which will increase the measuring expense. Another proper method is subpixel-level measurement. According to current mathematical models, subpixel detection methods can mainly be divided into three types, the moment method, fitting method, and interpolation method [7]-[11]. Among these methods, fitting method has higher positioning accuracy owing to that it can filter off

noise pixels. Thus, as a fitting method, the Facet surface model has been widely used as an image model. This model fits the gray surface with the gray information of discrete digital image to determine the subpixel edge location [12]-[14]. One problem of this model is that it uses all pixels in a symmetrical area with the edge pixel points around, including the image background and foreground, and a few pixel points in transitional zone. So, it may own a large error in the extraction of subpixel edge and low computing efficiency.

Therefore, this study proposes an accurate and efficient subpixel edge detection algorithm based on the Gaussian integral model to realize the high precision measurement of the mechanical parts, such as gauge block and standard involute gear.

2. EDGE CHARACTERISTICS

Step edge and roof edge are two types of common image edges. Edge of backlight image belongs to step edge. So this study focuses on step edge.

The actual lens imaging system is limited by the modulation transfer function (MTF) cutoff frequency. Actual image can be considered as the convolution of imaging point spread function (PSF) and the ideal image

function. The actual edge as shown in Fig.1.a), and the first derivative distribution of actual edge is consistent with Gaussian distribution as shown in Fig.1.b) [15]. It is the same with the point spread function of the imaging system.

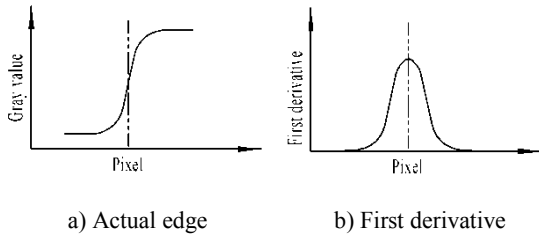


Fig.1. Gray distribution of step edge.

In this study, charge-coupled device (CCD) was used to capture image. According to the square aperture sampling principle, the gray value is equal to the integration of CCD light intensity with the fixed area in a fixed time period. The output results are the pixel gray value of image, which can be expressed as a discrete matrix [16].

3. DETECTION METHOD OF PIXEL EDGE

A. Image smoothing

In the collecting and transferring process of image, some noise is usually produced. It influences the subsequent processing results seriously. So it is important to preprocess the original image to reduce noise after image capture. Image smoothing is a practical digital image processing technology to reduce the noise. A better smoothing method usually eliminates image noise and also guarantees clear image edge contour.

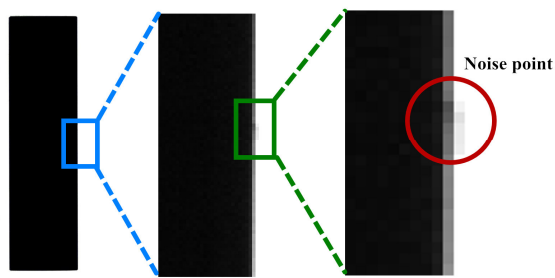


Fig.2. Comparison between original and Gaussian filter processed image.

The most noise signals of image are according to Gaussian distribution. So the Gaussian filter could be an effective method to suppress noise.

One dimensional Gaussian function $G(x)$ was chosen to establish the filter. Basing on the convolution processing of original image $f(i,j)$, the gray value of smooth image $I(i,j)$ can be expressed as

$$I(i,j)=[G(i)G(j)]*f(i,j) \tag{1}$$

Fig.2. shows the original and Gaussian filter processed image. It can be seen that Gaussian filter removes the noise points in the marginal zone. It increases the gray contrast.

B. Edge detection process

In digital image, each target pixel has eight neighborhood pixels except for the boundary one. It is very complex for traditional detection algorithm to calculate first or second order derivative, so as to determine the image edge by means of pixel gray tendency. If the neighborhood pixels are only considered and are not calculated repeatedly, the processing time will be reduced effectively. Therefore, here an eight-neighborhood edge tracking algorithm is proposed to realize edge detection. The process to detect pixel edge is as follows:

1) The gray value of each pixel is first scanned by column. If the gray value of a point $f(i,j) \geq T$, then this point (x_r, y_r) is considered as the edge of the starting point, its coordinate is noted as tag to avoid repeating track. As shown in Fig.3., this point is marked as starting point P0.

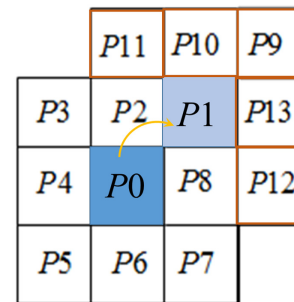


Fig.3. Schematic diagram of edge tracking.

2) After P0 is considered as the starting point of the edge, the maximum gray value point is searched around the eight neighborhoods of the point P0. The maximum gray value point is considered as the next edge point of the image, named as P1. After that the point P1 is marked as the next edge point. According to the two existing edge points P0, P1 and characteristics of single pixel edge, the next maximum gray value point after P1 cannot be P2 and P8. So the gray value of these two points is cleared. When searching the maximum gray value point around the eight neighborhoods of the point P1, the maximum point is only one of the P9 to P13. So, these points can only be calculated, which greatly reduces the computing complexity.

3) When the searching point is located at the boundary or starting point of the image, the edge extraction is finished, else repeat the process.

4. SUBPIXEL EDGE DETECTION

Subpixel edge point is located in the normal direction of the edge section line. In order to determine accurate position, Gaussian integral model is established to obtain the location of subpixel edge by searching the mean point.

A. Establishing the Gaussian integral model

According to the above analysis, the PSF [17] can be expressed by

$$p(t) = \frac{1}{\sqrt{2\pi}\sigma} e^{-\frac{(t-u)^2}{2\sigma^2}} \quad (2)$$

where t denotes the impacted point coordinate, u is the spread point coordinate, and σ is the standard deviation.

The ideal step edge can be defined as

$$E(t) = \begin{cases} g & t \leq \mu \\ g+k & t > \mu \end{cases} \quad (3)$$

where μ denotes edge, and k is the gray values difference between the background and prospect.

The theoretical gray value of an image can be expressed as follows:

$$\begin{aligned} P(t) &= \int_{-\infty}^{+\infty} p(t)E(t) \\ &= \int_{-\infty}^{\mu} p(t)E(t) + \int_{\mu}^{+\infty} p(t)E(t) \\ &= g + \frac{k}{\sqrt{2\pi}\sigma} \int_{-\infty}^{\mu} e^{-\frac{(t-u)^2}{2\sigma^2}} dt \end{aligned} \quad (4)$$

It is difficult to solve the integral expression directly. In order to obtain the mean point of the Gaussian integral model, the $(t-u)/\sigma$ was replaced by v . Therefore,

$$\begin{aligned} P(t) &= g + \frac{k}{\sqrt{2\pi}} \int_{-\infty}^{\frac{t-\mu}{\sigma}} e^{-\frac{v^2}{2}} dv \\ &= g + k\phi(v) = g + k\phi\left(\frac{t-\mu}{\sigma}\right) \end{aligned} \quad (5)$$

According to the standard normal distribution table, the upper limit of the integral in (5) can be defined as $a_i = t_i - \mu/\sigma$.

According to the minimum mean square error principle of least-squares fitting, we can obtain

$$\sum_{i=-N}^N (t_i - \mu - a_i\sigma)^2 = C \quad (6)$$

Then, the partial derivative of C to μ and σ is set equal to zero.

$$\begin{cases} \frac{\partial C}{\partial \mu} = 2 \sum_{i=-N}^N (t_i - \mu - a_i\sigma) = 0 \\ \frac{\partial C}{\partial \sigma} = 2 \sum_{i=-N}^N (a_i t_i - a_i \mu - a_i^2 \sigma) = 0 \end{cases} \quad (7)$$

This can be further solved to obtain

$$\begin{cases} \mu = \bar{t}_i - \sigma \cdot \frac{\bar{t}_i \cdot \bar{a}_i - \bar{t}_i \bar{a}_i}{\bar{a}_i \cdot \bar{a}_i - \bar{a}_i^2} \\ \sigma = \frac{\bar{t}_i \cdot \bar{a}_i - \bar{t}_i \bar{a}_i}{\bar{a}_i \cdot \bar{a}_i - \bar{a}_i^2} \end{cases} \quad (8)$$

Where \bar{t}_i , \bar{a}_i , $\bar{t}_i \bar{a}_i$, and \bar{a}_i^2 denote the arithmetic mean value of t_i , a_i , $t_i a_i$, a_i^2 , respectively.

μ denotes the distance between subpixel edge points in normal section line and pixel edge points, t denotes the distance between discrete points on the normal section line and pixel edge points. As shown in Fig.4., the coordinates of subpixel edge points can be easily obtained.

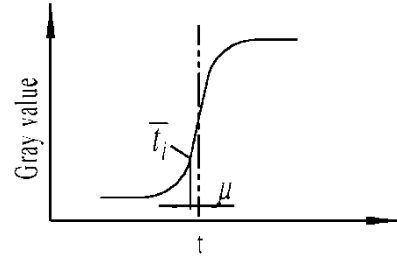


Fig.4. Gaussian integral model on normal section line.

B. Solution method for the proposed model

The subpixel edge information could be obtained by solving the above Gaussian integral model. The solving process to locate the subpixel edge involves:

1) The pixel edge of image was first thrice fitted with the least-squares method. Then the pixel edge points were obtained by discretizing the fitting curve. The normal section line of each pixel edge point was also determined based on the fitting curve.

2) The normal offset curve could be obtained on each side of the pixel edge-fitting curve by choosing a series of equidistant lines in arithmetic progression. Then the Gaussian integral model fitting points can be determined by finding the intersections of the normal section line and the normal offset curve.

3) The gray value of fitting points was given to the Gaussian integral model by using Bezier surface interpolation. Then, the initial gray value of fitting point was filtered along the tangential direction of the normal offset

curve with the Gaussian filter method. Lastly, the final gray value of the fitting points was obtained.

4) The gray values of discrete points in normal section line of pixel edge were fitted based on Gaussian integral model. Then the coordinates of subpixel edge were obtained according to the mean point μ of the Gaussian integral model using (8).

5. EXPERIMENT

The vision measurement system was designed as shown in Fig.5. It mainly consists of a CCD camera, double telecentric lens, LED blue light, digital controller, guide rail slider and holder. It can be used for the measurement of mechanical parts.

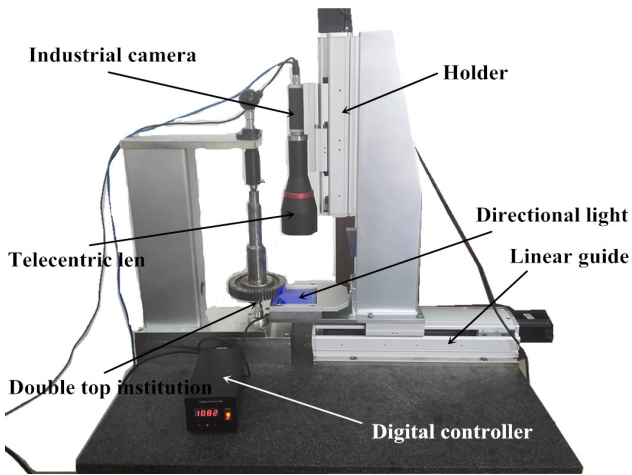


Fig.5. Vision measurement system.

A. Error analysis of subpixel location

According to the JJG2056-90 standard verification system for length measuring instruments, the accuracy of the first-grade gauge block with the size of 1 mm to 10 mm is below 0.05 μm . Due to its high accuracy and simple edge, the first-grade gauge block with the size of 5 mm in different positions was used for verification of the above algorithm. Fig.6. shows the images of the gauge block image with the size of 5 mm in different positions. In order to analyze the accuracy of the algorithm, the proposed algorithm and Facet surface fitting method were compared to detect the subpixel edge of the gauge block.

Owing to the high quality of the gauge block edge, the result of each image processing shows the same character. It illustrates that the position of image has no effect on the image processing. Therefore, the lower edge of the gauge block was taken, for example, to verify the proposed algorithm as shown in Fig.7. First, seven normal offset curves on each side of the pixel edge fitting curve were obtained symmetrically, each interval between equidistant lines can be expressed by arithmetic progression, of which the first term is 0.3 and the common difference is 0.1. Thus, fifteen discrete points on the pixel edge normal section line were chosen for fitting. For example, certain point coordinate on the fitting pixel edge is (1289.994, 1253.711),

its normal direction angle is 2.94°. The discrete points information corresponding to this point is provided in Table 1., and the Gaussian integral fitting curve is shown in Fig.8.

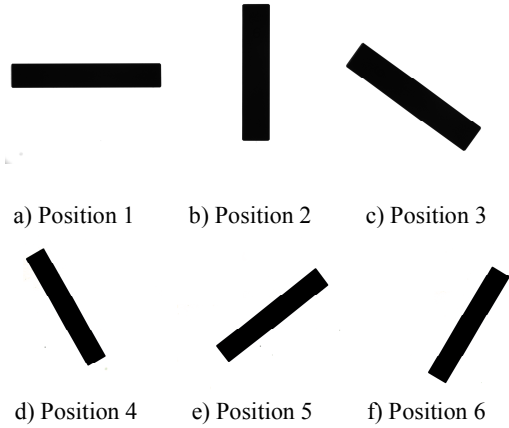


Fig.6. Gauge block image.

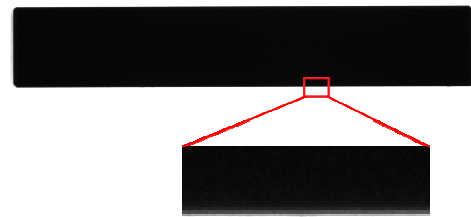


Fig.7. Edge image for vision measurement.

Table 1. Information of discrete points on normal section line of pixel edge.

No.	t/pixel	Gray value	Image coordinates/pixel
1	-4.2	14.384	(1290.204,1249.516)
2	-3.3	17.112	(1290.159,1250.415)
3	-2.5	24.166	(1290.119,1251.214)
4	-1.8	37.819	(1290.084,1251.913)
5	-1.2	57.367	(1290.054,1252.512)
6	-0.7	80.266	(1290.029,1253.012)
7	-0.3	102.108	(1290.007,1253.411)
8	0	119.600	(1289.994, 1253.711)
9	0.3	137.851	(1289.978,1254.010)
10	0.7	162.514	(1289.958, 1254.410)
11	1.2	190.083	(1289.933, 1254.909)
12	1.8	217.823	(1289.903, 1255.508)
13	2.5	238.706	(1289.868, 1256.208)
14	3.3	254.586	(1289.828,1257.007)
15	4.2	254.998	(1289.783,1257.905)

The mean value of the Gaussian integral fitting curve is 0.117 pixels. According to the coordinates of pixel edge and normal direction angle, the corresponding coordinate of the subpixel edge is (1289.988, 1253.828).

Fig.9. shows the subpixel detection results obtained by the proposed algorithm and Facet surface fitting algorithm. It concludes that the extracted subpixel in the proposed algorithm is consistent with the Facet surface fitting algorithm, which verifies the proposed algorithm. Fig.10. gives the comparison of the fitted subpixel of the two-edge detection algorithm. As can be seen from the figure, straightness error of local fluctuation in the subpixel edge extracted by the Facet surface fitting algorithm is 6 μm . The straightness of local fluctuation in the subpixel edge is smoother when using the proposed algorithm, with error of 1 μm .

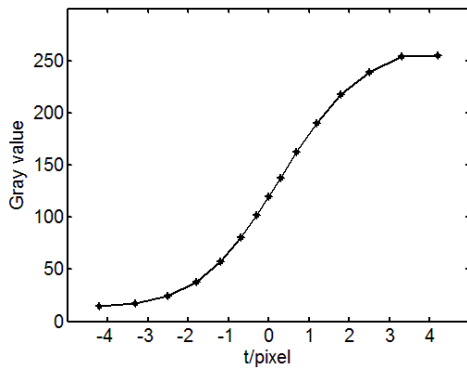


Fig.8. Gaussian integral fitting curve on normal section line.

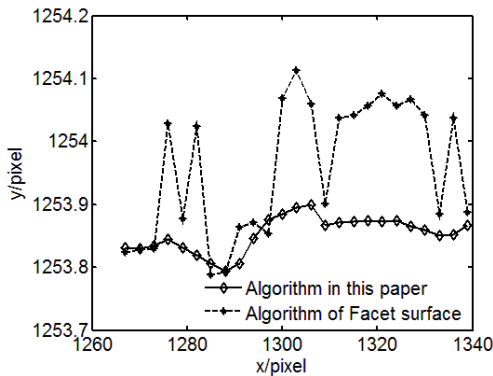


Fig.9. Subpixel edge obtained by the two algorithms.

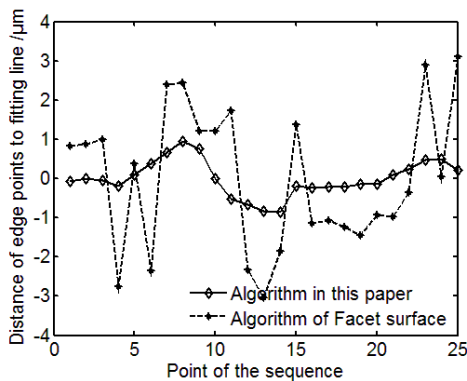


Fig.10. Distance of pixel edge points to the fitting line.

The 5 mm gauge block in a different position was measured to verify the measuring accuracy of this algorithm. Then the subpixel edge of the gauge block was extracted using the two algorithms proposed in this paper and the Facet surface fitting algorithm. One-gauge block edge was first fitted using the least-squares method and then the distance between the points on the other edge and the fitting line was calculated. In that case the measuring size of gauge block can be expressed by the average distance. Then, the measuring error was obtained by comparing the theoretical size with the measured size. The execution time for the proposed algorithm and that of the Facet surface fitting algorithm are 29 ms and 47 ms, respectively. The measuring errors of two algorithms are provided in Table 2. The calculated results indicate that the subpixel edge extraction method of the proposed algorithm is reliable. It generates a smaller measuring error than that of the Facet surface fitting algorithm.

Table 2. Measuring error of two algorithms (μm).

Measuring image	Proposed Algorithm	Algorithm for Facet surface fitting
Position 1	0.914	1.945
Position 2	0.887	1.624
Position 3	0.983	1.817
Position 4	0.873	1.778
Position 5	0.941	1.921
Position 6	1.183	1.883
Average	0.964	1.828

B. Verification using high precision gear

The built-in vision measurement system was calibrated by our previous work [18]. Thus, it can be used to measure tooth profile total deviation of gear. The measured gears are standard involute spur gear. The basic parameters are shown in Table 3.

Table 3. Basic parameters of the measured gear.

Order	Tooth number	Modulus	Grade level
Gear #1	90	2	5
Gear #2	60	2	5

On the basis of obtaining pixel edge of gear profile, each profile was fitted with involute line. Then accurately locating subpixel profile was achieved by the section 4 algorithm. According to the coordinate of gear center [19], the initial phase angle φ_i corresponding to each point of involute tooth profile can be obtained. The gear radius of base circle r_b has been known. So, the tooth profile total deviation of gear can be indicated by using the involute initial phase angle,

$$\varepsilon = r_b \times \left| \max(\varphi_j) - \min(\varphi_j) \right| \quad (9)$$

In order to analyze the accuracy of the measurement method in this paper, the M&M3525 gear measurement center was adopted as shown in Fig.11. The tooth profile total deviation of the gear with the proposed method was compared with the measurement result of gear measurement center.



Fig.11. Gear measurement center.

The measured tooth profile total deviation obtained by two methods is shown in Table 4. M1 is the measurement result of the proposed method. M2 is the measurement result obtained by the gear measurement center. The ΔM is the difference between them. The biggest error of the two methods is smaller than 1.9 μm . And the trend of measurement results is basically the same. It shows that the method in this paper has certain reliability to high accuracy of measurement.

Table 4. Measurement result of two methods (μm).

Measured tooth		Gear #1			Gear #2		
		M ₁	M ₂	ΔM	M ₁	M ₂	ΔM
Tooth 1	Left	5.2	4.8	0.4	4.3	3.2	0.9
	Right	5.1	3.6	1.5	3.4	1.7	1.7
Tooth 2	Left	5.7	5.2	0.5	3.9	2.1	1.8
	Right	4.0	3.6	0.4	4.5	3.6	0.9
Tooth 3	Left	5.9	4.7	1.2	4.1	3.3	0.8
	Right	3.5	2.7	0.8	5.4	3.5	1.9
Tooth 4	Left	5.1	4.2	0.9	5.3	3.6	1.7
	Right	6.3	4.9	1.4	5.4	3.8	1.6

According to the relevant provisions of GB/T 10095, the tooth profile total deviation allowable value of two fifth level spur gear is 7 μm and 6 μm . The measured results show that the tooth profile total deviation obtained by two methods is less than the maximum. We can conclude that the gears meet the accuracy requirement of fifth level gear.

6. CONCLUSIONS

A subpixel edge detection algorithm based on the Gaussian integral model was proposed. The algorithm constructed the step edge normal section Gaussian integral model. Based on the obtained normal of the pixel edge-fitting curve, a Gaussian filter along the tangential of the edge was applied. The gray value of discrete points on the normal section line of the pixel edge was calculated with surface interpolation. This maintains the smoothness of the edge tangential and the steepness of the edge normal. Coordinate and gray information was fitted in accordance with the Gaussian integral model for accurate subpixel location. This approach solved the problem of sensitivity to gray value change by using a gradient to determine the subpixel edge; thus, it has good noise resistance, and it improves the precision of edge detection. In addition, the algorithm adopts curve fitting, reduces the amount of calculation, and improves the calculation speed compared to the Facet surface fitting.

The built-in vision measurement system was calibrated, then, the algorithm was applied to measure the gauge block and standard involute spur gear. The measurement error of first grade gauge block is 0.964 μm , and the tooth profile total deviation measured by this method is compared with the measurement result of the gear measurement center, its maximum error is 1.9 μm , which indicates that the method has high reliability and can meet the requirement of high precision measurement.

ACKNOWLEDGMENT

This work was supported by Funder: Key Projects in the National Science & Technology Pillar Program No.2014BAF08B01.

REFERENCES

- [1] Kumar, B.M, Ratnam, M.M. (2015). Machine vision method for non-contact measurement of surface roughness of a rotating workpiece. *Sensor Review*, 35 (1), 10-19.
- [2] Gadelmawla, E.S. (2011). Computer vision algorithms for measurement and inspection of spur gears. *Measurement*, 44 (9), 1669-1678.
- [3] Kosarevsky, S., Latypov, V. (2013). Detection of screw threads in computed tomography 3D density fields. *Measurement Science Review*, 17 (2), 93-99.
- [4] Robinson, M.J., Oakley, J.P., Cunningham, M.J. (1995). The accuracy of image analysis methods in spur gear metrology. *Measurement Science and Technology*, 6, 860-871.
- [5] Chen, F., Brown, G.M. (2000). Overview of three-dimensional shape measurement using optical methods. *Optical Engineering*, 39 (1), 10-21.
- [6] Lu, N.-G., Deng, W.-Y., Wang, Y.-Q. (2005). Profile measurement of microwave antenna using close range photogrammetry. In *Third International Conference on Experimental Mechanics and Third Conference of the Asian Committee on Experimental Mechanics*, Proc. SPIE 5852, 508-515.

- [7] Sidor, K., Szlachta, A. (2017). The impact of the implementation of edge detection methods on the accuracy of automatic voltage reading. *Measurement Science Review*, 13 (6), 292-297.
- [8] Shang, Y.-C., Chen, J., Tian, J.-W. (2010). The study of sub-pixel edge detection algorithm based on the function curve fitting. In *2nd International Conference on Information Engineering and Computer Science*. IEEE, 1-4.
- [9] Wei, B.-Z., Zhao, Z.-M. (2013). A sub-pixel edge detection algorithm based on Zernike moments. *The Imaging Science Journal*, 61, 436-446.
- [10] Liu, G., Liu, B., Chen, F., Hu, T. (2009). Study on the method of the accuracy evaluation of sub-pixel location operators. *Acta Optica Sinica*, 29, 3446-3451.
- [11] Li, S., Lu, R., Shi, Y. et al. (2011). Sub-pixel edge detection algorithm based on Gaussian Surface Fitting. *Tool Engineer*, 45, 79-82.
- [12] Ma, R., Zeng, L., Lu, Y. (2009). Improved sub-pixel edge detection based on Facet model. *Journal of Basic Science and Engineering*, 17, 296-302.
- [13] Wang, K., Zhang, D., Huang, H. et al., (2005). A study of sub voxel edge detection method based on 3-D Facet model. *Mechanical Science and Technology*, 24, 865-868.
- [14] Xu, L.-Y., Cao, Z.-Q., Zhao, P., Zhou, C. (2017). A new monocular vision measurement method to estimate 3D positions of objects on floor. *International Journal of Automation and Computing*, 14, 159-168.
- [15] Yu, Q.-F., Shang, Y. (2009). *Videometrics: Principles and Research*. Beijing, China: Science Press.
- [16] He, Z., Wang, B. (2003). Sub-pixel extraction algorithm using curve fitting method. *Journal of Scientific Instrument*, 24, 195-197.
- [17] Chang, S.-T., Sun, Z.-Y., Zhang, Y.-Y., Zhu, W. (2014). Radiation measurement of small targets based on PSF. *Optics and Precision Engineering*, 22 (11), 2879-2887.
- [18] Duan, Z.-Y., Wang, N., Zhao, W.-H. et al. (2016). Study on calibration method based on lattice calibration plate in vision measurement system. *Acta Optica Sinica*, 36 (5), 0515004.
- [19] Fei, Z.-G, Xu, X.-J., Anthimos, G. (2016). Short-arc measurement and fitting based on the bidirectional prediction of observed data. *Measurement Science and Technology*, 27 (2), 025013.

Received August 11, 2017.

Accepted March 20, 2018.

The Influence of Measurement Methodology on the Accuracy of Electrical Waveform Distortion Analysis

Jacek Bartman, Bogdan Kwiatkowski

Department of Computer Engineering, Faculty of Mathematics and Natural Sciences, University of Rzeszow, 35-959 Rzeszow, Poland, jbartman@ur.edu.pl

The present paper covers a review of documents that specify measurement methods of voltage waveform distortion. It also presents measurement stages of waveform components that are uncommon in the classic fundamentals of electrotechnics and signal theory, including the creation process of groups and subgroups of harmonics and interharmonics. Moreover, the paper discusses selected distortion factors of periodic waveforms and presents analyses that compare the values of these distortion indices. The measurements were carried out in the cycle per cycle mode and the measurement methodology that was used complies with the IEC 61000-4-7 norm. The studies showed significant discrepancies between the values of analyzed parameters.

Keywords: Distortion measurement, harmonic analysis, inverters, IEC standards, factors of waveforms distortion.

1. INTRODUCTION

Distorted waveforms are the signals with non-sinusoidal time dependence. As far as electrical voltage and current are concerned, distorted waveforms are the results of the use of non-linear electrical energy loads [1]-[4]. Until they were a minor group among electrical energy loads, their work has had little impact. However, their amount is constantly growing, as well as their influence on the shape of voltage and current waveforms. Consequently, the issue of distorted waveform measurements and analyses is becoming more significant.

Periodical waveforms are very often involved when voltage and current waveforms are distorted as a result of non-linear machine work. However, when waveform distortion is the result of the work of electrical switching components, the signal is very often unsteady [5], [6] and has components of frequency from several hundreds of Hz to several tens of kHz, that are not synchronized with the network. This type of signals is not easy to measure and analyze as they comprise both harmonics and interharmonics, slow changing components and fast changing components that additionally can change over time. Such waveform raises two problems:

- minimum number of samples, that guarantees the reflection of fast changing and slow changing components included in distortion, can be very high,
- fundamental Fourier frequency cannot be determined as the frequency of all components is unknown [7].

Modern power quality analyzers have enough memory and are able to sample with such high frequencies, that the

problem mentioned as first can be perceived as burdensome because of increased measurement and calculation costs. The second problem, as far as interharmonics are concerned, fails to allow finding the exact fundamental Fourier frequency. However, there are many (parametric and non-parametric) methods for digital parameter estimation of the fundamental component that allow determining its frequency with acceptable accuracy. Most commonly chosen methods use the spectral analysis [5], [7], [8].

The norms IEC 61000-4-30 [9] and IEC 61000-4-7 [10] are the documents that specify methods of studies and measurements of power quality, including distortions of current and voltage.

The analyses presented in the current paper compare the values given above, for various frequencies of the output of a frequency inverter. They were conducted on the basis of measurements that comply with the norm [10] and made in the cycle per cycle mode

2. MEASUREMENTS STANDARDIZATION

Measurement methodology and requirements for devices used in power quality testing, including current and voltage distortions, were included in the norms IEC 61000-4-30 [9] and IEC 61000-4-7 [10]. There are many references [11], [12] that clarify recommendations or suggestions related to the waveform distortion analysis included in the norms mentioned above.

According to the recommendations of the norms, the frequency analysis of waveforms should include 50

harmonics determined by the DFT method. The width of the time window of the DFT analysis is determined as 200 ms (10 periods 50 Hz), and frequency resolution is 5 Hz. The norm recommends to conduct averaging of selected values in a very short (3 s), short (10 min), and long (2 h) measurement time. Basic measurement of interharmonics should be carried out for 10-period non-overlapping centered subgroups of interharmonics.

In order to determine quantitative waveform distortion, the IEC 61000-4-7 [10] introduces the conception of grouping. It says that the spectrum with 5 Hz frequency obtained as a result of DFT is subject to grouping. The norm defines: a group of harmonics, a subgroup of harmonic, a group of interharmonics, and a subgroup of interharmonics. Assumed by the norm notations:

$Y_{g,h}$ - effective value of a group of h -th harmonic,

$Y_{sg,h}$ - effective value of a subgroup of h -th harmonic,

$Y_{ig,h}$ - effective value of a group of interharmonics that are h -th and $(h+1)$ harmonic,

$Y_{C,(N\bullet h)+k}$ - effective value of spectrum component, that corresponds to an initial bar of DFT of $(N\bullet h)+k$, row,

N - number of periods of fundamental harmonic in a measurement window,

the groups and subgroups mentioned before can be defined.

A) According to the norm, the value of a group of h -th harmonic is determined on the basis of h -th harmonic and of ten neighboring interharmonics. However, only 8 closest values and half of values of the furthest neighbors (Fig.1.):

$$Y_{g,h}^2 = \sum_{k=-(N/2-1)}^{(N/2)-1} Y_{C,(N\bullet h)+k}^2 + \frac{Y_{C,(N\bullet h)-N/2}^2 + Y_{C,(N\bullet h)+N/2}^2}{2} \quad (1)$$

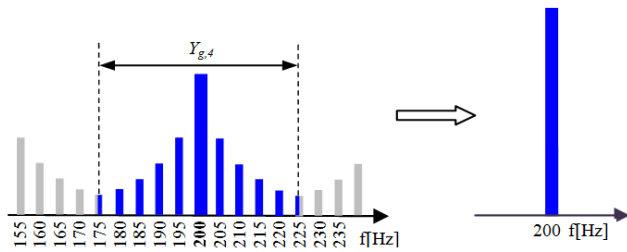


Fig.1. The idea of creating a harmonic group.

B) The value of a subgroup of h -th harmonic is determined on the basis of h -th harmonic and two neighboring interharmonics (Fig.2.):

$$Y_{sg,h}^2 = \sum_{k=-1}^1 Y_{C,(N\bullet h)+k}^2 \quad (2)$$

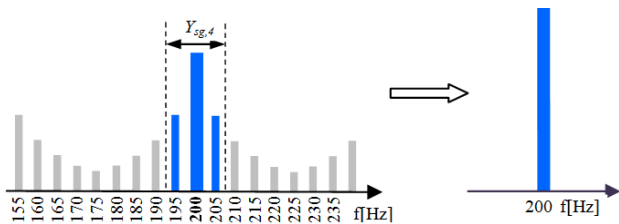


Fig.2. The idea of creating a harmonic subgroup.

C) In order to determine a group of interharmonics that are between h -th and $(h+1)$ harmonic, all bars of a transform that are between the harmonics should be included (Fig.3.):

$$Y_{ig,h}^2 = \sum_{k=1}^{N-1} Y_{C,(N\bullet h)+k}^2 \quad (3)$$

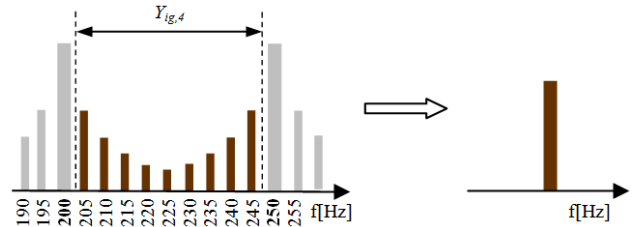


Fig.3. The idea of creating an interharmonic group.

D) In order to determine the value of an interharmonic group, the components that are direct neighbors with harmonic frequencies should be excluded from dependence (3) (Fig.4.):

$$Y_{isg,h}^2 = \sum_{k=2}^{N-2} Y_{C,(N\bullet h)+k}^2 \quad (4)$$

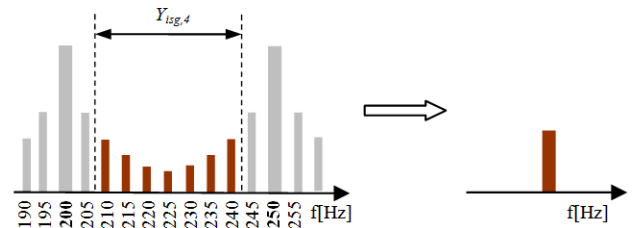


Fig.4. The idea of creating an interharmonic subgroup.

3. EVALUATION OF WAVEFORM DISTORTION

In order to evaluate distortion of a periodical waveform, it is necessary to determine indices which would enable to make the evaluation more objective according to the assumed criteria. Distortion analysis is very often begun with spectrum analysis conducted based on Discrete Fourier Transform - DFT [5], [7], [8], [13]-[18]. According to DFT, the analyzed waveform $y(t)$ with a period T must meet the following conditions of Dirichlet:

- be absolutely integrable, that is:

$$\int_0^T |y(t)| dt < \infty \quad (5)$$

- have a finite number of local extremes within one period,
- have a finite number of discontinuity points first kind, within one period.

In order to properly conduct DFT, it is necessary to select an appropriate sampling period and determine the period of a fundamental component (of minimum width of measurement window) [7], [16], [19]. The width of a measurement window

must be the absolute multiplicity of a period of analyzed waveform and on the accuracy of its determination depends the transform's accuracy. This is not an easy task as far as distorted waveforms that have both harmonics and interharmonics are concerned [5]-[8]. The relevance of this question found reflection in many papers, and many algorithms were created in order to precisely estimate a waveform period [5], [15], [17], [18], [20]. In fact, however, unstable frequency in a waveform makes it impossible to precisely determine a fundamental frequency. As a result, a determined DFT transform is not accurate [15], [16]. However, despite its weaknesses and imperfections, and despite the fact that there are many other methods, DFT is still the most commonly applied method of the distorted waveform analysis. It results from its simplicity and easy implementation.

4. FACTORS OF WAVEFORMS DISTORTION

Various indices that carry different information can be used for the evaluation of waveform distortion. The current paper aims at finding out whether and how measurement methodology influences their results. Thus, the most popular indices used for the evaluation of waveform distortion were selected. The indices used in the paper are compared below:

A. Effective value

The effective value of a periodical waveform is presented with the dependence:

$$X_{RMS} = \sqrt{\frac{1}{T} \int_{t_0}^{t_0+T} f^2(t) dt} = \sqrt{\sum_{k=1}^{\infty} X_k^2} \approx \sqrt{\sum_{k=1}^N X_k^2} \quad (6)$$

In case of current, effective value is described by the value of direct current which flowing through an ideal resistance, being all the time the multiple of a period, causes releasing of energy the same as alternating current simultaneously flowing through.

B. K-th harmonic content factor

The factor of harmonic content determines the contribution of particular components to a signal waveform

$$w_k = \frac{x(k)}{x(1)} \cdot 100\% \quad (7)$$

C. K-th interharmonic content factor

The factor of interharmonic content determines the contribution of particular interharmonics to a signal waveform.

$$w_k = \frac{v(k)}{x(1)} \cdot 100\% \quad (8)$$

D. Total Harmonic Distortion

The THD factor reflects the relation of higher harmonic effective value to a fundamental component effective value:

$$THD = \frac{\sqrt{\sum_{k=2}^N X_k^2}}{X_{(1)}} \quad (9)$$

There are also definitions that define the THD factor as the relation of higher harmonic effective value to a signal effective value. In the paper [21] the author showed that the factor determined by dependence (9) is more useful and unambiguous. Most power analyzers set the value of a THD factor using this dependence, and the analyzer used for the studies described below uses this definition.

E. Crest factor

Crest factor is used for determining the degree of waveform distortion and is defined as the relation of crest value to effective value:

$$CF = \frac{\max|f(t)|}{X_{RMS}} \quad (10)$$

where: $f(t)$ – signal time waveform,
 $X_{(k)}$ – k-th harmonic of signal spectrum,
 $V_{(k)}$ – k-th interharmonic of signal spectrum,
 X_{RMS} – effective value.

In order to gain the accurate assessment of the electrical waveform distortion, the distortion components have to be representative and integral to reality. The authors of numerous works [6], [8], [23], [24], [25], [26] indicate that restriction of the spectrum suggested in the norm [10] to 50 components may be the reason for the discrepancies. In work [23] presents the practical example of the supply voltage on a ship. In the voltage, apart from the fundamental component, there are dominating components with the frequency above 25,000 Hz. In this case the analysis of the waveform distortion requires indicating harmonics with frequencies higher than the frequency of 50 harmonic. The author proves that the THD component, after extending the range of considered harmonics, increases from 1.51 % to 7.9 %. In other works comprising similar issues [24] it was claimed that to monitor the electrical waveform distortion on a ship, it is advisable to apply the THD components which comprise the components with frequencies up to 10 kHz.

The impact of the number of harmonics on the value of the THD component is presented also in the work of [25]. The authors observed that the value of the component calculated to the frequency higher than the frequency switching of the semiconductors' elements of the converter, varies from the value gained according to the IEC standards. That is why the authors claim that a complete harmonic distortion has to be calculated to harmonics higher than the frequency of the converter switch and not to restrict the experiment only to 50 components.

On the contrary, the paper [8] presents the comparison of an original signal with the signal obtained on the basis of the spectrum determined according to the norm [10] – the difference between the recreated signal and the original signal was significant. It was probably caused, among others, by a reduced range of analyzed spectrum, according to the norm [10]. Further studies [6], [26] indicated that narrowing the spectrum of harmonics may affect other parameters that describe electrical waveforms such as effective value (RMS), waveform distortion factor (THD), and crest factor (CF).

5. TESTING STATION

The studies were conducted at a well-prepared measuring stand that comprised the following elements: Emerson Commander SK frequency inverter, 1.5 kW Temal 3Sg90L-4-IE2 induction motor, 1.5 kW Delta ECMA-E21315GS servomotor, Elspec Blackbox G4500 power quality analyzer, MS SQL database server, Microcomputer with PQScada and PQInvestigator softwares dedicated to Elspec Blackbox G4500 analyzer.

While running, a frequency inverter supplies an induction motor. It enables to adjust the frequency of its speed. The motor is loaded with a servomotor mounted on the same bed. Class A Elspec Blackbox G4500 analyzer is responsible for measurements. It has 11 measurement channels that enable simultaneous measurement of voltage and current in each phase. Voltage sampling frequency enables the analysis of up to 511 harmonic components, and in case of current, up to 127 components. Moreover, the device enables the analysis of interharmonics. The analyzer enables simultaneous recording of power quality data according to the norm IEC 61000-4-30 and in the cycle per cycle mode. It is possible thanks to two simultaneously running conversion motors realizing FFT of each cycle for both methods and for all channels.

PQScada software enables to send measurement data from analyzer to the MS-SQL server. Properly configured PQInvestigator application acquires data from the MS-SQL server and enables to conduct analyses and their visualization.

6. RESULTS

Measurements were made at the testing station as described in the previous section of the paper. The values of factors were mentioned in section 3 for various frequencies of a fundamental component, setting various values of frequency of motor supplied voltage (38.1 Hz; 42.5 Hz; 45.8 Hz; 49.7 Hz; 53.7 Hz; 57.6 Hz; 61.6 Hz) and using the analyzer's ability to simultaneous data recording in the cycle per cycle mode (CpC). According to the norm IEC 61000-4-30 (IEC), the values of the factors mentioned in point 3 were compared for various frequencies of a fundamental component.

Fig.5. shows analyzed voltage waveforms which have large distortions. Such comparison shows that reducing the voltage frequency below 50 Hz (45.8 Hz, 42.5 Hz) causes an increasingly fuzzy waveform. It does not occur while raising the frequency above 50 Hz.

The shape of voltage waveforms (Fig.5.) indicates that it comprises many components. Thus, a wide spectrum of harmonics and possibly interharmonics should be expected. Another figure (Fig.6.) presents the initial voltage spectrum for various frequencies related to the fundamental component, and the spectrum of interharmonics expressed in volts. The spectra shown in the first (IEC) column of Fig.6. were recorded in accordance with the norm IEC 61000-4-30 [9]. Their observation leads to the conclusion that distortions of voltage waveform are caused mainly by the third harmonic.

This conclusion is erroneous as in the full spectrum of harmonics, a great contribution of higher components can be observed (second column, Fig.6.). In case of frequencies lower than 50 Hz, a few groups of very high harmonics appear. This justifies the fuzzy time waveforms exactly for these frequencies. The analysis of interharmonics (third column, Fig.6.) indicates that they influence the shape of waveforms, but it is definitely bigger for frequencies above 50 Hz.

The THD factor is a secondary value in regard to the content of particular harmonics. However, it reflects global influence of higher harmonics on the shape of waveforms.

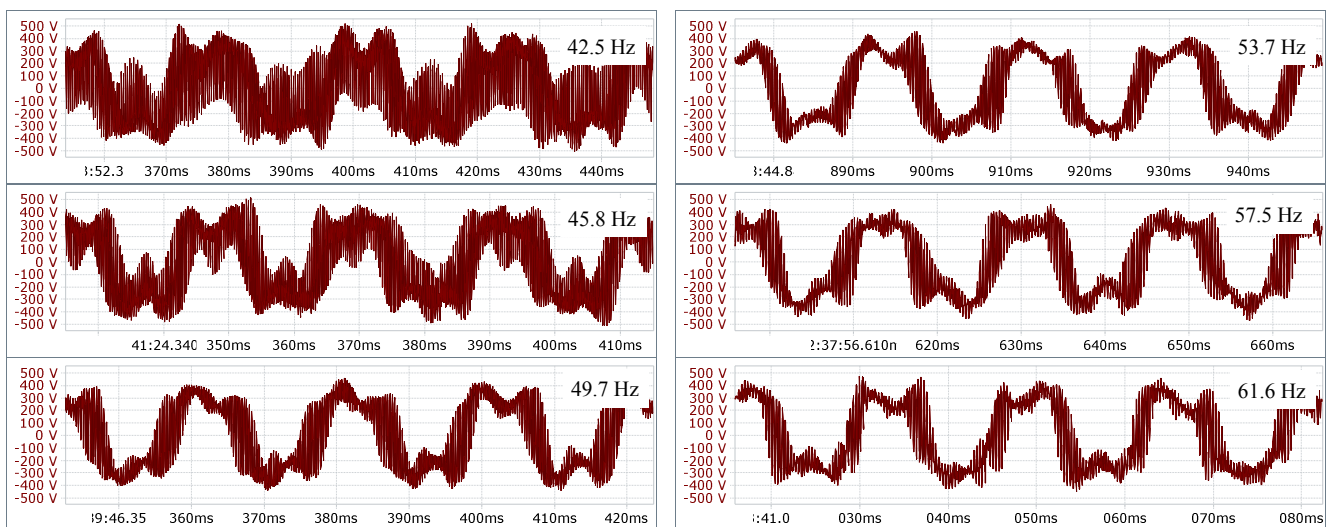


Fig.5. Voltage waveforms for various powering frequencies.

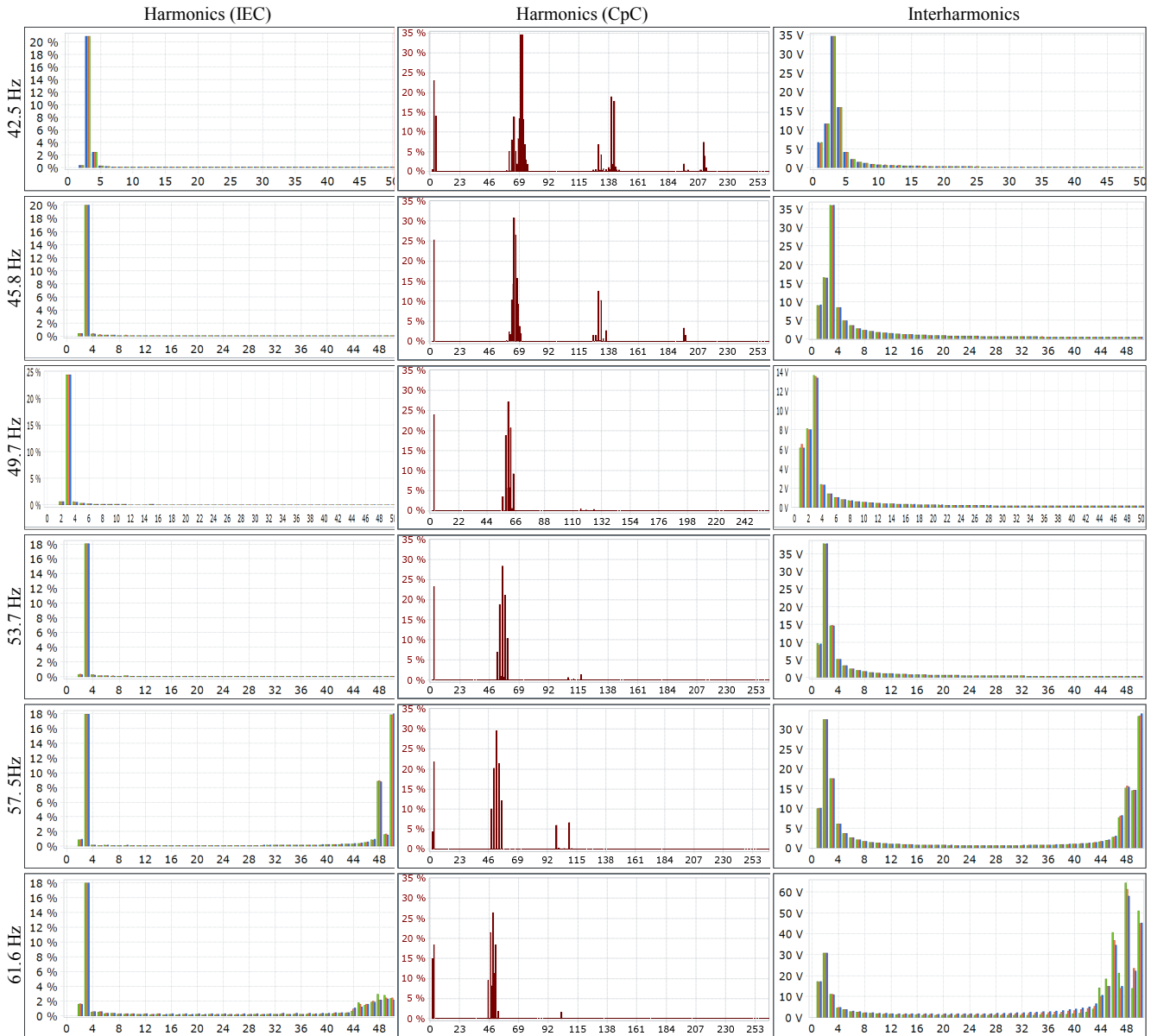


Fig.6. Spectra of harmonics and interharmonics recorded for various voltage frequencies during measurements in the cycle per cycle mode (CpC) and in accordance with the norm [9].

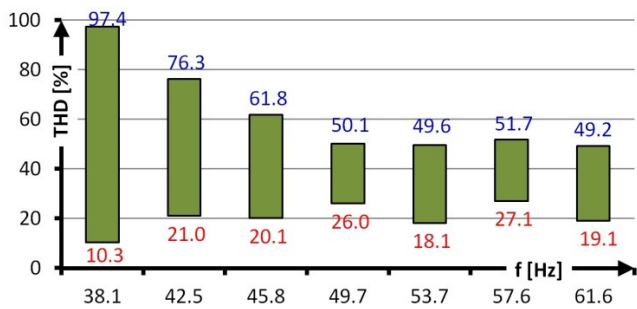


Fig.7. Differences between average values of THD recorded during measurements in the cycle per cycle mode (CpC) and in accordance with the norm [9].

Fig.7. and Fig.8. show a dependence between measurement IEC 61000-4-30 [9] indicating a significantly lower value of THD results of the factor and the assumed methodology. The measurements taken according to the recommendations of the IEC 61000-4-30 [9] norm, show significantly smaller value of the THD factor than the measurements taken cycle after cycle. Analyzing the relation (9) and Fig.7. it can be easily observed that it is caused by not taking into account the harmonics higher than 50 in measurements consistent with the norm. The measurements conducted according to the recommendation of the norm IEC 61000-4-30 [9] indicate that both the value and the changes in THD are small, although they are large according to the cycle per cycle measurements (Fig.8.).

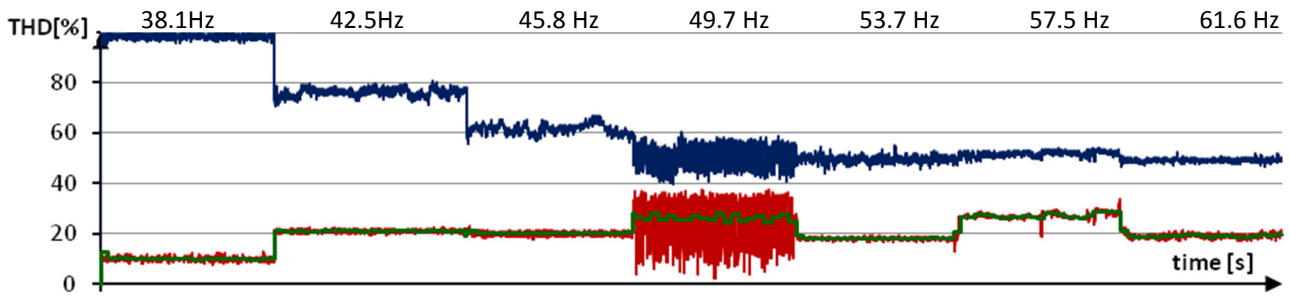


Fig.8. Changes in THD recorded for various voltage frequencies during cycle per cycle measurements (CpC) and in accordance with the norm [9]. Dark blue line – cycle per cycle, red line - analysis in the window with 10 periods, green line – averaged value in the time of 150 periods.

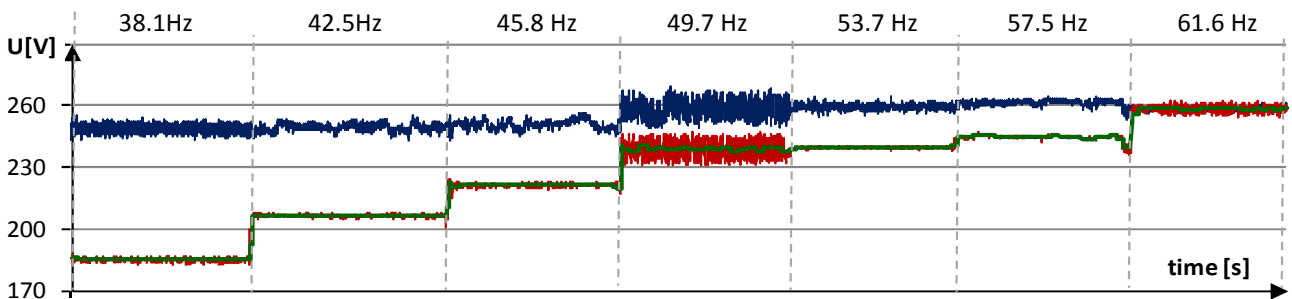


Fig.9. Changes in RMS recorded for various voltage frequencies during cycle per cycle measurements (CpC) and in accordance with the norm [9]. Dark blue line – cycle per cycle including all components, red line - analysis in the window of 10 periods, green line – averaged value in the time of 150 periods.

The measurements of voltage effective value also show great discrepancy between the values measured cycle per cycle and the values measured according to the norm IEC 61000-4-30 (Fig.9.). Similarly to the measurements of THD, the values measured according to the norm are lower than the values measured in the cycle per cycle mode. Discrepancy between the measurements decreases with an increase in frequency of the measured voltage (Fig.10.).

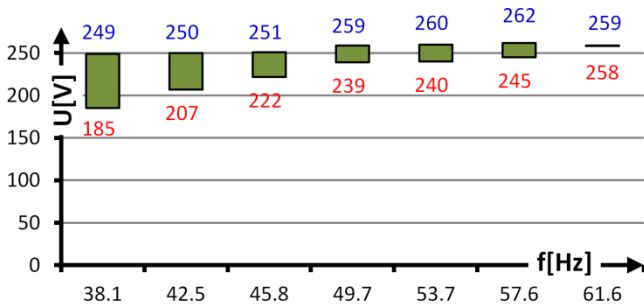


Fig.10. Differences between average values of RMS recorded during cycle per cycle measurements (CpC) and in accordance with the norm IEC 61000-4-30.

Another study compared values of the crest factor set from cycle per cycle measurements and in accordance with the norm [9] (Fig.11.). Similarly, as in the case of THD and RMS, the set values differed. Moreover, the measurements from particular periods taken cycle per cycle were significantly different.

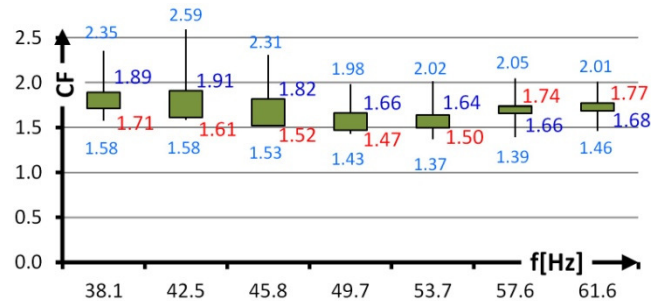


Fig.11. Differences between average values of crest factor recorded during cycle per cycle (CpC) and in accordance with the norm IEC 61000-4-30. Blue color describes minimum and maximum values measured in the CpC.

7. CONCLUSIONS

The paper includes the review of documents that specify measurement methods of voltage waveform distortion. It presents measurement stages of waveform components uncommon in the classic fundamentals of electrotechnics and signal theory, including the creation process of groups and subgroups of harmonics and interharmonics. Moreover, selected distortion indices of distorted waveforms were presented.

The evaluation of voltage and current waveform distortion is crucial as far as the analysis of power quality is concerned. Thus, it should be unambiguous and accurate. Most devices available in the market enable accurate measurements and analyses of mains electricity, according to the norms [9], [10].

The studies presented in the paper showed that using analyzers, which work according to the norms, for measuring highly distorted signals, may result in errors.

The measurement methodology, however, may lead to erroneous results caused by restrictions of spectrum (in accordance with the norms [9], [10]).

REFERENCES

- [1] Shmilovitz, D. (2005). On the definition of total harmonic distortion and its effect on measurement interpretation. *IEEE Transactions on Power Delivery*, 20 (1), 526-528.
- [2] Binkowski, T. (2016). Influence of current sampling frequency on voltage source inverter fuzzy correction. In *13th Selected Issues of Electrical Engineering and Electronics (WZEE)*. IEEE.
- [3] Kamuda, K., Klepacki, D., Kuryło, K., Sabat, W. (2015). Statistical analysis of influence of the low-power non-linear loads on deformation of supply voltage. *Przegląd Elektrotechniczny*, 91 (8), 19-22. (in Polish)
- [4] Sobczynski, D. (2015). A concept of a power electronic converter for a BLDC motor drive system in aviation. *Aviation*, 19 (1), 36-39.
- [5] Rezmer, J., Leonowicz, Z., Gono, R. (2011). Analysis of distorted waveform in power converter systems. *Przegląd Elektrotechniczny*, 87 (1), 254-257.
- [6] Bartman, J. (2017). The analysis of output voltage distortion of inverter for frequency lower than the nominal. *Journal of Electrical Engineering*, 68 (3), 194-199.
- [7] Hanzelka, Z., Bień, A. (2004). *Harmonics. Interharmonics*. Power Quality Application Guide 3.1.1., Copper Development Association.
- [8] Bartman, J. (2016). Accuracy of reflecting the waveforms of current and voltage through their spectrum determined by the standards regulating measurements. *Revue Roumaine des Sciences Techniques - Serie Électrotechnique et Énergétique*, 61 (4), 355-360.
- [9] International Electrotechnical Commission. (2015). Electromagnetic compatibility (EMC) – Part 4-30: Testing and measurement techniques – Power quality measurement methods. IEC 61000-4-30: 2015 RLV.
- [10] International Electrotechnical Commission. (2002). Electromagnetic compatibility (EMC) – Part 4-7: Testing and measurement techniques - General guide on harmonics and interharmonics measurements and instrumentation, for power supply systems and equipment connected thereto. IEC 61000-4-7: 2002(E).
- [11] Bollen, M., Olofsson, M., Larsson, A., Ronnberg, S., Lundmark, M. (2014). Standards for supraharmonics (2 to 150 kHz). *IEEE Electromagnetic Compatibility Magazine*, 3 (1), 114-119.
- [12] Leszczyński, J. (2010). Research on the quality of electricity: A comparative analysis of methods and regulations. *Prace Naukowe: Instytutu Maszyn, Napędów i Pomiarów Elektrycznych Politechniki Wrocławskiej: Studia i Materiały*, 30, 520-534. (in Polish)
- [13] Bartman, J., Kozirowska, A., Kuryło, K., Malska, W. (2011). Analysis of the real electric parameters feed water-pump drive systems. *Przegląd Elektrotechniczny*, 87 (8), 8-11. (in Polish)
- [14] Kozirowska, A., Bartman, J. (2014). The influence of reactive power compensation on the content of higher harmonics in the voltage and current waveforms. *Przegląd Elektrotechniczny*, 90 (1), 136-140.
- [15] Lin, W. (2012). Current harmonics and interharmonics measurement using Recursive Group-Harmonic Current Minimizing Algorithm. *IEEE Transactions on Industrial Electronics*, 59 (2), 1184-1193.
- [16] Pawłowski, M. (2010). Basics of harmonic analysis of distorted currents and voltages in power supply networks. *Mechanizacja i Automatyzacja Górnictwa*, 7, 17-23. (in Polish)
- [17] Petrović, P. (2012). Frequency and parameter estimation of multi-sinusoidal signal. *Measurement Science Review*, 12 (5), 175-183.
- [18] Knežević, J.M., Katić, V.A. (2011). The hybrid method for on-line harmonic analysis. *Advances in Electrical and Computer Engineering*, 11 (3), 29-34.
- [19] Chapman, D. (2001). *Harmonics: Causes and effects*. Power Quality Application Guide 3.1., Copper Development Association.
- [20] Antić, B.M., Mitrović, Z.L., Vujičić, V.V. (2012). A method for harmonic measurement of real power grid signals with frequency drift using instruments with internally generated reference frequency. *Measurement Science Review*, 12 (6), 277-285.
- [21] Shmilovitz, D., Duan, J., Czarkowski, D., Zabar, Z., Lee, S. (2007). Characteristics of modern nonlinear loads and their influence on systems with distributed generation. *International Journal Energy Technology and Policy*, 5 (2), 219-240.
- [22] Kozirowska, A., Bartman, J. (2012). A-model as a way of squirrel cage induction motor modelling used in pumps drive systems. *International Journal of Numerical Modelling*, 25, 103-114.
- [23] Mindykowski, J. (2016). Case study based overview of some contemporary challenges to power quality in ship systems. *Inventions*, 1 (2), 12.
- [24] Tarasiuk, T., Mindykowski, J. (2015). Problem of power quality in the wake of ship technology development. *Ocean Engineering*, 107, 108-117.
- [25] Kus, V., Josefova, T. (2017). Study of the input current harmonic distortion of voltage-source active. *Revue Roumaine des Sciences Techniques - Serie Électrotechnique et Énergétique*, 62 (2), 185-191.
- [26] Bartman, J. (2018). Evaluating the level of waveform distortion. In *Analysis and Simulation of Electrical and Computer Systems*. Springer, 305-318.

Received September 30, 2017.

Accepted March 20, 2018.

A Novel Marker Based Method to Teeth Alignment in MRI

Jean-Marc Luukinen^{1,2}, Daniel Aalto^{3,4}, Jarmo Malinen⁵, Naoko Niikuni^{1,6}, Jani Saunavaara⁷, Päivi Jääsaari^{1,2}, Antti Ojalampi⁵, Riitta Parkkola⁷, Tero Soukka^{1,2}, and Risto-Pekka Happonen^{1,2}

¹Department of Oral and Maxillofacial Surgery, University of Turku, Lemminkäisenkatu 2, 20520, Turku, Finland

²Department of Oral and Maxillofacial Diseases, Turku University Hospital, Lemminkäisenkatu 2, 20520, Turku, Finland

³Institute for Reconstructive Sciences in Medicine, Misericordia Hospital, 16940 87 Ave NW, Edmonton, AB, Canada

⁴Department of Communication Sciences and Disorders, University of Alberta, 8205 114 St NW, Edmonton, Canada

⁵Department of Mathematics and System Analysis, Aalto University, Otakaari 1 F, 00076, Espoo, Finland

⁶Department of Pediatric Dentistry, Nihon University, School of Dentistry, 4-8-24 Kudan-Minami, Chiyoda-ku, Tokyo, Japan

⁷Department of Medical Physics, Turku University Hospital, Kiinamyllynkatu 4-8, 20521, Turku, Finland

Corresponding author Jean-Marc Luukinen: jean-marc.luukinen@utu.fi

Magnetic resonance imaging (MRI) can precisely capture the anatomy of the vocal tract. However, the crowns of teeth are not visible in standard MRI scans. In this study, a marker-based teeth alignment method is presented and evaluated. Ten patients undergoing orthognathic surgery were enrolled. Supraglottal airways were imaged preoperatively using structural MRI. MRI visible markers were developed, and they were attached to maxillary teeth and corresponding locations on the dental casts. Repeated measurements of intermarker distances in MRI and in a replica model was compared using linear regression analysis. Dental cast MRI and corresponding caliper measurements did not differ significantly. In contrast, the marker locations *in vivo* differed somewhat from the dental cast measurements likely due to marker placement inaccuracies. The markers were clearly visible in MRI and allowed for dental models to be aligned to head and neck MRI scans.

Keywords: Dental imaging, Magnetic resonance imaging, MRI markers, teeth superposition, vocal tract imaging.

1. INTRODUCTION

Computed tomography (CT) is the clinical standard for creating 3D digital models of jaws. [1], [2] However, X-ray based methods expose the patients to relatively high radiation doses, which restricts their use for studying speech production. [3]-[6] Magnetic resonance imaging (MRI) provides an attractive alternative to CT since it can provide both static and dynamic imaging without the associated high ionizing radiation dose of the latter. [7]-[9] While the soft tissues are well captured in standard MRI, the high mineral content teeth crowns are typically not visible. Complete MRI based models of oral anatomy benefit the study of not only speech but also the study of other functions like chewing. In this publication, a marker-based teeth alignment method is presented and evaluated.

Methods to visualize teeth and their relation to the skull in MRI can be roughly classified in two groups. First, a digital model of dentition can be aligned to the MRI by completely or partly covering the dentition with a contrast medium to provide data for alignment. [10], [12]-[18] In these methods, a digital dental model based on optical or conventional impressions is superimposed to the MR image. Second, the dentition can be directly measured by MRI. [11], [19], [20]

The methods that have been used earlier will be presented briefly in the following paragraph.

Pure water [15] and blueberry juice [12], [16], [20] have been used as a contrast medium to cover the dentition completely. Clinical applicability is limited by an elevated aspiration risk which can be minimized by using paired plate containers [10], thermoplastic elastomer mouthpiece [13], retainer filled with ferric ammonium citrate jelly [14], or molded silicone mouthpiece coated with petroleum jelly [17]. However, hypersensitivity to a contrast medium may be a restricting factor. [21] Even a body part like the tongue can act as a contrast medium. [18] Nevertheless, tight lingual frenulum, reduced tongue mobility or small tongue size, e.g., due to glossectomy, can restrict the applicability of the method. Extraorally placed MRI visible markers have been proposed to solve the alignment problem. However, when the markers are attached to the facial skin, they are sensitive to the movement of the mimetic muscles. [17] Finally, customized MRI sequences have been proposed to simultaneously image hard and soft tissues, but those specialized sequences are not available on standard clinical scanners. [11], [19], [20], [22]

2. SUBJECTS & METHODS

Patients

Ten patients (6 men and 4 women) undergoing orthognathic surgery treatment were recruited. According to the clinical standards of the hospital, the surgical operations were planned based on cephalograms, and CT scans were not clinically justified. The youngest patient was 19 and the oldest 47 years old (Table 1.). Each patient signed an informed consent form. The procedure was approved by the Ethical Board of the Hospital District of Southwest Finland.

Table 1. Descriptive statistics of the patients participating in the study. Mean distance measures (\pm standard deviation) based on structural MRI: I-PNS (incisor–posterior nasal spine), M–S (molar–sella), and W (width dd 16–26).

	Men	Women	All
Participants	6	4	10
Age (years)	34 \pm 9	27 \pm 10	31 \pm 9
I-PNS (mm)	61.0 \pm 6.9	54.3 \pm 4.8	58.8 \pm 6.9
M-S (mm)	82.4 \pm 6.7	75.3 \pm 4.5	79.3 \pm 6.4
W (mm)	54.9 \pm 3.2	50.5 \pm 2.7	52.9 \pm 3.7

Dental casts

Dental casts and a bite index were taken for each patient. [23] Central occlusion was recorded using a bite index (made of beeswax). The bite index was also used in MRI to ensure central occlusion.

Markers

Custom-made MRI-visible markers (Fig.1.a) were attached to the teeth on the buccal/labial side of first maxillary incisors (dd 11 and 21) and molars (dd 16 and 26). The markers were also attached to the corresponding places on the dental casts (Fig.1.b). An orthodontic instrument (a Boone bracket positioning gauge) was used for vertical and caliper for horizontal placement. The exact place varied between the patients to make sure that the markers did not disturb the occlusion. An adhesive (Scotchbond TM Universal) was chosen to attach the markers rigidly to the dental surface with minimal risk of damage to the enamel surface during removal. Markers were attached to dental casts with a two-component adhesive (Araldite Rapid, Huntsman).

The MRI markers that were used had a flattened half spherical shape of diameter 5.0 ± 0.3 mm and thickness of 3.0 ± 0.3 mm. The markers had a flat facet to facilitate attachment to a dental surface using UV hardening dental adhesive.

The MRI signal from the marker is due to vegetable oil (food quality canola oil) whose most abundant fatty acid components are in the fluid phase at room temperature. The oil is bound to a matrix, produced from a circular aspen wood (*Populus tremula L.*) disk of diameter 3.8 ± 0.1 mm and thickness 2.0 ± 0.0 mm.

To produce the disks, furniture quality aspen blocks were first slowly air dried in a slightly elevated room temperature as is usual in all woodworking. When the material was deemed dry enough for cutting, wooden circular disks were produced in batches of several hundreds of items. Another heat treatment is required to drive out the remaining moisture,

and it was carried out by heating the disks using an infrared lamp for about 15 minutes. Since the temperature measurement of such small objects is difficult, the desiccation process was only visually observed so that the wood material would not get carbonized, thereby destroying the capillary structure. The weight of the disks was measured several times during the process, and the disks were deemed ready when no decrease in weight could be observed by additional infrared irradiation. It was observed that the weight of a successfully desiccated disk would soon rise markedly if it was left in the analytical balance unprotected against the humidity of air. After having removed practically all water from the wood material, vegetable oil is introduced without delay into its capillary structure by immersion. Immersion time of several hours was used. Finally, between 51-55 % of the marker matrix weight (with reachable maximum at 57 % of weight) consists of MRI visible oil.

The coating of the markers is obtained by dipping the markers in Bisphenol A -based epoxy resin. Before applying the coating, the marker matrices were rounded in a sanding drum to remove sharp corners where the coating would peel. The viscosity and surface tension of the epoxy resin were adjusted by adding water-free ethanol. It was observed that even a small amount of water in the mixture would make the resin grainy and unusable. In our application, the thickness of the coating is between 0.1–1.0 mm depending on the surface of the marker in question. The non-uniform thickness is due to the surface tension of the unhardened coating and the fact that the marker matrix was lying on a flat surface during hardening. The thin part of the coating is on the flat surface of the marker; it is positioned against the tooth surface where the thickness of the coating plays a significant role.

Because of the layered structure, the markers have good MRI contrast to air and osseous structures (due to their vegetable oil content) as well as to the water or fat containing tissues (due to their epoxy coating) (Fig.1.c).

The MRI relaxation time parameters of vegetable oil, or the prepared MRI visible marker matrices, were not measured. It was, however, observed in MRI phantom experiments that the coated markers produce a signal level comparable with oil containing gelatin capsules that are often used to mark positions on patients' skin during MRI experiments.

Patient and dental cast imaging

All MRI scans were performed using Siemens Magnetom Avanto 1.5T scanner (Siemens Healthineers, Erlangen, Germany). A 12-element Head Matrix Coil and a 4-element Neck Matrix Coil were used to cover the anatomy of interest. The coil configuration allows the use of Generalized Auto-calibrating Partially Parallel Acquisition (GRAPPA) technique to accelerate acquisition. 3D VIBE (Volumetric Interpolated Breath-hold Examination) MRI sequence was used to acquire the high-quality images of the patients' maxilla and mandible. Following parameters were used to obtain images with 0.9 mm isotropic voxels in 215 seconds: Time of repetition (TR) was 4.26 ms, echo time (TE) 1.57 ms, flip angle (FA) 6°, parallel acquisition technique (PAT) acceleration factor, number of slices 120, and number of averages 3.

For comparison, a data set with 1.8 mm isotropic voxels was acquired during sustained vowel production. Using VIBE sequence and the following parameters the data acquisition took less than 9 seconds: TR 3.75 ms, TE 1.19 ms, FA 6°, PAT 2, number of slices 44, and number of averages 2.

In addition, 3D MRI technique was used to scan the dental casts with the markers. Since dental casts are not visible in MRI, they were embedded in blueberry juice that served as a contrast medium for MRI (Fig.1.d). The following parameters allowed imaging with 0.9 mm isotropic voxels in less than 3 min: TR 4.26 ms, TE 1.57 ms, FA 6°, number of slices 120, and number of averages 4.

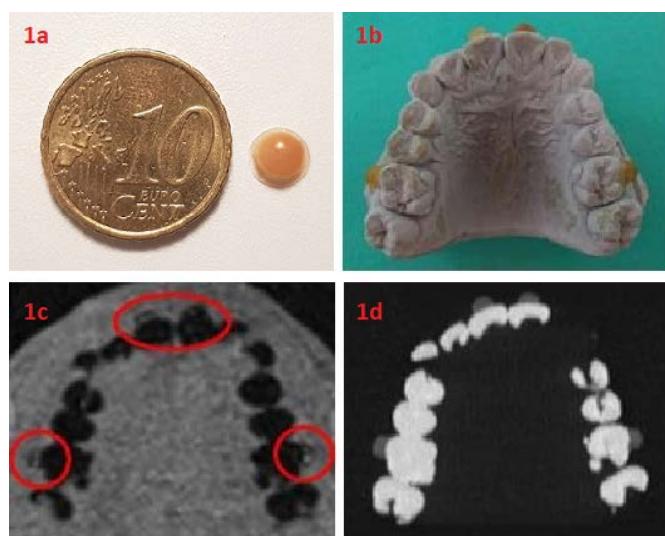


Fig.1. a) A marker with a ten cent (euro) coin with diameter 19 mm, b) An inferior view of the dental cast showing the markers on dental cast, c) The corresponding axial slice of the patient showing markers, d) Axial slice of an MR image showing dental cast immersed in blueberry juice.

Cephalometry (Cranex® D, Soredex, Tuusula, Finland) radiographs were used as a benchmark for the teeth alignment method evaluation. The imaging time in cephalogram was 14.6 s. During the imaging, the head was stabilized to avoid movement artifact.

Landmarks

Three cranial landmarks visible in both imaging modalities (X-ray and MR) were selected. These were anterior nasal spine (ANS), posterior nasal spine (PNS), and the midpoint of sella (S). Dental markers in the MRI and the corresponding points on the teeth in lateral X-ray served as additional landmarks.

Landmark and marker registration

Intermarker distances were obtained from the patient MRI, dental cast MRI, and from dental casts using a caliper. The anatomical landmarks were measured from the cephalogram and the patient MRI. The measurements between different modalities were compared.

The landmarks were located in the MR image by adjusting the orientation and position of the mutually orthogonal planes in the orthogonal multi-planar reconstruction (MPR) and recording the coordinate values using OsiriX (Advanced Open-Source PACS Workstation DICOM Viewer) (Fig.2.).

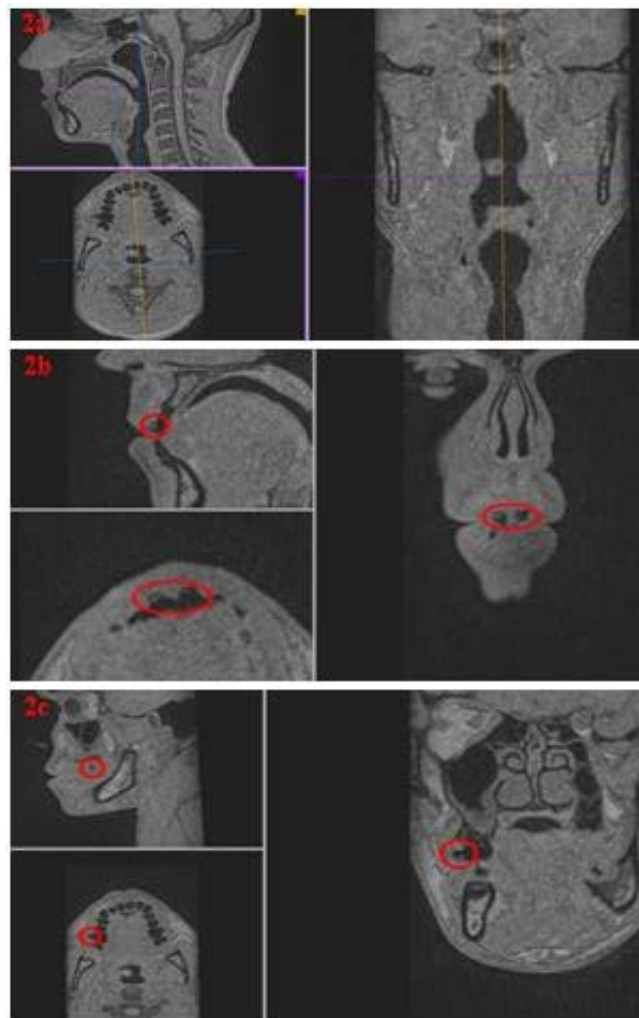


Fig.2. a) The MPR technique was used to locate anatomical landmarks in the midsagittal plane, b) Markers on the maxillary incisors (dd 11, 21), c) The marker on the first maxillary molar (d 16).

The midsagittal plane was aligned based on the foramen magnum or four uppermost vertebrae C1-C4, the eyes, and the palatal arch. The dental markers were registered at planes tangent to the flat surface of the markers. Within the dental casts, the distances between the dental markers as well as the vertical position between the markers and the inferior edge of the crown were measured by a digital vernier caliper (Mitsutoyo, nominal accuracy 0.1 mm). Measured distances between the teeth were dd 11–21, dd 11–16, dd 11–26, dd 21–26, dd 21–16, and dd 16–26 (Fig.3.). Three independent measurements were taken for each measure, and the median value was used in geometrical transformations and statistical analyses. For estimating measurement errors, measurements for one patient were repeated 20 times.

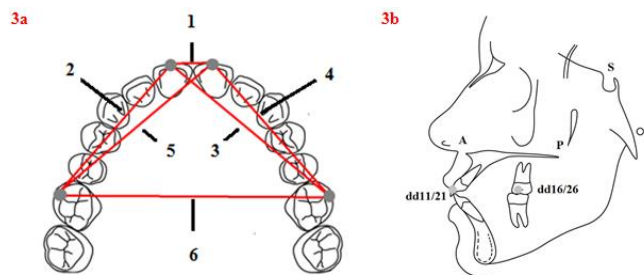


Fig.3. a) Schematic drawing of the distances between the dental markers: 1 = dd 11-21, 2 = dd 11-16, 3 = dd 11-26, 4 = dd 21-26, 5 = dd 21-16, and 6 = dd 16-26, b) Illustration of the anatomical landmarks and the markers: A = Anterior nasal spine, P = Posterior nasal spine, and S = Sella.

During the X-ray imaging, the markers were not held in the mouth. By observing marker positions on the dental casts, the corresponding points were registered in the cephalogram. To compare the cephalogram and the MRI data, the MRI data was geometrically transformed to match the corresponding cephalometric distances (Fig.4.). The transformation was very coarse: parasagittal points (incisors, molars) were orthogonally projected to the midsagittal plane (defined as the plane containing ANS, PNS, and sella).

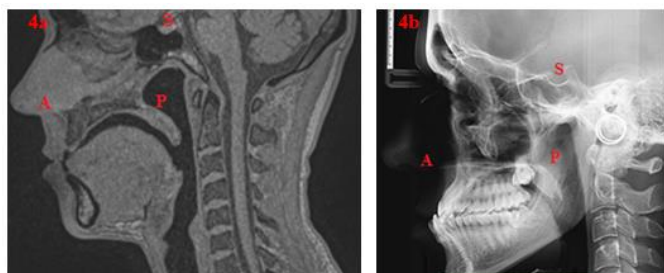


Fig.4. a) A midsagittal slice of an MRI, b) Cephalogram. In both pictures, from the same patient the anatomical landmarks (A = Anterior nasal spine, P = Posterior nasal spine, and S = Sella) are clearly observable.

Dental cast alignment

The recorded coordinate values of the markers on the dental cast in MRI and the corresponding coordinate values on the dentitions in MRI were used to create an optimal estimate of the rigid body coordinate transformation based on the singular value decomposition (SVD). [24] The alignment results are presented visually in Fig.5. and summarized in Table 2.

Patients M04 and M06 show subvoxel accuracy, Table 2. Some markers became loose (d26 in M07 and d16 in W05) or were lost completely (d16 in M07). At least three markers are necessary for alignment and due to missing markers could not be done for M03 and W04. *For M02 the markers were attached to d13 and d23 instead of d11 and d21. **The marker d16 became loose (and consequently misplaced) and was not included in the computation of the optimal rigid transformation.

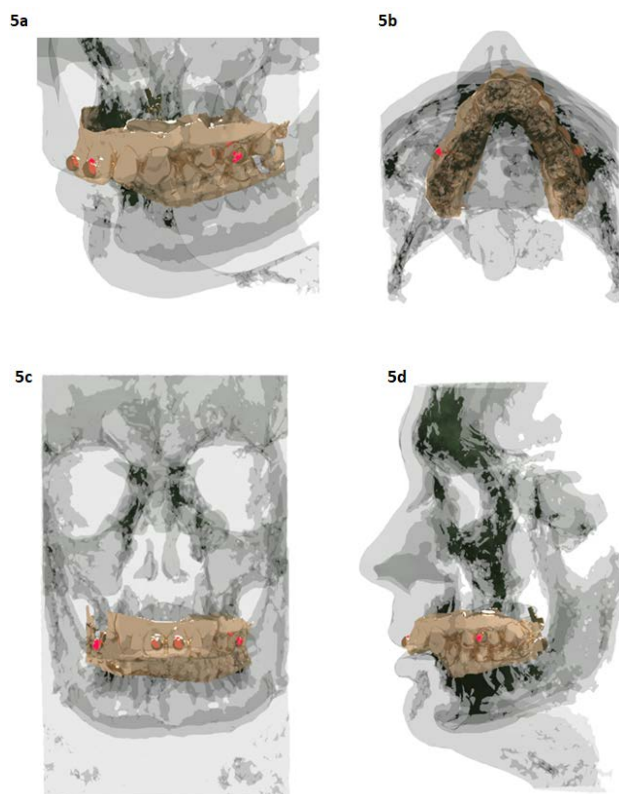


Fig.5. Translucent 3D models of the head and neck anatomy with dark color for osseous tissue. The dental casts (light brown) are superposed to the images based on the markers (red). The oblique view shows an overbite a), the inferior view of the maxilla shows the lateral asymmetry b), frontal view shows lateral asymmetry in mandible c), and the lateral view d) shows the position of the marker on the molar.

Table 2. Alignment error between optimally rotated and translated dental cast model markers and the intraoral markers.

Patient	Alignment error (mm)			
	d11	d16	d21	d26
M02*	1.61	1.62	0.88	1.28
M03	N/A	N/A	N/A	N/A
M04	0.40	0.28	0.60	0.69
M06	0.43	0.64	0.62	0.75
M07	3.53	N/A	1.91	3.68
M08	2.41	1.91	2.57	0.89
W04	N/A	N/A	N/A	N/A
W05	0.12	7.52**	0.24	0.12
W06	0.26	0.77	1.11	0.65
W07	1.02	0.87	0.95	0.82

Statistical analysis

The data was analyzed for consistency within every modality and for discrepancy across modalities based on distance measures. *Caliper precision* was defined as the residual standard error of the linear regression model with intermarker distance as the dependent variable and the marker pair as the independent variable. *MRI registration precision* for dental markers (including both dental cast and patient MRI) and cranial landmarks was defined similarly. *Cephalometric registration precision* was estimated similarly.

Cranial landmarks offer an alternative to marker-based solutions. The accuracy of locating the landmarks was assessed using three cranial landmarks (ANS, PNS and sella) using repeatedly acquired MRI scans with two spatial resolutions (0.9 mm isotropic voxels, 1.8 mm isotropic voxels). [25], [26] The consistency was again defined as the standard residual error of the fitted linear regression model.

Cross-modally, caliper measurements were compared with the MRI measurements of dental casts and patient MRI. A linear regression model for the dental marker distance differences was fitted, and the standard residual error and the intercept served as a measure for precision and bias. More detailed models included the distance measures as a factor. Similarly, linear regression models were used to compare cephalometric and MRI measures between cranial landmarks. Finally, dental alignment was assessed by linear regression models where the dependent variable was the difference between MRI and cephalometric landmark to marker distance.

Visualization of results

The results were visualized in one patient. Accurate coordinate measurements were made from the dental markers in MRI from the dental cast immersed in blueberry juice and the patient. Based on these coordinates, geometric models were created using the marching cubes algorithm (Fig.5.). [27], [28].

3. RESULTS

Variability within a modality

Caliper precision was 0.15 mm. MRI registration precision for dental markers attached to dental cast was 0.32 mm and 0.39 mm when attached to the dentition. The MRI registration precision for the cranial landmarks was 0.57 mm and the cephalometric landmark registration precision was 0.32 mm (Fig.6.). In repeated MRI scans (1.8 mm isotropic voxels) of the same subjects, the cranial landmark registration precision was 1.2 mm.

Cross modal comparisons

Dental cast MRI did not differ significantly from the corresponding caliper measurements (intercept: 0.47 mm, residual standard error: 1.8 mm, $t = 1.8$, n.s.). The dental MRI distances were underestimated with respect to the caliper measurements (intercept: 0.77 mm, residual standard error: 1.3, $t = 4.1$, $p < 0.01$). The underestimation was mainly due to dd 21–26 distance (1.6 mm, $t = 2.8$, $p < 0.01$) and dd 11–

16 (1.5 mm, $t = 2.7$, $p = 0.01$). Differences in intermarker distances between dental cast MRI and patient dental MRI measurements were not statistically significant (intercept: 0.0 mm, residual error: 2.0 mm, $t = 0.1$, n.s.). Cranial landmark accuracy was good (intercept 0.6 mm, residual standard error: 3.0 mm, $t = 1.0$, n.s.). The distance between dental markers and cranial landmarks was in average 2.1 ± 2.9 mm larger in MRI compared to cephalogram ($t = 4.9$, $df = 47$, $p < 0.01$). The molar-PNS distance was 3.0 mm larger ($p = 0.07$) and the molar-ANS distance 3.6 mm smaller ($p = 0.01$) compared with the average 2.1 mm general overestimation trend.

Dental cast alignment

The alignment was successful in eight cases and impossible in two cases due to missing data. The difference between the optimally aligned cast and the dental markers varied around one millimeter as shown in Table 2. For M03 and W04, at least two markers were missing preventing alignment. The molar marker (d16) became loose in M07 when entering MRI and could not be reattached in situ while the other molar marker (d26) became loose and displaced within MRI. The resulting rigid transformation contained a reflection and led to erroneous alignment. In W05, the marker d16 became loose and displaced and was not included when determining the rigid transformation. Seven alignments were successful, an example is shown in Fig.5.

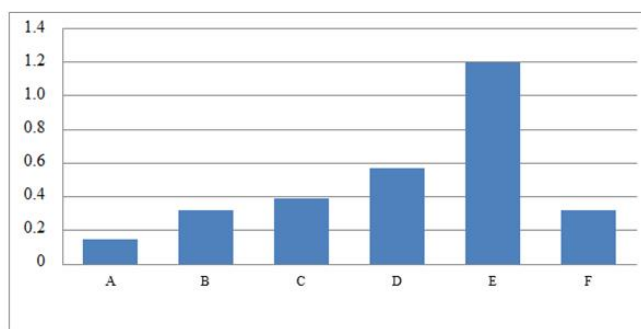


Fig.6. Standard deviations (in mm) of repeated measurements for each measuring method.

- Caliper measurement from the dental cast.
- Dental cast in MRI with 0.9 mm isotropic voxels.
- Dentition in MRI with 0.9 mm isotropic voxels.
- Cranial landmarks in MRI with 0.9 mm isotropic voxels.
- Cranial landmarks in MRI with 1.8 mm isotropic voxels.
- Cranial landmarks in cephalogram.

4. DISCUSSION

In this publication, a marker-based method to superpose teeth in MRI is presented and evaluated. Several methods to visualize teeth in MRI have been proposed but the teeth alignment methods have been evaluated only perceptually. In this study, the accuracy is determined by repeated measurements and cross modal comparisons. Based on standard deviation of repeated measurements the accuracy for dental markers in MRI, when attached to dental cast and dentition, is 0.32 mm and 0.39 mm, respectively.

Dental MRI marker distances are smaller than the corresponding caliper measurements in the dental casts. The difference is due to ipsilateral comparisons. The poor visibility and moist conditions, especially in molar area, may complicate the attaching of the marker and this way affects the results negatively. This is supported by dental cast caliper and dental cast MRI distances being comparable. On the other hand, the bottom of the marker in MRI may be detected slightly too mesially.

Cranial landmark distances in MRI are comparable to the corresponding cephalometric measurements. The distortion is minor between different imaging methods because the anatomical landmarks were in the midsagittal plane although some of the patients had lateral asymmetries so that the midsagittal plane could not be determined unambiguously.

Even in the same MR stack the detectability of anatomical landmarks is weaker than the detectability of the markers. Firstly, the determination of the midsagittal plane is more difficult than the determination of the marker attachment plane. Secondly, the anatomical shapes (ANS, PNS, and sella) are less symmetrical than the proposed markers which complicates the within plane positioning of the target points.

The measures between markers in 3D MRI and 2D cephalogram showed clear discrepancies. Cephalometric distortion occurs because of different magnification between adjacent parasagittal planes. In MRI, the distances between the anatomical landmarks and markers are systematically 2 mm bigger than in cephalogram. In a cephalogram, the incisors and molars are not situated in the midsagittal plane and thus give a dual image on the radiograph. [26] The error is due to the fact that in cephalograms the supposed locations of markers are estimated too cranially due to the double images. The cephalometric distances are simulated from the MRI by orthogonally projecting the parasagittal marker locations to the mid-sagittal plane which is not an accurate enough model of the cephalogram. However, the exact orientation of the patient with respect to the image plane and the signal source could not be reliably estimated.

The markers were coated by inert plastic for several reasons. Firstly, the oil will little by little seep out of the matrix if there is nothing to stop it. Secondly, the dental resin does not stick to an oily surface. Thirdly, even though the oil impregnated matrix has good MRI contrast against osseous tissue and air, it has poor contrast against soft tissues such as lip and tongue that may touch the tooth and marker surface.

Handling of the hemispherical markers is cumbersome and the marker adherence is not optimal. A custom applicator could make the maneuvering steadier and increase the precision. The markers are attached to the teeth firmly, but some of the markers would come loose if the patient touched them with the tongue or made big lip movements. Nevertheless, even if a marker came loose, the registration is still possible with the remaining three markers. Furthermore, since the proposed markers are attached to the buccal surface of the teeth, there is no distortion in occlusion. However, some types of malocclusion may complicate or even make the attachment of the marker to the labial/buccal surface of the teeth impossible.

Several unsuccessful ideas were tested in the marker design. Small plastic disks were chemically silver-plated in hopes of

getting identifiable MRI artefacts such as those produced by amalgam fillings. Objects containing solid hydrocarbons (e.g., paraffin wax and stearin) were tried but no signal was obtained. Liquid oil can be enclosed in small PLA/ABS plastic frames but producing sufficiently small, dimensionally accurate, and oil tight plastic parts appeared to be impossible, at least using inexpensive 3D printers. Using plastic enclosures of some other type, however, is likely to be a cost-effective solution of choice if large scale production of markers is required. Another idea is to plastic coat gelatin capsules containing oil but the authors considered that approach more uncertain and not much easier to implement than binding the oil to a capillary structure.

The dental markers could be placed and located well for every studied patient despite substantial variability in their occlusions. The accuracy achieved is sufficient to separate the hard and soft tissue. At the moment, these markers are not commercially available, but they could be industrially produced. Even if the proposed markers would not be the solution to the tooth visibility in MRI, they may be needed for the evaluation of another method. The marker data is useful to register the anatomy data which comes from different imaging modalities when complete geometric models are needed.

5. CONCLUSION

A marker-based solution to superpose teeth to MRI is presented. The markers are visible in MRI and help in aligning the dental models to head and neck anatomy. The accuracy achieved is promising and suggests that digital dental cast models can be superposed to digital models based on MRI with high precision.

ACKNOWLEDGMENT

The authors would like to thank anonymous reviewers for valuable feedback, Mr. Jarkko Malinen for significant and time-consuming marker manufacturing, and the funding from Aalto Starting Grant, Magnus Ehrnrooth Foundation, and from Hospital district of Southwest Finland, EVO project grant 13939.

REFERENCES

- [1] Rohner, D., Jaquiéry, C., Kunz, C., Bucher, P., Maas, H., Hammer, B. (2003). Maxillofacial reconstruction with prefabricated osseous free flaps: A 3-year experience with 24 patients. *Plastic and Reconstructive Surgery*, 112 (3), 748-757.
- [2] Plooij, J.M., Maal, T.J., Haers, P., Borstlap, W.A., Kuijpers-Jagtman, A.M., Bergé, S.J. (2011). Digital three-dimensional image fusion processes for planning and evaluating orthodontics and orthognathic surgery. A systematic review. *International Journal of Oral and Maxillofacial Surgery*, 40 (4), 341-352.
- [3] Jones, S. (1929). Radiography and pronunciation. *British Journal of Radiology*, 2 (15), 149-56.
- [4] Scheier, M. (1897). Die Anwendung der Röntgenstrahlen für die Physiologie der Stimme und Sprache. *Deutsche Medizinische Wochenschrift*, 23 (25), 403.

- [5] Vampola, T., Horáček, J., Laukkanen, A.M., Švec, J.G. (2015). Human vocal tract resonances and the corresponding mode shapes investigated by three-dimensional finite-element modelling based on CT measurement. *Logopedics Phoniatrics Vocology*, 40 (1), 14-23.
- [6] Sovijärvi, A. (1938). *Die gehaltenen, geflüsterten und gesungenen vokale und nasale der Finnischen sprache - physiologisch-physikalische lautanalysen*. Helsinki: Annales Academiæ Scientiarum Fennicæ; German text.
- [7] Lingala, S.G., Sutton, B.P., Miquel, M.E., Nayak, K.S. (2016). Recommendations for real-time speech MRI. *Journal of Magnetic Resonance Imaging*, 43 (1), 28-44.
- [8] Baer, T., Gore, J.C., Boyce, S., Nye, P.W. (1987). Application of MRI to the analysis of speech production. *Magnetic Resonance Imaging*, 5 (1), 1-7.
- [9] Scott, A.D., Wylezinska, M., Birch, M.J., Miquel, M.E. (2014). Speech MRI: Morphology and function. *Physica Medica: European Journal of Medical Physics*, 30 (6), 604-618.
- [10] Wakumoto, M., Masaki, S., Dang, J., Honda, K., Shimada, Y., Fujimoto, I., Nakamura, Y. (1997). Visualization of dental crown shape in an MRI-based speech production study. *International Journal of Oral and Maxillofacial Surgery*, 26, 189-190.
- [11] Hövener, J.B., Zwick, S., Leupold, J., Eisenbeiß, A.K., Scheifele, C., Schellenberger, F., Hennig, J., Elverfeldt, D., Ludwig, U. (2012). Dental MRI: Imaging of soft and solid components without ionizing radiation. *Journal of Magnetic Resonance Imaging*, 36 (4), 841-846.
- [12] Hiraiishi, K., Narabayashi, I., Fujita, O., Yamamoto, K., Sagami, A., Hisada, Y., Saika, Y., Adachi, I., Hasegawa, H. (1995). Blueberry juice: Preliminary evaluation as an oral contrast agent in gastrointestinal MR imaging. *Radiology*, 194 (1), 119-123.
- [13] Kitamura, T., Nishimoto, H., Fujimoto, I., Shimada, Y. (2011). Dental imaging using a magnetic resonance visible mouthpiece for measurement of vocal tract shape and dimensions. *Acoustical Science and Technology*, 32 (5), 224-227.
- [14] Ng, I.W., Ono, T., Inoue-Arai, M.S., Honda, E., Kurabayashi, T., Moriyama, K. (2011). Application of MRI movie for observation of articulatory movement during a fricative/s/and a plosive/t/ Tooth visualization in MRI. *The Angle Orthodontist*, 81 (2), 237-244.
- [15] Olt, S., Jakob, P.M. (2004). Contrast-enhanced dental MRI for visualization of the teeth and jaw. *Magnetic Resonance in Medicine*, 52 (1), 174-176.
- [16] Takemoto, H., Kitamura, T., Nishimoto, H., Honda, K. (2004). A method of tooth superimposition on MRI data for accurate measurement of vocal tract shape and dimensions. *Acoustical Science and Technology*, 25 (6), 468-474.
- [17] Ventura, S.R., Freitas, D.R., Ramos, I.M., Tavares, J.M.R. (2014). Three-dimensional visualization of teeth by magnetic resonance imaging during speech. In *Biodental Engineering II*. Taylor & Francis Group, 13-17.
- [18] Ventura, S.R., Freitas, D.R., Tavares, J.M.R. (2009). Application of MRI and biomedical engineering in speech production study. *Computer Methods in Biomechanics and Biomedical Engineering*, 12 (6), 671-681.
- [19] Idiyatullin, D., Corum, C., Moeller, S., Prasad, H.S., Garwood, M., Nixdorf, D.R. (2011). Dental magnetic resonance imaging: Making the invisible visible. *Journal of Endodontics*, 37 (6), 745-752.
- [20] Traser, L., Flügge, T.V., Burdumy, M., Kamberger, R., Richter, B., Hassepas, F., Korvink, J.G., Echternach, M. (2015). A comparison of different methods to generate tooth surface models without applying ionizing radiation for digital 3-dimensional image fusion with magnetic resonance imaging-based data of the head and neck region. *Journal of Computer Assisted Tomography*, 39 (6), 882-889.
- [21] Sicherer, S.H., Sampson, H.A. (2006). Food allergy. *Journal of Allergy and Clinical Immunology*, 117 (2), S470-S475.
- [22] Weiger, M., Pruessmann, K.P., Bracher, A.K., Köhler, S., Lehmann, V., Wolfram, U., Hennel, F., Rasche, V. (2012). High-resolution ZTE imaging of human teeth. *NMR in Biomedicine*, 25 (10), 1144-1151.
- [23] Ender, A., Mehl, A. (2013). Accuracy of complete-arch dental impressions: A new method of measuring trueness and precision. *Journal of Prosthetic Dentistry*, 109 (2), 121-128.
- [24] Eggert, D.W., Lorusso, A., Fisher, R.B. (1997). Estimating 3-D rigid body transformations: A comparison of four major algorithms. *Machine Vision and Applications*, 9 (5-6), 272-290.
- [25] Aalto, D., Aaltonen, O., Happonen, R.P., Jääsaari, P., Kivelä, A., Kuortti, J., Luukinen, J.M., Malinen, J., Murtola, T., Parkkola, R., Saunavaara, J., Soukka, T., Vainio, M. (2014). Large scale data acquisition of simultaneous MRI and speech. *Applied Acoustics*, 83, 64-75.
- [26] Ojalampi, A., Malinen, J. (2017). Automated segmentation of upper airways from MRI - vocal tract geometry extraction. In *Proceedings of the 10th International Joint Conference on Biomedical Engineering Systems and Technologies – Volume 2: Bioimaging*. Setúbal, Portugal: SciTePress, 77-84.
- [27] Athanasiou, A.E., Van der Meij, A.J.W. (1995). Posteroanterior (frontal) cephalometry. In *Orthodontic Cephalometry*. Mosby-Wolfe, 141-161.
- [28] Lorensen, W.E., Cline, H.E. (1987). Marching cubes: A high resolution 3D surface construction algorithm. In *SIGGRAPH '87: Proceedings of the 14th Annual Conference on Computer Graphics and Interactive Techniques*. ACM, 163-169.

Received November 20, 2017.

Accepted March 21, 2018.